UNIVERSIDAD COMPLUTENSE DE MADRID
FACULTAD DE CIENCIAS FÍSICAS
Departamento de Física de Materiales

TESIS DOCTORAL

Fenómenos interfacionales asociados a vacantes de oxígeno en heteroestructuras de óxidos

Oxygen vacancy driven interfacial phenomena in oxide heterostructures

MEMORIA PARA OPTAR AL GRADO DE DOCTOR

PRESENTADA POR

Mariona Cabero Piris

Director

Jacobo Santamaría Sánchez-Barriga

Madrid, 2018

UNIVERSIDAD COMPLUTENSE DE MADRID

Facultad de Ciencias Físicas

GRUPO DE FÍSICA DE MATERIALES COMPLEJOS

Departamento de Física de Materiales

Fenómenos interfaciales asociados a vacantes de oxígeno en heteroestructuras de óxidos

Oxygen vacancy driven interfacial phenomena in oxide heterostructures

Trabajo presentado como requisito para optar al grado de Doctor en Física

Autor:

Mariona Cabero Piris

Directores:

Jacobo Santamaría Sánchez-Barriga

María Varela del Arco

Madrid, Febrero 2017

Content

Resumen en español

Chapter 1: Introduction

Chapter 2: Experimental techniques

Chapter 3: Effects of oxygen vacancies on the magnetic anisotropy of LSMO/LCO/LSMO heterostructures

Chapter 4: Oxygen vacancy doping in multiferroic tunnel junctions

Chapter 5: Interfacially enhanced conductivity in YSZ thin films

Chapter 6: Summary

Anex

Resumen en español

1. Introducción

Los óxidos complejos son una familia de compuestos de óxidos de metales de transición con un amplio espectro de propiedades para su aplicación en electrónica de óxidos, como son: ferromagnetismo, antiferromagnetismo, superconductividad, ferroelectricidad, etc. En particular, son buenos candidatos para dispositivos reales, ya que las interfases de estos materiales generan un escenario prometedor gracias a la interacción entre sus efectos eléctricos y magnéticos [1]. Las distintas interacciones entre los distintos grados de libertad como son la carga, el espín, la red cristalina y los orbitales dan lugar a una amplia variedad de fases electrónicas. Por tanto, la combinación de estas propiedades en heteroestructuras de alta calidad cristalina pueden dar lugar a diferentes estados electrónicos [2]. El comportamiento de los electrones en estos sistemas está sujeto a las interacciones culombianas con primeros vecinos y, por tanto, los materiales no se pueden describir con el modelo clásico de bandas. Un ejemplo de este tipo de comportamiento es el que se da en los aislantes de Mott, en los que la repulsión culombiana es suficientemente intensa para inducir un estado aislante a pesar de que la teoría de bandas prediga exactamente lo opuesto para una ocupación parcial de las bandas [3].

Es bien sabido que este tipo de materiales crecen con deficiencias de oxígeno, las cuales pueden dar lugar a cambios en sus las propiedades físicas, ya sea por el efecto electrónico de dopado o por los cambios estructurales que puedan generar en la red cristalina. Por ejemplo, el $LaMnO_3$ estequiometrico es un aislante antiferromagnético que presenta ferromagnetismo cuando la red es deficiente en oxígeno [4]. Otros estudios demuestran que la familia de cobaltitas $(La,Sr)CoO_3$ en película delgada sobre sustratos de $NdGaO_3$ y $(La,Sr)(Al,Ta)O_3$ tiene diferentes imanaciones de saturación [5]. Es estos experimentos se ha demostrado que, la diferencia en el contenido de vacantes de oxígeno en las películas delgadas para diferentes sustratos pueden ser responsables de la mejora observada en las propiedades magnéticas. Un caso particularmente importante es el del $LaCoO_3$, en el que se ha demostrado que cuando se crece en película delgada hay que tener en cuenta la combinación de la tensión epitaxial y las vacantes de oxígeno, pues ambos fenómenos son interdependientes. En este caso, la estabilización de espín del Co^{2+} y Co^{3+} está directamente relacionado con una superestructura ordenada de vacantes en la red que da lugar a la interacción de canje ferromagnética.

Otro tipo de sistemas en óxidos de metales de transición a tener en cuenta son aquellos que integran óxidos ferroeléctricos en sus estructuras. En estos dispositivos, las vacantes de oxígeno permiten que se den varios estados memristivos debido a la alta movilidad de éstas comparada con los otros cationes [6,7]. También se dan casos en los que las vacantes pueden incluso estabilizan fronteras de dominios ferroeléctricos, como es el ejemplo en uniones túnel multiferroicas, basadas en barreras ferroeléctricas de $BaTiO_3$, en las que se han observado cómo la estabilización de paredes de dominio head-to-head o tail-to-tail dan lugar a conductividad túnel resonante [8].

Por último, no podemos olvidar los conductores iónicos, específicamente el ZrO_2:Y_2O_3. En este sistema se ha encontrado conductividad iónica colosal, producto de una tensión epitaxial del 14% en películas ultradelgadas crecidas entre capas de $SrTiO_3$. Barriocanal et al. proponen que las reconstrucciones atómicas en interfaces tan diferentes dan lugar a un gran número de portadores así como un plano de alta movilidad, reportando un plano lateral de alta conductividad con una mejora en 8 órdenes de magnitud cerca de temperatura ambiente [9,10].

La formación de vacantes de oxígeno se puede controlar durante el proceso de crecimiento, ya sea realizando recocidos en vacío a alta temperatura. Oras rutas son la tensión epitaxial, ya que al introducir sustratos con ciertos grados de tensión pueden forzar a la película delgada a crecer con un contenido de vacantes para minimizar su energía [11]. Por esto, basándonos en este grado de libertad, la motivación de esta tesis ha sido la fabricación y caracterización de heteroestructuras y películas delgadas en las que el oxígeno juega un papel esencial. Este trabajo está focalizado en los cambios locales que provocan las vacantes y que lugar a cambios o mejoras en las propiedades macroscópicas, de transporte y magnetismo, para diferentes sistemas en los que hay una falta de oxígeno.

2. Resultados

Dentro del marco introducido, los resultados de esta tesis se organizan en los siguientes experimentos:

- En primer lugar, se ha estudiado la anisotropía magnética de películas delgadas de $La_{0.7}Sr_{0.3}MnO_3$ crecidas sobre $LaCoO_3$. En primer lugar, se ha realizado un estudio por STEM-EELS de películas delgadas de $La_{1-x}Sr_xCoO_3$ sobre sustratos con diferentes grados de tensión epitaxial (compresivo y expansivo), con objeto de utilizar los resultados para un análisis de los estados de oxidación en un análisis posterior. El experimento consiste en la fabricación de uniones túnel multiferroicas con electrodos de $La_{0.7}Sr_{0.3}MnO_3$ y barreras aislantes de $LaCoO_3$. La tensión epitaxial inducida por el sustrato de $SrTiO_3$ en la barrera de $LaCoO_3$ da lugar a la aparición de planos atómicos La-La con diferentes elongaciones debido a la presencia de vacantes de oxígeno. Estos efectos tienen implicaciones importantes en la anisotropía magnética del electrodo de $La_{0.7}Sr_{0.3}MnO_3$, que se encuentra crecido sobre $LaCoO_3$. De este modo, se ha realizado un estudio en bicapas con secuencia de crecimiento intercambiada ($La_{0.7}Sr_{0.3}MnO_3$/ $LaCoO_3$ y $LaCoO_3$/ $La_{0.7}Sr_{0.3}MnO_3$). Se han encontrado evidencias de cambios en la anisotropía magnética en las películas de $La_{0.7}Sr_{0.3}MnO_3$ crecidas sobre $LaCoO_3$ debido al desorden estructural inducido por los planos de vacantes desordenados en el $LaCoO_3$.

- El siguiente experimento ha estado dedicado a la fabricación y caracterización de uniones túnel multiferroicas basadas en $La_{0.7}Sr_{0.3}MnO_3$/ $BaTiO_3$/ $La_{0.7}Sr_{0.3}MnO_3$, en las cuales se ha introducido una asimetría en el sistema, consistente en una película ultradelgada de un cuprato fuertemente desoxigenado entre el electrodo superior y la barrera de $BaTiO_3$. La introducción de una gran densidad de vacantes en el sistema ha dado lugar a una mejora en la electrorresistencia túnel en un 10^4%. Además, se ha observado que el estado de polarización y la posición en la red de las vacantes de oxígeno se puede controlar el tamaño de la zona de carga espacial. Con esto se ha buscado mejorar la electrorresistencia túnel y la magnetorresistencia túnel de las uniones.

- Por último, el sistema que se presenta en este capítulo es un conductor iónico de oxígeno bien conocido, el Y_2O_3:ZrO_2. Este trabajo está basado en el crecimiento de interfaces fluoirta/perovskita con planos de terminación con distintas simetrías y un grado de tensión epitaxial muy pequeño. El sustrato elegido es el $YAlO_3$, por tener parámetros de red muy similares y ser un material muy aislante. El Y_2O_3:ZrO_2 se ha crecido en películas delgadas de distintos grosores sobre sustratos de $YAlO_3$, dando lugar a un aumento de la conductividad que viene determinado por los primeros 4 nm de Y_2O_3:ZrO_2. Se ha realizado un estudio de los efectos interfaciales utilizando espectroscopía de impedancias y STEM-EELS.

3. Conclusiones

A lo largo de esta tesis hemos mostrado como los efectos interfaciales en presencia de vacantes de oxígeno pueden dar lugar a cambios fundamentales en las propiedades eléctricas y magnéticas. Particularmente en este trabajo, se han crecido y caracterizado varios sistemas basados en óxidos fuertemente correlacionados, los cuales muestran una gran sensibilidad a los cambios locales. Por este motivo se han crecido diferentes heteroesctructuras y hemos fabricado un dispositivo con objeto de estudiar los fenómenos derivados de la presencia de vacantes de oxígeno, utilizándolas como grado de libertad en dispositivos emergentes. Gracias a las técnicas de crecimiento por sputtering y la microscopía electrónica con corrector de aberraciones hemos podido fabricar y estudiar de forma local las fluctuaciones en la composición química o en la estructura, estableciendo conexiones entre mecanismos atómicos y las propiedades eléctricas y magnéticas de los sistemas.

4. Bibliografía

[1]J. Mannhart and D. G. Schlom, "Oxide Interfaces: An Opportunity for Electronics" *Science* **327**, 1607–1611 (2010).

[2]Y. Tokura, "Correlated-Electron Physics in Transition-Metal Oxides" *Phys. Today*, **56**, 50 (2003).

[3]N. F. Mott, "Metal-insulator transition", *Rev. Mod. Phys.* **40**, 677–683, (1968).

[4]R. Zhao, K. Jin, Z. Xu, H. Guo, L. Wang, C. Ge, H. Lu, and G. Yang, "The oxygen vacancy effect on the magnetic property of the $LaMnO_{3-\delta}$ thin films", *Appl. Phys. Lett.* **102**, 122402 (2013).

[5]Y.-M. Kim, J. He, M. D. Biegalski, H. Ambaye, V. Lauter, H. M. Christen, S. T. Pantelides, S. J. Pennycook, S. V. Kalinin, and A. Y. Borisevich, "Probing oxygen vacancy concentration and homogeneity in solid-oxide fuel-cell cathode materials on the subunit-cell level" *Nat. Mater.* **11**, 888–894 (2012).

[6]R. Waser and M. Aono, "Nanoionics-based resistive switching memories", *Nat. Mater.* **6**, 833–40 (2007).

[7]R. Waser, R. Dittmann, C. Staikov, and K. Szot, "Redox-based resistive switching memories nanoionic mechanisms, prospects, and challenges", *Adv. Mater.* **21**, 2632–2663 (2009).

[8]G. Sánchez-Santolino, J. Tornos, D. Hernández-Martín, J. I. Beltrán, C. Munuera, M. Cabero, A. Pérez-Muñoz, F. Monpean, M. Garcia-Hernandez, Z. Sefrioui, C. León, S. J. Pennycook, M. C. Muñoz, M. Varela, and J. Santamaría, "Realization of a ferroelectric-domain-wall tunnel junction", (*Nature Nanotechnology*, accepted 2017*)*

[9]J. Garcia-Barriocanal, a Rivera-Calzada, M. Varela, Z. Sefrioui, E. Iborra, C. Leon, S. J. Pennycook, and J. Santamaria, "Colossal ionic conductivity at interfaces of epitaxial ZrO2:Y2O3/SrTiO3 heterostructures" *Science* **321**, 676–80 (2008).

[10]A. Rivera-Calzada, M. R. Diaz-Guillen, O. J. Dura, G. Sanchez-Santolino, T. J. Pennycook, R. Schmidt, F. Y. Bruno, J. Garcia-Barriocanal, Z. Sefrioui, N. M. Nemes, M. Garcia-Hernandez, M. Varela, C. Leon, S. T. Pantelides, S. J. Pennycook, and J. Santamaria, "Tailoring interface structure in highly strained YSZ/STO heterostructures," *Adv. Mater.* **23**, 5268–5274 (2011).

[11]V. V Mehta, N. Biskup, C. Jenkins, E. Arenholz, M. Varela, and Y. Suzuki, "Long-range ferromagnetic order in $LaCoO_{3-\delta}$ epitaxial films due to the interplay of epitaxial strain and oxygen vacancy ordering", 1–12 (2015).

Chapter 1: Introduction

1. Motivation: oxygen vacancies in transition metal oxides

Transition metal oxides (TMO's) are a family of compounds of with a wide spectrum of physical properties which are very promising for future applications in oxide electronics: ferromagnetism, antiferromagnetism, superconductivity, ferroelectricity, etc. They are also good candidates for devices because they are highly compatible and interfaces of these materials allow studying the interplay between different electric and magnetic effects [1]. The different interactions between the charge, spin, lattice and orbital degrees of freedom at oxide interfaces give rise to a wide variety of electronic phases, stemming from the combination of proximity, reduced dimensionality and strong correlations [2,3].

An additional degree of freedom than can strongly affect the properties of oxide films is the presence of point defects such as O vacancies. It is well known that TMO's grow with oxygen deficiencies, and oxygen stoichiometry can affect significantly the functional properties of the system either by the doping the materials or by the structural changes induced in the crystal lattice. For example, while stoichiometric $LaMnO_3$ is an antiferromagnetic insulator, experimental samples tend to be oxygen deficient and exhibit ferromagnetism [4]. Epitaxial strain due to lattice mismatch is another key player when studying the properties of thin films and interfaces. Unexpected behaviors can be ensured from strain fields. For example, the antiferromagnetic insulator $LuMnO_3$ has been reported to stabilize a ferromagnetic ground state when grown in epitaxial thin film form. In this case, the ferromagnetism is found close to the film substrate interface where strain effects are largest [5]. More recent studies of epitaxial $(La,Sr)CoO_3$ films on similarly lattice-matched $NdGaO_3$ and $(La,Sr)(Al,Ta)O_3$ (LSAT) substrates showed different saturation magnetization values [6]. In these studies, the authors demonstrate that the different oxygen stoichiometry of the films grown on the two different substrates can account for the enhancement of the magnetic properties. Particularly, Metha et al. studied the combined effects of epitaxial strain and defects on the magnetic properties of $LaCoO_3$ films. They demonstrated that both factors affect the magnetism of the samples in a close loop, since epitaxial strain induces the formation of oxygen vacancy ordering with geometries related to stress release mechanisms. They found that the stabilization of higher spin Co^{2+} and Co^{3+} states combined with an ordered oxygen vacancy superstructures can account for the ferromagnetic exchange interaction observed. In ferroelectric devices, oxygen vacancies allow the presence of memristive states since they are more mobile than cations in TMO's [7,8]. O vacancies in multiferroic tunnel junctions (MTJ's) are responsible for resonant tunneling in $La_{0.7}Sr_{0.3}MnO_3/BaTiO_3/La_{0.7}Sr_{0.3}MnO_3$ junctions through states in head-to-head domain walls [9].

These are a few examples of interest in spintronics, but there are other complex oxides of interest in fields such as energy materials and related devices. Colossal ionic conductivity can result from the 7% epitaxial strain between ZrO_2:Y_2O_3 ultrathin films and $SrTiO_3$ (STO). Barriocanal et al. proposed that the atomic reconstructions at the interface between highly dissimilar structures (fluorite and perovskite) provided both large number of carriers and a high-mobility plane, reporting a high lateral ionic conductivity with an enhancement of eight orders of magnitude near room temperature [10,11].

The density of O vacancies in all these compounds can be controlled during the growth process by in-situ annealings in vacuum at high temperature or by the introduction of tensile or compressive substrates that may force the structure to grow with an oxygen deficient content to minimize strains [12]. Thus, the motivation of this thesis harnessing this degree of freedom and exploiting new functionalities in heterostructures and thin films. We will focus on characterizing changes in the structure, electric and magnetic properties of different systems where a lack or disorder of the oxygen lattice is present. In the next sections of this introduction, the physical properties of chosen systems of interest in spintronics and energy are summarized. At the end of the chapter, the outline of the work included in this thesis is presented.

2. Multiferroic tunnel junctions

Spin-based electronics is an emerging field which exploits the quantum nature of electrons [13,14]. The spin of the electron is used as a magnetic degree of freedom to control the conduction. Manifestations of the spin are found in ferromagnetic metals, where an imbalance of spin populations at the Fermi surface can result in charge carrier spin polarization. Thus, magnetic fields can be used to manipulate spin polarized electrical currents, providing an additional channel of information as well as an additional degree of freedom for designing novel devices. In this context, and in good approximation, the currents of spin-up and spin-down electrons behave independently from each other with separate conduction channels. Spintronic devices display asymmetric behaviors due to different carrier densities and / or mobilities [15]. Typical spintronic devices have already made the way towards applications, e.g. the giant magnetoresistance read head [16,17], which detects magnetically stored data by measuring changes of resistance in the read head. Another important example of successful application related to data storage itself can be found in magnetic tunnel junctions (MTJs), which consist of two metallic ferromagnetic electrodes separated by a non-magnetic ultrathin insulating layer as we will explain in detail later in this section. If the barrier is made of a ferroelectric material, the device is called multiferroic tunnel junction. In this case the resistance can be affected and controlled by the application of both magnetic and electric fields. MFTJ's exhibit increased functionalities, simultaneously presenting: (i) tunnel magnetoresistance caused by the modulation of the tunnel conductance produced by the relative alignment of magnetizations of the ferromagnetic electrodes and (ii) tunnel electroresistance (TER) due to the modulation of the tunnel conductance by the ferroelectric polarization reversal [18,19]. The interplay between these two effects can strongly affect the interfacial properties of MFTJ's leading to large magnetoelectric effects, which can lead to the discovery of new effects and novel functionalities.

2.1. Electron tunneling

When two conductors M_1 and M_2 are separated by an ultrathin insulating barrier I, an applied voltage between them can give rise to a non-finite current across the barrier. The classical particle framework does not explain this phenomenon, so the dual wave-particle nature of electrons has to be taken into account. Within a quantum framework, the current flow can be explained by a non-zero probability of transmission of electrons across the insulating layer if the electronic wave function decay length is larger than the insulating layer thickness. Sommerfeld and Bethe in 1930 and Frenkel in 1933 evidenced experimentally the tunneling effect also in superconducting tunneling junctions [20,21].

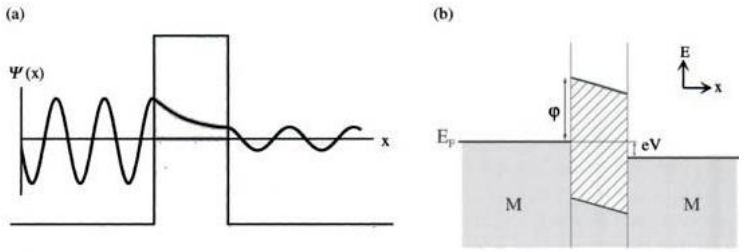

Figure 1. (a) Electron tunneling wave function in a metal-insulator-metal structure. (b) Energy diagram of the structure Potential diagram for a M-I-M structure with applied bias eV. Grey areas represent filled states and white correspond to empty states. The hatched area represents the forbidden gap in the insulator. Figure adapted from Reference [22].

In metal-insulator-metal (MIM) heterostructures, the current flow is measured as a function of the applied voltage across the junction. Figure 1 summarizes an illustration of the phenomenon. The ideal structure is modelled as a step potential as in Figure 1a., where the two metals will equilibrate their Fermi energies in absence of a voltage. When a bias V is applied across the MIM junction, there is a shift of a few eV of one Fermi level respect to the other, as displayed in Figure 1b. The tunneling current from the left electrode to the right one will then be given by:

$$I_{l\to r}(V) = \int_{-\infty}^{\infty} \rho_l(E)\rho_r(E+eV)|M|^2 f(E)[1-f(E+eV)]dE \quad [1]$$

Where ρ_l and ρ_r are the density of states in the left and right electrodes respectively at a given energy E, and $|M|^2$ is the matrix element which represents the probability of transmission through the barrier. The probability of having empty states in the left electrode is given by the Fermi-Dirac function *f(E)* and the probability of empty states in the right electrode is *1-f(E-eV)*. The total tunneling current is given by:

$$I = I_{l\to r} - I_{r\to l} \quad [2]$$

Where $I_{l\to r}$is the tunneling current from the left electrode to the right electrode and $I_{r\to l}$ is the tunneling current from the right electrode to the left electrode. Simmons calculated the tunnel current density, *J* [23]. He used the Wentzel–Kramers–Brillouin (WKB) approximation and calculated the matrix elements $|M|^2$ for an arbitrary barrier of average height $\bar{\varphi}$ above the Fermi level E_F. For T=0 (Fermi-Dirac functions are step functions) and using a free electron relation for $\rho_l(E)$, the result was:

$$J(V) = \frac{J_0}{d^2}\left(\bar{\varphi} - \frac{eV}{2}\right)e^{\left[-Ad\sqrt{\bar{\varphi}-\frac{eV}{2}}\right]} - \frac{J_0}{d^2}\left(\bar{\varphi} + \frac{eV}{2}\right)e^{\left[-Ad\sqrt{\bar{\varphi}+\frac{eV}{2}}\right]} \quad [3]$$

Where $A = 4\pi\sqrt{2m_e^*}/h$ and $J_0 = e/2\pi h$, are constants, m_e^* is the electron effective mass, d is the barrier thickness, $\bar{\varphi}$ is the average barrier height above the Fermi level, and V is the applied voltage. At moderate voltages, Simmons showed that $J \sim \alpha V + \beta V^3$. This result give rise to a parabolic dependence of the conductance G on voltage ($G \equiv dI/dV$) which is seen experimentally in tunnel junctions. However, this model does not take

into account the dependence of the current density on the electronic density of states (DOS). Thus, this simplification gives rise to an over-simplified result that does not often fit very well the behavior of real junctions [24,26].

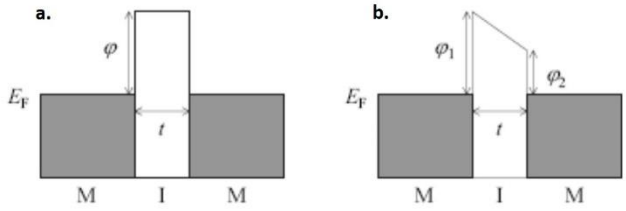

Figure 2. Schematic potential barrier for (a) Simmons model and (b) Brinkman model.

In practice, junctions with equal electrodes can present different interfaces properties leading to unequal energy profiles. To address this issue, Brinkman proposed a model with a trapezoidal potential barrier as shown in Figure 2b [27]. In this model the barrier is described by the width d and the potentials φ_1, φ_2 at the metal-insulator interfaces, where the potential spatial function is:

$$\varphi(x) = \varphi_1 + \frac{x}{t}(\varphi_2 - eV - \varphi_1) \quad [4]$$

If the applied voltage is $V \ll \varphi$, the tunnel conductance can be written as:

$$\frac{G(V)}{G\,(0)} = 1 - \frac{A_0 \Delta\varphi}{16\bar{\varphi}^{3/2}} eV + \frac{9A_0^2}{128\bar{\varphi}}(eV)^2 \quad [5]$$

where $A_0 = 4\pi d\sqrt{2m_e^*}/3\hbar$, $G(0) = \frac{e^2}{dh^2}\sqrt{2m_e^*}\,\bar{\varphi} e^{\left(\frac{-4\pi}{\hbar}\sqrt{2m_e^*\,\bar{\varphi}}\right)}$, $\Delta\varphi = \varphi_2 - \varphi_1$ is the barrier asymmetry, $\bar{\varphi} = \frac{\varphi_1+\varphi_2}{2}$ is the effective barrier height in eV. This equation is often used to fit experimental J(V) characteristics to obtain effective barrier heights and thicknesses.

2.2. Magnetic tunnel junctions

Magnetic tunnel junctions (MTJs) typically consist of a heterostructure where an ultrathin insulating barrier (a few nanometers thick) is sandwiched between two ferromagnetic metal layers. If a voltage is applied between the two metal electrodes across the insulator, electrons can tunnel through the barrier.

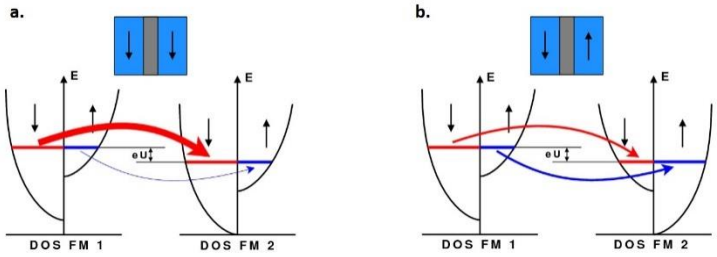

Figure 3. Schematic of the spin-dependent tunnelling process when the relative magnetization is (a) parallel and (b) antiparallel.

In a MTJ the tunneling current depends on several parameters. One of the most important ones is the relative orientation of the magnetizations of the two ferromagnetic electrodes, which can be controlled by an applied magnetic field (Figure 3). The resulting conduction phenomenon is called tunnelling magnetoresistance (TMR). The first TMR experiment was carried out by Jullière in 1975 using Co and Fe ferromagnetic films and a Ge barrier layer, reporting a sizable magnetoresistance at 4.2 K [28]. Considering that the spin of electrons is conserved in the tunneling process and tunneling of up- and down-spin electrons are two independent processes, Jullière assumed the conductance to occur via two independent spin channels. Thus, electrons with one spin state of the first ferromagnetic electrode would only be accepted by empty states with the same spin polarization in the second ferromagnetic electrode. If both electrodes are magnetized parallel (P), majority (minority) spins tunnel into majority (minority) states. But, if the two films are magnetized antiparallel (*AP*) the identity of the majority- and minority-spin electrons is reversed, so the majority spins of the first electrode tunnel to the minority states in the second layer and vice versa. The second assumption of Jullière was that the conductance for a particular spin orientation is proportional to the product of the effective (tunneling) density of states (DOS) of the two ferromagnetic electrodes, so, the conductance for both parallel and antiparallel relative alignments, G_P and G_{AP}, can be written as follows:

$$G_P \propto \rho_1^{\uparrow}\rho_2^{\uparrow} + \rho_1^{\downarrow}\rho_2^{\downarrow} \quad [6]$$

$$G_{AP} \propto \rho_1^{\uparrow}\rho_2^{\downarrow} + \rho_1^{\downarrow}\rho_2^{\uparrow} \quad [7]$$

Where $\rho_i^{\uparrow}$ and $\rho_i^{\downarrow}$ are the tunneling DOS of the ferromagnetic electrodes (designated by index i = 1, 2) for the majority- and minority-spin electrons. It follows from equations [6] and [7] that parallel- and antiparallel-magnetized MTJs have different tunnel conductances. TMR is then defined as the difference of conductances for parallel and antiparallel magnetization states, normalized by the antiparallel conductance. Using equations [6] and [7], the Jullière's formula results:

$$TMR = \frac{(G_P - G_{AP})}{G_{AP}} = \frac{(R_{AP} - R_P)}{R_P} = \frac{2P_1P_2}{(1 - P_1P_2)} \quad [8]$$

which expresses the TMR in terms of the effective spin polarization of the two ferromagnetic electrodes:

$$P_i = \frac{\rho_i^{\uparrow} - \rho_i^{\downarrow}}{\rho_i^{\uparrow} + \rho_i^{\downarrow}} \quad [9]$$

Besides the conventional spin polarized tunneling devices, the recent discovery of ferroelectricity at the nanoscale opened up the implementation of ferroelectric material as a barrier in tunnel junction devices, the so-called ferroelectric tunnel junctions. Ultrathin films of different compounds as $Pb(Zr_{0.2}Ti_{0.8})O_3$ (PZT), $BiFeO_3$, $(Li,Bi)MnO_3$, $PbTiO_3$ and $BaTiO_3$ have been reported to be ferroelectric [29-35]. The functionalities of MTJ's can therefore be extended by replacing the usual insulating barriers by a ferroelectric material.

2.3. Ferroelectric and multiferroic tunnel junctions.

Ferroelectric tunnel junctions are composed by two metal electrodes and an intermediate ultrathin layer (a few nanometers thick) of a ferroelectric (FE) material, which acts as the insulating barrier in the electron tunneling conduction process. The idea was formulated for the first time in 1971 by Esaki *et al*. [36]. However, the extended belief back then was that the critical thickness for ferroelectricity to be stable in a material was larger than the values necessary for tunneling to take place. Recent theoretical and experimental advances on perovskite ferroelectric oxide thin-films have demonstrated that in some cases ferroelectricity may persist in thickness ranges down to the 1 nm scale [37,35]. Therefore, ferroelectric tunneling mechanisms become available and result interesting both from the fundamental point of view and also for applications in the field of data storage. The application of an electric field across a ferroelectric film enables a polarization state that can be reversed applying the electric field in the opposite direction, giving rise to two logic states. Such switch of the ferroelectric polarization results in large changes in the tunnel resistance, property known as tunnel electroresistance (TER) [38].

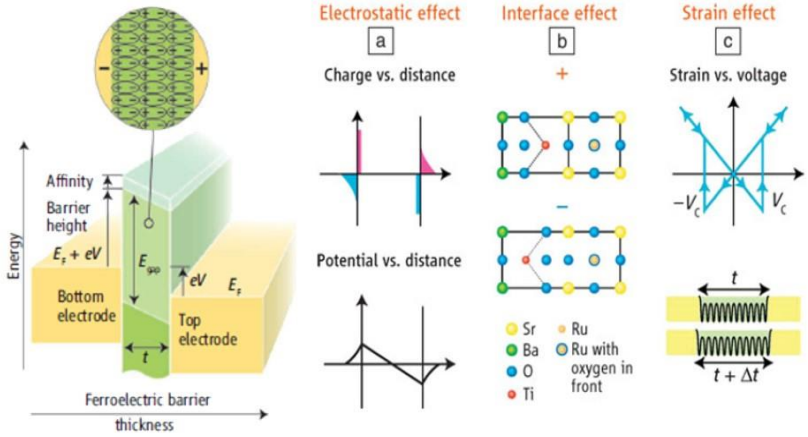

Figure 4. Schematic of a ferroelectric tunnel junction, adapted from reference [39].

The modulation of the tunnel conductance in MFTJ's can thus be controlled by three different factors, illustrated in Figure 4. The effects of the ferroelectric polarization are:

- A change in the electrostatic potential across the junction: The ferroelectric polarization surface charges cannot be completely screened by the adjacent metals and thus, the depolarization electric field is not zero [40]. In addition, if the metallic electrodes have different screening lengths, the potential profile will be asymmetric and thus the average height of the tunnel barrier will be not constant. This effect results in the modulation of the tunnel conductance a few orders of magnitude [35]. Also, recent experiments based on tunnel barriers combining a dielectric and a ferroelectric thin film have been proposed, where the dielectric layer acts as a switch depending on the direction of the ferroelectric polarization [41].
- The interfacial bonding strength: the ferroelectric polarization can reverse ionic displacements in the barrier. This effect modifies the interfacial bonding and thus, the density of states of the electrodes [42].
- The strain associated with the piezoelectric response: the effective barrier thickness may change due to structural distortions along the axis of the junctions caused by the applied bias. The ensuing tunnel current will be modulated since it depends on the barrier thickness.

In order to enhance the TER effect, several experiments have been performed. Zhwang et al. replaced one of the metal electrodes with a highly doped semiconductor in a FTJ, achieving values of electroresistance upon 10^4 [43]. Other improvements are the control of the domain dynamics demonstrated by Chanthbouala and co-workers, which allows the use of FTJ as memristive devices since the resistance can be continuously and reversibly modified. All these results can result in multilevel nonvolatile memories and adaptative networks that require synapse-like functions [44].

The natural forward step is the design of multiferroic tunnel junctions (MFTJ's) capable of exploiting simultaneously TER and TMR effects. Such devices would ideally give rise to a 4-resistance-state device, as shown in Figure 5. The resistance states can be switched with electric and magnetic fields. In MFTJ's, the spin-dependent and ferroelectric contributions to the transport properties is, in principle, independent. However, magneto-electrically driven effects at the interfaces would be very relevant relevant since magnetic reconstructions can take place and affect coupling and tunneling conductances.

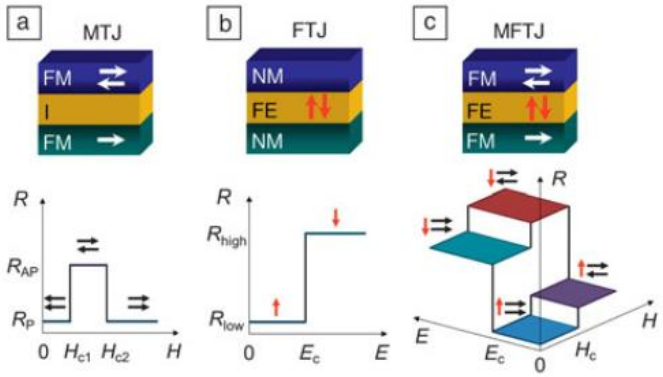

Figure 5. Schematic of a MFTJ adapted from reference [45].

The first demonstration of ferroelectric control of the interfacial spin polarization was observed by V. Garcia and co-workers [46]. They fabricated $La_{0.7}Sr_{0.3}MnO_3$ (LSMO) /$BaTiO_3$ (BTO)/Fe MTJ's and obtained a significant change in TMR with the ferroelectric polarization reversal. The change in the TMR amplitude was given by the change of the spin polarization at the Fe/$BaTiO_3$ interface and the induced magnetic moment on the interfacial Ti atoms [42][47]. The direction of the ferroelectric polarization can also reverse the signal of the TMR amplitude, as in LSMO/PZT/Co junctions due the modification of the spin density of states at the PZT/Co interface [48]. However, new trends rely on the modification of the barrier elements or on the introduction of ultrathin films of semiconductors between the barriers and the electrodes to produce magnetic phase transitions. For example, Yin et al. fabricated $La_{0.7}Sr_{0.3}MnO_3$/$BaTiO_3$/$La_{0.7}Sr_{0.3}MnO_3$ MFTJ's with an ultrathin film of $La_{0.5}Ca_{0.5}MnO_3$ (LCMO) between the barrier and the top electrode [49]. They tuned the ferromagnetic metallic phase to the antiferromagnetic anisotropic insulating phase of the LCMO by changing the direction of the ferroelectric polarization, which produced an enhancement of the TER driven by the modulation of the effective barrier thickness accompanied by a large change in the TMR. These results remark the importance and the wide possibilities emerging from barrier engineering in MFTJ's. Unfortunately, the possibility of controlling the polarization still has to overcome issues related to the presence of defects such as oxygen vacancies or, instead, take advantage of such factors for the design of new devices. In this framework, two different experiments will be proposed in this work aimed at exploring novel functionalities related to O point defects: the first one is the introduction of an oxygen deficient ferromagnetic barrier in MTJ's (Chapter 3). The second consists in the introduction of an ultrathin film of a deoxygenated cuprate between a ferroelectric barrier of $BaTiO_3$ and the ferromagnetic electrodes of $La_{0.7}Sr_{0.3}MnO_3$ (Chapter 4).

3. Ionic conductors for SOFC's

We will also devote some attention to devices related to the field of energy materials. During the last years, a vast amount of work has been dedicated to the family of materials known as ionic conductors. This attention has been motivated by the idea of promising applications in different solid state devices, such as gas sensors or supercondensers, among others [50][51]. However, the most relevant application currently can be found in the use of ionic conductors as electrolytes or electrodes in solid fuel cells. Currently, > 90% of telephone devices, tablets and computers incorporate lithium batteries as energy storage devices. Additionally, fuel cells constitute one of the main approaches to "clean energy" alternatives to fossil fuels [52][53][54].

Fuel cells are devices capable of turning chemical energy into electric energy without producing major contaminating emissions to the atmosphere. Technologic applications of solid oxide fuel ells (SOFC) combine such non-contaminant energy production with flexibility in the election of fuel (hydrogen, carbon monoxide, etc.). However, the most important limitation for a definitive implementation of these devices is the poor ionic conductivity at room temperature of solid state electrolites, such as yttria-stabilized zirconia ZrO_2/Y_2O_3 (YSZ). The operation temperature of YSZ is nowadays of 800°C, which has been in part overcome reaching values of 500-700°C [53][55][56][54][57]. Such high operation temperatures preclude a wide spread of applications. The best alternatives proposed so far include other oxide compounds such as Gd-doped ceria. The practical interest is fueled as well from the standpoint of basic research. The complex many-body interactions taking place in ionic conductors pose a challenge when trying to understand the dynamics of mobile ions in solid electrolites. One of the most accepted tendencies so far assumes that the dynamics of the mobile ions are driven by correlations established during their diffusive long range movement. In this context, it has been found that positional disorder is related to enhancements of the ionic conductivity of these materials, since there is an increasing number of available locations for mobile ions in the structure.

3.1. Ionic conductivity

Ionic conductors are a singular kind of materials where conduction process mechanisms are due to the jump of ions in a diffusion process from an occupied position into a vacant one. The conduction process is thermally activated, which implies that it exhibits a dependence with temperature of the kind:

$$\sigma \sim \exp\left(-\frac{E_a}{k_B T}\right) \quad [10]$$

Where E_a is the activation energy, k_B is the Boltzmann constant and T the temperature. This simple description has important implications. The first one is that the charge carriers are heavier and bigger than electrons, and thus, conduction will take place at lower speeds. Hence, conductivity values will be lower than those characteristic of metals. The second implication is that the atoms are constitutive elements of the material structure, so there must be vacancy and accessible positions within the fixed matrix that is the crystal lattice. Charge carriers have to move from their sites into vacancies in order to be able to move through the material. There must be always a minimum number or accessible positions for the movement of atoms under applied

fields. Moreover, in ionic conductors with high values of conductivity, there is a characteristic quantity known as positional disorder: in these materials, the number of positions in which the ion can be placed is bigger than the mobile ions, so there is not optimal configuration to distribute the ions amongst those positions.

In order to understand to the ionic dynamics inside a solid, the response to applied electric fields is the most commonly used probe. In particular, measurements of electric conductivity, σ*(ω), allow the extraction of the relaxation function of the electric field in the frequency range. The frequency dependence of the electric conductivity in ionic conductors is given by the following expression [58]:

$$\sigma^*(\omega) = \sigma_{dc}\left[1 + \left(\frac{j\omega}{\omega_p}\right)^n\right] + j\omega\varepsilon_0\varepsilon_\infty, 0 \leq n \leq 1$$

[11]

Where ε_0 is the dielectric permittivity in vacuum and ε_∞ is the dielectric permittivity at high frequencies. At low frequencies, the real part is independent of the frequency itself and its value, σ_{dc}, is known as dc conductivity. The *n* exponent is characteristic of the potential dependence observed at high frequencies and it is a measurement of the interaction or correlation between the ions during the diffusion process. The frequency ω_p is a characteristic frequency observed for the regime change from dc to the potential dependence with frequency. The dc conductivity and the characteristic frequency are activated thermally with an activation energy E_a:

$$\sigma_{dc} \propto \sigma_\infty \exp(-E_a/k_B T)$$

[12]

The inverse of ω_p is the relaxation constant of the electric field inside the material and it is activated thermally with the same activation energy than σ_{dc}.

3.2. Strained and/or disordered heterostructures structures based on ZrO_2/Y_2O_3 (YSZ): state of the art.

Alternatives to improve the capabilities of ionic conducting systems can be found in the fabrication of thin films, where one of the dimensions of the material is reduced down to the nanometer scale [59]. It has been reported that nanostructured zircona presents an electric conductivity enhanced more than two orders of magnitude when compared to monocrystalline samples [60]. The fabrication of heterostructures combining YSZ with different materials allow exploring the determining effects of interfaces. Maier and co-workers have reported an increase of more than three orders or magnitude in the ionic conductivity of CaF_2 / BaF_2 superlattices when the thickness of the layers is reduced to 50 nm [61][62]. Kosacki and co-workers have been able to grow ultrathin films of textured YSZ with thicknesses below 15 nm. Within these thickness ranges, an interfacially enhanced diffusion process has been proposed, which could induce values of 3 mS cm^{-1} at room temperature, with activation energies would near 0.5 eV [63].

Epitaxial strain has also been shown to constitute a key parameter to tune the enhancement of the ion mobility at interfaces. Several experimental and theoretical investigations have focused on the increase of the ionic conductivity generated by epitaxial strain [64]. However, models find that strain by itself cannot account for the large increase of the conductivity observed experimentally. Korte and co-workers have made use of static models to evaluate changes in the migration volume associated to the density of misfit dislocations caused by strain relaxation. They have pointed out that strain by itself can only account for two or three orders of magnitude conductivity increase in YSZ/STO heterostructures [65]. On the other hand, de Souza and colleagues, have shown that strain effects on the free energy for migration are able to account for a conductivity increase up to five orders of magnitude (of the eight reported experimentally by Garcia-Barriocanal et al. in YSZ/STO heterostructures). Furthermore, from a study of the effects of biaxial strain on the oxygen diffusivity using combined density-functional theory (DFT) calculations and kinetic Montecarlo (KMC), Yildiz and collaborators conclude that bonding reconfiguration poses an upper limit to the effects of epitaxial strain in explaining conductivity enhancements [68].

However, these models are based on stressing *bulk* structure, i.e., they do not explicitly include the presence of interfaces which incorporate important additional ingredients related to the chemical and structural compatibility of the merging lattices. Density-functional theory simulations explicitly considering the presence of the interface by introducing heterogeneous YSZ/STO super cells have shown that the combination of epitaxial strain and the merging of dissimilar structures can be key in generating extreme degrees of disorder in the oxygen sub-lattice within the region close to the interface, which would explain the highly conducting interface [69] [64][70]. In this thesis, we will address the study of lattice discontinuity itself via the growth of unstrained YSZ thin films on a lattice parameter matched substrate ($YAlO_3$) in order to study the conduction mechanisms related to disorder resulting from assymetric interfaces.

4. Outline of this thesis

Within the framework presented above, the work carried out in this thesis is organized in the following chapters:

- Chapter 2: this chapter is dedicated to the description of the experimental techniques used for this work. There is an extensive introduction to the components and mechanics of the sputtering growth system and characterization techniques such as aberration corrected electron microscopy, along with a description of other experimental techniques used to a lesser extent to fabricate the devices or make specific measurements.

- Chapter 3: This chapter is dedicated to a study of the magnetic properties of manganite/cobaltite hetrostructures. Important changes in the magnetic anisotropy of LSMO thin films are triggered by the presence of oxygen vacancies of $LaCoO_3$ (LCO) buffer layers. An in-depth study of the structural and electronic properties will be presented. For this aim, in the first place, a study of $La_{1-x}Sr_xCoO_3$ thin films on different substrates is carried out using advanced electron microscopy and spectroscopy techniques. Next, we will fabricate devices consisting on MTJ's combining $La_{0.7}Sr_{0.3}MnO_3$ electrodes with an insulating LCO barrier. As we will show, the strain induced in the barrier and the presence of oxygen vacancies has important implications in the magnetic anisotropy of the $La_{0.7}Sr_{0.3}MnO_3$ upper electrode which will, in turn, help us explain the low TMR values measured in these devices.

- Chapter 4: To improve the capabilities of multiferroic tunnel junctions, we have fabricated asymmetric MFTJ's by further engineering of the ferroelectric barrier. We will introduce an ultrathin film of a deficient oxygen cuprate adjacent to the insulating ferroelectric $BaTiO_3$ barrier. The high density of oxygen vacancies in the cuprate will provide a new degree of freedom resulting in additional resistance states in the system, improving both the TMR and TER properties.

- Chapter 5: Last, we will turn to applications in the field of energy related materials. This chapter will focus on the study of the properties of epitaxial Y_2O_3:ZrO_2 (YSZ) films grown on virtually mismatch free substrates. We will force the matching of dissimilar fluorite/perovskite structures at an interface free of major strain fields in order to study the interfacial contribution to the conductivity. Our YSZ films will be deposited on highly insulating $YaAlO_3$ substrates. A study of the interfacial effects will be presented based on experimental measurements combining dielectric spectroscopy techniques and atomic resolution electron microscopy.

Finally, the last chapter summarizes the major conclusions of this work. There is also an attached annex including the list of publications resulting from this thesis (including those currently submitted and under preparation) including conference contributions. Also, we will include a description of short stays that have taken place within the frame of collaborations with international groups at major research institutions abroad.

5. References

[1] J. Mannhart and D. G. Schlom, "Oxide Interfaces: An Opportunity for Electronics" *Science* **327**, 1607–1611 (2010).

[2] Y. Tokura, "Correlated-Electron Physics in Transition-Metal Oxides" *Phys. Today*, **56**, 50 (2003).

[3] N. F. Mott, "Metal-insulator transition", *Rev. Mod. Phys.* **40**, 677–683, (1968).

[4] R. Zhao, K. Jin, Z. Xu, H. Guo, L. Wang, C. Ge, H. Lu, and G. Yang, "The oxygen vacancy effect on the magnetic property of the $LaMnO_{3-\delta}$ thin films", *Appl. Phys. Lett.* **102**, 122402 (2013).

[5] J. S. White, M. Bator, Y. Hu, H. Luetkens, J. Stahn, S. Capelli, S. Das, M. Dbeli, T. Lippert, V. K. Malik, J. Martynczuk, A. Wokaun, M. Kenzelmann, C. Niedermayer, and C. W. Schneider, "Strain-induced ferromagnetism in antiferromagnetic $LuMnO_3$ thin films", *Phys. Rev. Lett.* **111**, 1–5 (2013).

[6] Y.-M. Kim, J. He, M. D. Biegalski, H. Ambaye, V. Lauter, H. M. Christen, S. T. Pantelides, S. J. Pennycook, S. V. Kalinin, and A. Y. Borisevich, "Probing oxygen vacancy concentration and homogeneity in solid-oxide fuel-cell cathode materials on the subunit-cell level" *Nat. Mater.* **11**, 888–894 (2012).

[7] R. Waser and M. Aono, "Nanoionics-based resistive switching memories", *Nat. Mater.* **6**, 833–40 (2007).

[8] R. Waser, R. Dittmann, C. Staikov, and K. Szot, "Redox-based resistive switching memories nanoionic mechanisms, prospects, and challenges", *Adv. Mater.* **21**, 2632–2663 (2009).

[9] G. Sánchez-Santolino, J. Tornos, D. Hernández-Martín, J. I. Beltrán, C. Munuera, M. Cabero, A. Pérez-Muñoz, F. Monpean, M. Garcia-Hernandez, Z. Sefrioui, C. León, S. J. Pennycook, M. C. Muñoz, M. Varela, and J. Santamaría, "Realization of a ferroelectric-domain-wall tunnel junction", (*Paper Accepted in Nature Nanotechnology.)*

[10] J. Garcia-Barriocanal, a Rivera-Calzada, M. Varela, Z. Sefrioui, E. Iborra, C. Leon, S. J. Pennycook, and J. Santamaria, "Colossal ionic conductivity at interfaces of epitaxial ZrO2:Y2O3/SrTiO3 heterostructures" *Science* **321**, 676–80 (2008).

[11] A. Rivera-Calzada, M. R. Diaz-Guillen, O. J. Dura, G. Sanchez-Santolino, T. J. Pennycook, R. Schmidt, F. Y. Bruno, J. Garcia-Barriocanal, Z. Sefrioui, N. M. Nemes, M. Garcia-Hernandez, M. Varela, C. Leon, S. T. Pantelides, S. J. Pennycook, and J. Santamaria, "Tailoring interface structure in highly strained YSZ/STO heterostructures," *Adv. Mater.* **23**, 5268–5274 (2011).

[12] V. V Mehta, N. Biskup, C. Jenkins, E. Arenholz, M. Varela, and Y. Suzuki, "Long-range ferromagnetic order in $LaCoO_{3-\delta}$ epitaxial films due to the interplay of epitaxial strain and oxygen vacancy ordering", 1–12 (2015).

[13] S. Yunoki, A. More, E. Dagotto, S. Okamoto, S. S. Kancharla, and A. Fujimori, "Electron Doping of Cuprates via Interfaces with Manganites," *Phys. Rev. B* **76**, 064532 (2007).

[14] D. Niebieskikwiat, L. E. Hueso, J. A. Borchers, N. D. Mathur, and M. B. Salamon, "Nanoscale magnetic structure of ferromagnet/antiferromagnet manganite multilayers", *Phys. Rev. Lett.* **99,** 247207 (2007).

[15] J. Salafranca, M. J. Calderón, and L. Brey, "Magnetoresistance in an all-manganite heterostructure", *Phys. Rev. B* **77**, 014441 (2008).

[16] J. Garcia-Barriocanal, F. Y. Bruno, A. Rivera-Calzada, Z. Sefrioui, N. M. Nemes, M. Garcia-Hernández, J. Rubio-Zuazo, G. R. Castro, M. Varela, S. J. Pennycook, C. Leon, and J. Santamaria, "'Charge leakage' at $LaMnO_3/SrTiO_3$ interfaces," *Adv. Mater* **22**, 627–632 (2010).

[17] J. Chakhalian, J. W. Freeland, H.-U. Habermeier, G. Cristiani, G. Khaliullin, M. van Veenendaal, and B. Keimer, "Orbital reconstruction and covalent bonding at an oxide interface", *Science* **318**, 1114–1117 (2007).

[18] M. Y. Zhuravlev, S. S. Jaswal, E. Y. Tsymbal, and R. F. Sabirianov, "Ferroelectric switch for spin

injection," *Appl. Phys. Lett.* **87**, 1–3 (2005).
[19]M. Y. Zhuravlev, S. Maekawa, and E. Y. Tsymbal, "Effect of spin-dependent screening on tunneling electroresistance and tunneling magnetoresistance in multiferroic tunnel junctions", *Phys. Rev. B* **81**, 10 (2010).
[20]J. Frenkel, "On the electrical resistance of contacts between solid conductors," *Phys. Rev.* **36**, 1604–1618 (1930).
[21]I. Giaever and K. Megerle, "Study of superconductors by electron tunneling," *Phys. Rev.* **122**, 1101–1111 (1961).
[22]F. Group, *Spin transport magnetism.* Edited by. 2012.
[23]J. G. Simmons, "Generalized Formula for the Electric Tunnel Effect between Similar Electrodes Separated by a Thin Insulating Film" *J. Appl. Phys.* **34**, 1793–1803 (1963).
[24]W. A. Harrison, "Tunneling from an independent-particle point of view" *Phys. Rev.* **123**, 85–89 (1961).
[25]J. Bardeen, "Tunnelling From a Many-Particle Point of View" *Phys. Rev. Lett.* **6**, 57–59 (1961).
[26]S. Zhang and P. M. Levy, "Models for magnetoresistance in tunnel junctions" *Eur. Phys. J. B* **10**, 599 (1999).
[27]W. F. Brinkman, R. C. Dynes, and J. M. Rowell, "Tunneling conductance of asymmetrical barriers", *J. Appl. Phys.* **41**, 1915–1921, (1970).
[28]M. Julliere, "Tunneling between ferromagnetic films", *Phys. Lett. A* **54,** 225–226 (1975).
[29]A. V. a. V. Bune, L. M. L. M. Blinov, V. M. M. Fridkin, S. Ducharme, S. P. Palto, A. V. Sorokin, S. G. Yudin, and A. Zlatkin, "Two-dimensional ferroelectric films", *Nature* **391**, 45 (1998).
[30]T. Tybell, C. H. Ahn, and J.-M. Triscone, "Ferroelectricity in thin perovskite films", *Appl. Phys. Lett.* **75**, 856–858 (1999).
[31]D. D. Fong, "Ferroelectricity in Ultrathin Perovskite Films", *Science* **304**, 1650–1653 (2004).
[32]H. Béa, M. Bibes, S. Cherifi, F. Nolting, B. Warot-Fonrose, S. Fusil, G. Herranz, C. Deranlot, E. Jacquet, K. Bouzehouane, and A. Barthélémy, "Tunnel magnetoresistance and robust room temperature exchange bias with multiferroic $BiFeO_3$ epitaxial thin films", *Appl. Phys. Lett.* **89**, 3–6 (2006).
[33]Y. H. Chu, T. Zhao, M. P. Cruz, Q. Zhan, P. L. Yang, L. W. Martin, M. Huijben, C. H. Yang, F. Zavaliche, H. Zheng, and R. Ramesh, "Ferroelectric size effects in multiferroic $BiFeO_3$ thin films," *Appl. Phys. Lett.* **90**, 1–3 (2007).
[34]M. Gajek, M. Bibes, S. Fusil, K. Bouzehouane, J. Fontcuberta, A. Barthélémy, and A. Fert, "Tunnel junctions with multiferroic barriers" *Nat. Mater.* **6**, 296–302 (2007).
[35]V. Garcia, S. Fusil, K. Bouzehouane, S. Enouz-Vedrenne, N. D. Mathur, a Barthélémy, and M. Bibes, "Giant tunnel electroresistance for non-destructive readout of ferroelectric states" *Nature* **460**, 81–84 (2009).
[36]L. Esaki, R. B. Laibowitz, and P. J. Stiles, "Polar switch," *IBM Tech. Discl. Bull.*, **13**, 2161 (1971).
[37]J. Junquera and P. Ghosez, "Critical thickness for ferroelectricity in perovskite ultrathin films," *Nature* **422**, 506–509 (2003).
[38]M. Y. Zhuravlev, R. F. Sabirianov, S. S. Jaswal, and E. Y. Tsymbal, "Giant electroresistance in ferroelectric tunnel junctions" *Phys. Rev. Lett.* **94**, 1–4 (2005).
[39]E. Y. Tsymbal and H. Kohlstedt, "Tunneling across a ferroelectric" *Science* **313**, 181–3 (2006).
[40]T. M. Shaw, "The properties of ferroelectric films at small dimensions,"*Annu. Rev. Mater. Sci.* **30**, 263 (2000).
[41]A. Gruverman, D. Wu, H. Lu, Y. Wang, H. W. Jang, C. M. Folkman, M. Y. Zhuravlev, D. Felker, M. Rzchowski, C. B. Eom, and E. Y. Tsymbal, "Tunneling electroresistance effect in ferroelectric tunnel junctions at the nanoscale," *Nano Lett.* **9**, 3539–3543 (2009).
[42]J. P. Velev, C. G. Duan, K. D. Belashchenko, S. S. Jaswal, and E. Y. Tsymbal, "Effect of ferroelectricity

on electron transport in Pt/$BaTiO_3$/Pt tunnel junctions", *Phys. Rev. Lett.* **98**, 3–6 (2007).
[43]H. Kohlstedt, N. A. Pertsev, and R. Waser, "Size Effects on Polarization in Epitaxial Ferroelectric Films and the Concept of Ferroelectric Tunnel Junctions Including First Results", *MRS Proc.* **688**, C6.5.1 (2001).
[44]J. Rodriguez Contreras, H. Kohlstedt, U. Poppe, R. Waser, C. Buchal, and N. A. Pertsev, "Resistive switching in metal-ferroelectric-metal junctions", *Appl. Phys. Lett.* **83**, 4595–4597 (2003).
[45]Z. Wen, C. Li, D. Wu, A. Li, and N. Ming, "Ferroelectric-field-effect-enhanced electroresistance in metal/ferroelectric/semiconductor tunnel junctions" *Nat Mater.* **12**, 617–621 (2013).
[46]S. D. Ha and S. Ramanathan, "Adaptive oxide electronics: A review," *J. Appl. Phys.* **110**, (2011).
[47]E. Y. Tsymbal, a. Gruverman, V. Garcia, M. Bibes, and a. Barthélémy, "Ferroelectric and multiferroic tunnel junctions", *MRS Bull.* **37**, no. February, 138–143 (2012).
[48]V. Garcia, M. Bibes, L. Bocher, S. Valencia, F. Kronast, a Crassous, X. Moya, S. Enouz-Vedrenne, a Gloter, D. Imhoff, C. Deranlot, N. D. Mathur, S. Fusil, K. Bouzehouane, and a Barthélémy, "Ferroelectric control of spin polarization", *Science* **327**, 1106–1110 (2010).
[49]S. Valencia, a. Crassous, L. Bocher, V. Garcia, X. Moya, R. O. Cherifi, C. Deranlot, K. Bouzehouane, S. Fusil, a. Zobelli, a. Gloter, N. D. Mathur, a. Gaupp, R. Abrudan, F. Radu, a. Barthélémy, and M. Bibes, "Interface-induced room-temperature multiferroicity in $BaTiO_3$", *Nat. Mater.* **10**, 753–758 (2011).
[50]D. Pantel, S. Goetze, D. Hesse, and M. Alexe, "Reversible electrical switching of spin polarization in multiferroic tunnel junctions," *Nat. Mater.* **11**, 289–293 (2012).
[51]Y. W. Yin, M. Raju, W. J. Hu, X. J. Weng, X. G. Li, and Q. Li, "Coexistence of tunneling magnetoresistance and electroresistance at room temperature in $La_{0.7}Sr_{0.3}MnO_3$/(Ba, Sr)TiO_3/$La_{0.7}Sr_{0.3}MnO_3$ multiferroic tunnel junctions", *J. Appl. Phys.* **109**, 3–6 (2011).
[52]J. B. Goodenough, "Ceramic technology: Oxide-ion conductors by design", *Nature* **404**, 821–823 (2000).
[53]V Chadwick, "Solid progress in ion conduction.," *Nature* **408**, 925–6 (2000).
[54]R. M. Ormerod, "Solid oxide fuel cells", *Chem. Soc. Rev.* **32**, 17–28 (2003).
[55]J. B. Goodenough, "Oxide-Ion Electrolytes", *Annu. Rev. Mater. Res.* **33**, 91–128 (2003).
[56]J. W. Fergus, "Electrolytes for solid oxide fuel cells," *J. Power Sources*, **162**, 30–40 (2006).
[57]N. P. Brandon, S. Skinner, and B. C. H. Steele, "Recent Advances in Materials for Fuel Cells", *Annu. Rev. Mater. Res.* **33**, 183–213 (2003).
[58]Z. Shao and S. M. Haile, "A high-performance cathode for the next generation of solid-oxide fuel cells", *Nature* **431**, 170–173 (2004).
[59]Y. Yoo, "Fabrication and characterization of thin film electrolytes deposited by RF magnetron sputtering for low temperature solid oxide fuel cells," *J. Power Sources* **160**, 202–206 (2006).
[60]K. L. Ngai and A. K. Rizos, "Microscopic Explanation of the Non-Arrhenius Conductivity in Glassy Fast Ionic Conductors", *Phys. Rev. Lett.* **76**, 1296–1299 (1996).
[61]A. K. Jonscher, *Dielectric relaxation in solids*, Chelsea Di. London, 1983.
[62]A. Rivera, J. Santamaría, and C. León, "Electrical conductivity relaxation in thin-film yttria-stabilized zirconia," *Appl. Phys. Lett.* **78**, 610 (2001).
[63]I. Kosacki, B. Gorman, and H. U. Anderson, "No Title," *Electrochem. Soc. Proc.*, vol. 97, p. 631, 1998.
[64]J. Maier, "Point-defect thermodynamics and size effects", *Solid State Ionics* **131**, 13–22 (2000).
[65]N. Sata, K. Eberman, K. Eberl, and J. Maier, "Mesoscopic fast ion conduction in nanometre-scale planar heterostructures", *Nature* **408**, 946–9 (2000).
[66]I. Kosacki, C. M. Rouleau, P. F. Becher, J. Bentley, and D. H. Lowndes, "Nanoscale effects on the ionic conductivity in highly textured YSZ thin films", *Solid State Ionics* **176**, 1319–1326 (2005).
[67]A. Kushima and B. Yildiz, "Oxygen ion diffusivity in strained yttria stabilized zirconia: where is the fastest strain?," *J. Mater. Chem.* **20**, 4809 (2010).

[68]T. J. Pennycook, M. J. Beck, K. Varga, M. Varela, S. J. Pennycook, and S. T. Pantelides, "Origin of colossal ionic conductivity in oxide multilayers: Interface induced sublattice disorder", *Phys. Rev. Lett.* **104**, 1–4 (2010).
[69]T. J. Pennycook, M. P. Oxley, J. Garcia-Barriocanal, F. Y. Bruno, C. Leon, J. Santamaria, S. T. Pantelides, M. Varela, and S. J. Pennycook, "Seeing oxygen disorder in YSZ/$SrTiO_3$ colossal ionic conductor heterostructures using EELS," *Eur. Phys. J. Appl. Phys.* **54**, 33507 (2011).
[70]F. Li, R. Lu, H. Wu, E. Kan, C. Xiao, K. Deng, and D. E. Ellis, "The strain effect on colossal oxygen ionic conductivity in nanoscale zirconia electrolytes: a first-principles-based study", *Phys. Chem. Chem. Phys.*, **15**, 2692–7 (2013).

Chapter 2: Experimental techniques

This chapter includes a summary of all the experimental techniques used including growth, structural characterization and measurement of physical properties (electronic and ionic transport, magnetic measurements, etc).

1. RF Sputtering System

All the samples measured along this thesis have been grown with a high pressure pure oxygen sputtering system. This is a most appropriate technique for the growth of epitaxial films of complex oxides [1]. Growth takes place in a vacuum chamber in which a high purity oxygen gas is introduced at a pressure between 2.9-3.2 mbar, after a preliminary evacuation cleaning process reaching pressures of 10^{-6} mbar. During the growth process a constant flow of pure oxygen gas is maintained. Materials to be sputtered come from pellets known as targets. They are switched on by the application of a RF (for insulators) or a DC (conducting materials) power supply to ionize the oxygen gas flowing through the chamber. The RF power supply is used to avoid charge accumulation at the surface of the insulating targets. An oxygen plasma is formed under the target, as shown in Figure 1. Oxygen ions will be sent by the electric field towards the target surface, sputtering atoms away from it. The extracted atoms will be carried by the gaseous phase and deposited on the substrate. The high oxygen pressure prevents possible re-sputtering and substrate milling, and favors a complete thermalization, reaching very low growth rates (0.5-1nm/min). On the other hand, the substrate high temperature assures high diffusivities for the ions on the surface, yielding an ordered growth process of the films with good structural quality. The heating device is an Inconel furnace refrigerated and screened which reaches temperatures of 1000 C in an oxygen pure atmosphere. The furnace controller allows programming the thermal history of the sample before, during and after the growth process.

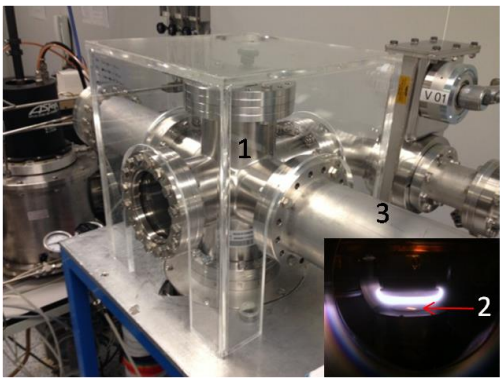

Figure 1. High O_2 pressure sputtering system. 1. Chamber, 2. Oxygen plasma of a LSMO target placed on the furnace with two STO substrates (marked with a red arrow) during regular operation, 3. Arm, loaded with different targets.

2. X-ray diffraction.

X- ray diffraction (XRD) is a non-destructive technique for the structural analysis of a wide range of materials. It allows the determination of the precise lattice parameters, thickness of individual and multiple layers, sometimes defects, etc. XRD is based on the optical interferences produced when a monochromatic radiation goes through a slit of finite thickness similar to the wavelength of the incident radiation. X-rays have wavelengths of Ångströms, same as interatomic distances in crystal lattices. All of our XRD patterns have been obtained at the CAI C.C. Químicas (UCM) using a Cu tube (λ_x=0.15418 nm) operating at 45kV and 40 mA.

2.1. X-Ray diffraction

A crystal lattice is formed by families of atomic planes (*hkl*), which are separated a distance d_{hkl}. In some circumstances, when an incident beam reaches the crystal each family of planes may reflect the incident radiation, provided the reflected radiation interferes constructively as shown in the scheme of Figure 2.

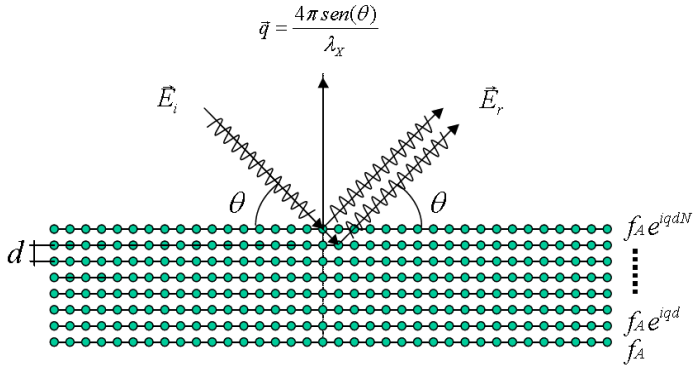

Figure 2. Bragg reflection picture for a monocrystalline crystal where d is the interatomic distance. The reflected beams in two adjacent planes go over an optical path difference of $2d_{hkl}sen\lambda$.

This constructive interference condition is met when the difference in the optical path of x-rays reflected in two adjacent planes, which is given by 2dsenθ (where θ is the angle between the incident beam and the family planes considered) is an integer number of wavelengths, λ. Therefore, the condition for a constructive interference of the incident radiation, summarized by Bragg's law [2, 3] is:

$$2d_{hkl} \sin\theta = n\lambda_x \quad [1]$$

Where d_{hkl} is the interplanar distance corresponding to the family planes with a {hkl} index, θ is the radiation incident angle, λ is the x-rays wavelength and n is an integer number which accounts for the

reflection order. For epitaxial, monocrystalline films (textured samples), the only family planes in Bragg position will be the parallel to the surface of the substrate. This way, we obtain peaks corresponding to the (001) direction, and hence, the family planes {hkl} perpendicular to the c axis.

XRD allows obtaining information of the structure of materials at the atomic scale with a great degree of accuracy. This information is averaged on large lateral extensions, given by a parameter known as structural length coherence, ξ. This length can be evaluated from the peaks full width at half-maximum (FWHM) with the Scherrer formula [3]:

$$\xi = \frac{0.9\lambda}{bcos\theta}$$

[2]

Where b is the FWHM of the corresponding peak and θ is the reflection angle. The incident angle of the X-rays is swept between θ-2θ using the Bragg geometry. At the same time, the sample rotates with a constant angular speed synchronized with the angular speed of the detector, which is 2θ, so the radiation detected corresponds to the direction of reflection.

2.1.1. X-Ray diffraction in superlattices

A high quality heterostructure made by a periodic repetition of two (or more) materials stacked coherently is known as a superlattice. For such samples, additional intensity peaks will appear in the diffraction pattern around each Bragg reflection. They are known a satellite peaks. The satellite positions are related with the artificial periodicity of the superlattice, which is called modulation. When the superlattice is comprised of bilayers of two materials, A and B, it is defined by [4]:

$$\Lambda = N_A c_A + N_B c_B$$

[3]

Where c_A and c_B are the lattice parameters in the growth direction and N_A and N_B are the number of unit cells, for materials A and B, respectively. The diffraction maxima associated to the superstructure only appear when the structural coherence in the perpendicular direction of the layers is larger than the modulation length ($\xi > \Lambda$). The superlattice satellite peaks are indexed, for convenience, around the average lattice constant of the bilayer:

$$2\frac{sin\theta}{\lambda_x} = \frac{1}{d} \pm \frac{n}{\Lambda}$$

[4]

Where n is the integer number which indexes the satellite peak around the Bragg peak and the averaged lattice parameter is provided by:

$$\bar{d} = \frac{\Lambda}{(N_A + N_B)}$$

[5]

Some values can be directly determined by means of the position of the peaks, such as $\bar{d}$, Λ and ξ.

2.2. SAXRD: Small angle X-ray diffraction

When a grazing incidence geometry is used, small angle X-ray diffractograms are obtained (with angles $2q \leq 10^{o}$). Under a Bragg geometry, the dispersion vector length corresponds to distances which are larger than the spacing between the crystallographic family planes of the material under study:

$$\frac{1}{d} = \frac{2sin\theta}{\lambda}$$

[6]

Where λ=1.54 Å. Therefore, the distances d that give rise to diffraction phenomena will typically satisfy the condition $d \leq 10$ Å, so the contrast is independent of the crystalline structure. In these conditions, X-rays are mostly sensitive to the chemical composition of the material through the refraction index, which is proportional to the averaged electronic density [5]. This refraction index is a complex number which can be written as $n=1-\delta-i\beta$, being:

$$\delta = \frac{\rho_N r_e \lambda^2}{2\pi}(f_0 + \Delta f')$$

[7]

$$\beta = \frac{\rho_N r_e \lambda^2}{2\pi}\Delta f''$$

[8]

Where r_N is the atomic density, r_e is the classical radius of the electron ($r_e=2.818\cdot10^{-5}$ Å), λ is the wave length of the X-rays, f_0 is the atomic dispersion factor, and $\Delta f'$ and $\Delta f''$ are the corrections that take into account the anomalous dispersion. The real part of the refraction index is written as 1-d, and its value in the case of complex oxides is $2d=3\cdot10^{-5}$.

When a thin film is irradiated by an X-ray beam, a part of the incident radiation is reflected at the surface, while a part of it will penetrate. The penetrating radiation in the material will be reflected at the interface film-substrate and will head towards the top surface again. When both beams interfere, a diagram comprised of maxima and minima (finite size peaks) will emerge. The X-ray beam traverses larger distances in the film than in high angle incidence, thus it is sensitive to changes in the refraction index through the material. It results in a deviation on the trajectory described by the Snell law:

$$n_1 sen(\alpha_1) = n_2 sen(\alpha_2)$$

[9]

Where n_1 and n_2 correspond to the different refraction index of the first and the second medium respectively while and α_1 is the angle between the incident beam in the second medium and the normal vector while α_2 is the angle between the refracted beam in the second medium and the normal vector. Maxima and minima diffraction peaks appear when the difference between the optical path of the reflected beams at the interfaces film-air and film-substrate is an integer number of wave length.

$$\Gamma=2n_1 d cos(\beta) = m\lambda$$

[10]

Where Γ is the difference between optical paths, n_1 is the refraction index of the material, d is the thickness of the film and λ is the wavelength of the incident beam. The value of m depends on the film refraction index and the material of the substrate chosen for deposition. To preserve the tangential component of an electromagnetic wave the condition imposed results in a change in the phase of π when the wave is reflecting in a medium which refraction index is larger than in the other. On the contrary, if the medium has a smaller refraction index, we have:

$n_{substrate} > n_{film}$ => m=n-1/2 constructive interference (maxima)

$n_{film} > n_{substrate}$ => m=n-1/2 destructive interference (minima)

And we obtain the Bragg law for angular positions of the maxima and minima values in grazing incidence:

$$sin^2\theta = \left[\frac{(n-k)\lambda_x}{2d}\right]^2 + 2\delta$$

[11]

Where d is the thickness of the film, 1-d is the real part of the refraction index and k=0 corresponds to the minima in intensity, while k=1/2 is a maximum if the substrate has an electronic density smaller than the film.

2.2.1. SAXRD: Small angle X-ray diffraction in superlattices

In small angle XRD scans of superlattices two different interference patterns will appear. The first one is due to the total thickness of the superlattice, and it is sensitive to the averaged refraction index. The latter is due to the artificial modulation of the superlattice, which is responsible for the new maxima appeared in the angular positions given by the Bragg's law for grazing incidence in superlattices:

$$sin^2\theta = \left[\frac{n\lambda_x}{2d}\right]^2 + 2\delta$$

[12]

This equation is practically the same as in equation 11. The difference arises in the order of diffraction, which is always an integer in this case due to the fact that the interference pattern responsible for the superlattice maxima emerges from the interference of waves which are reflected at identical interfaces and, hence, the wave won't change the net value of the phase.

Fluctuations of the film or superlattice thicknesses result in a decrease and a broadening in the intensity of the peaks. This effect is more pronounced for high order reflections as can be seen in the example of Figure 3.

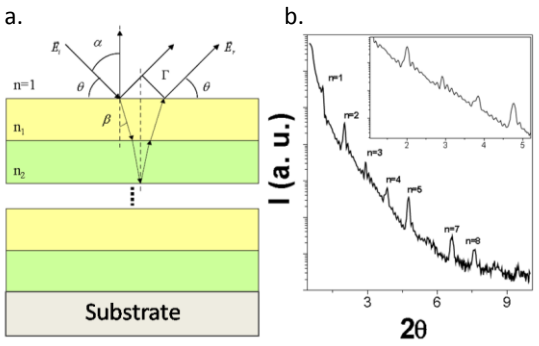

Figure 3. (a) Schematic showing the reflections which give rise to diffraction maxima. (b) Example of a grazing angle diffraction pattern from a superlattice.

3. Atomic Force Microscopy (AFM)

This technique is based on the interaction between a tip and the surface of a sample when both are separated a distance of a few Å. The AFM can control the force applied to the tip due to the small distance between the tip and the superficial atoms of the sample. The dependence with the distance is explained by the Lennard-Jones potential, which describes the interaction energy of two isolated atoms located a few Å away from each other. For very short distances (<10Å), this force experimented is repulsive due to the ionic contribution, which does not allow the contact between the particles. For larger distances (10-200 Å), the sign of the force changes due to the predominance of the attractive Van der Waals forces, which appear as a consequence of the polarization of the electronic clouds surrounding the atomic nucleus. In the regime when the repulsive forces are predominating we speak of a contact mode. In this case the vertical resolution will be substantially larger than in the attractive forces mode, reaching the atomic resolution in certain systems.

The interaction between the tip and the sample in an AFM will be given by the detection of a signal at the tip at the end of a cantilever. This way, the force which acts on the tip produces a deflection in the cantilever that will be quantified by a detector based on a laser diode. The diode will produce an electrical signal which will depend on the increase or decrease of the interaction force while maintaining constant the deflection in order to register the information of the surface. Besides this mode, the AFM can work in a dynamic mode. This mode gives rise to the oscillation of the tip at a frequency near the resonance frequency of the cantilever. The amplitude of the vibration will be reduced while the tip approaches the sample until the contact is produced. In this mode, the amplitude of the vibration will be used to register the surface.

AFM techniques have been used to study the surface of different samples in this study. All measurements have been performed at Centro de Microscopía Electrónica “Luis Bru” in Universidad Complutense de Madrid.

4. Scanning transmission electron microscopy (STEM)

A STEM is based on a transmission microscope equipped with a system of deflection coils which allow scanning the beam over the surface of the samples. The very first one was constructed by Manfred von Ardenne in 1937-1938 [6] and it had a spatial resolution of 40 nm in the scan direction. The focused electron beam goes through the sample, generating different signals which can be detected and monitored as a function of the position of the beam. Therefore, the STEM is a very versatile equipment, since it combines the high resolution of a conventional microscope with the capabilities of a scanning electron microscope regarding image formation and analysis (microanalysis, spectroscopy, etc.). Furthermore, thanks to success in the spherical aberration correction (Cs) in the past decade, the Ångström barrier in spatial resolution has been beaten [6-8].

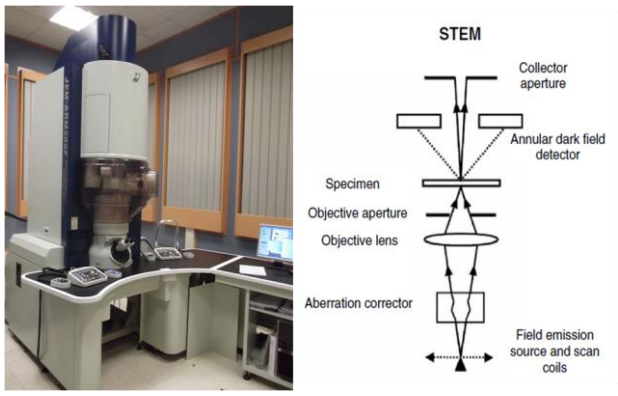

Figure 4. Left: Picture of the JEOL JEM-ARM200F of the Centro Nacional de Microscopía Electronica. Right: Schematic of the column of a scanning transmission electron microscope.

A STEM is different of a conventional TEM in the fact that most of the optical system acts on the beam before it reaches the sample (a schematic is shown in Figure 4). The electron trajectory is inverted and hence the position of the lenses. The beam is focused down to diameters in the 1 Å scale. Many STEMs, such as the ones used in this work, employ cold field emission guns (cFEG). These cFEGs have an overall better performance than thermionic sources, with higher brightness, smaller source size and lower energy spread.

For the operation of the tip in a field emission process, an ultra-high vacuum environment has to be reached in the gun in order to avoid the presence of contaminants. A high voltage (3-4 kV) is applied to the tip in order to extract the electrons beam. Afterwards a second voltage is applied (acceleration voltage) that accelerates the electrons to the desired energy and controls the effective source size and position producing a crossover. After the gun, the condenser lenses form a demagnified image of the source. To scan over the sample, a set of coils composed of fast deflectors produce a shift of the beam and then, bring the beam back to the parallel with the optic axis. The final step in the formation of the electron probe is done by the objective lens that produces the largest demagnification of the probe.

The spatial resolution in the microscope is determined by several factors. The first one is, in principle, determined by the energy of the electrons as determined by de Broglie equation [9]. However, the most important limitation in modern microscopes is introduced by the optical aberrations of the magnetic lenses that compose the microscope [10].

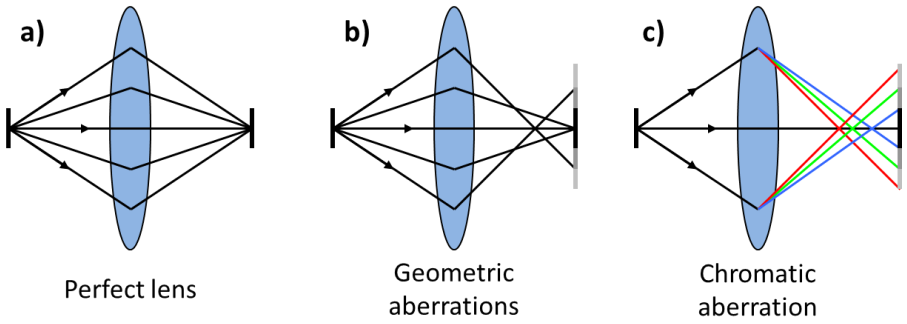

Figure 5. (a) Ray diagram for an ideal lens with no aberrations. (b) Diagram showing the effect of spherical aberration. (c) Diagram showing the effect of the chromatic aberration. Adapted from ref. [11]**.**

As in any optical lenses system, a perfect lens would converge all the rays coming from the same spot to a focused spot in the image plane. However, the presence of aberrations introduces limitations to this process. The diagrams in Figure 5 show how rays coming in at different angles, positions or energy will be focused with different strengths. Lens aberrations are classified in two categories: geometric aberrations due to errors in the optical path lengths and chromatic aberration due to a spread of the beam energy. The chromatic aberration (energy dependence) is treated separately because the energy dispersion is really small when using a cold FEG [12,13]. Assuming that the geometric aberration function depends only upon the angle of a particular ray with the optic axis, aberrations in the electron microscope can be expressed as a mathematical expression [12,15]:

$$\chi(\theta) = \frac{1}{2}C_1\theta^2 + \frac{1}{4}C_3\theta^4 + \frac{1}{6}C_5\theta^6 + \frac{1}{8}C_7\theta^8 + \cdots$$

[13]

This expression is a power series in function of the angle from the optic axis (θ), where the subscript N of each term indicates the order of the aberration. It reveals how rapidly the aberration increases off-axis. The lower order terms will predominate in the aberration function as θ is really small. This first order terms are the defocus and astigmatism, which can be corrected easily even in non-corrected electron microscopes. Spherical aberration, C_3 or C_S, expresses the angular dependence in the effect of the lens on the electron beam, rays propagating at different angles, are focused in different points. To reduce this aberration, an aperture is introduced to reduce the range of angles at which the rays reach the lens. However, the use of a small aperture involves the consideration of diffraction effects that could also limit the resolution. The optimum aperture allows one wavelength of third-order spherical aberration at its perimeter [15,16], and is given by:

$$\alpha_{opt} = \left(\frac{4\lambda}{C_S}\right)^{1/4}$$

[14]

These aberrations cannot be corrected with conventional magnetic lenses with rotational symmetry, as demonstrated Scherzer in 1936 [17] who also proposed how to overcome this limitation [15]. However, it wasn't until the late nineties, thanks to the advances in technology and computing power, that spherical aberration correctors were developed for the electron microscope. There were two different approaches, depending on the symmetry of the multipoles used: Haider et al. achieved the correction of aberrations in a TEM using a hexapole corrector in 1998 [18] and Krivanek et al. used a cuadropole/octupole geometry to correct the aberrations in a STEM in 1999 [12]. In both cases, the multipole magnetic lenses produce a magnetic field that changes with the distance to the optic axis, equal as the spherical aberration does, and hence, after measuring the aberration coefficients, the corrector produces a field that counteracts the aberration.

An example is shown in Figure 6, where the effect of the aberration correctors in the electron beam can be seen for the VG Microscopes HB603U dedicated STEM at Oak Ridge National Laboratory (ORNL). The full width at half maximum (FWHM) of the uncorrected beam was 0.12 nm, while after correction it decreases to FWHM = 0.05 nm, resulting in an improvement in both intensity and size of the electron probe. These improved beams allow better spatial resolution and even sensitivity to individual atoms [19], and further developments have been achieved in aberration corrector technology ever since. Now aberrations can be corrected up to the 5^{th} order [12] with resolutions under 0.5 Å at 300 kV [10,20]. Sub-Å resolution with single atom sensitivity has been also achieved at low voltages down to a few tens of kV [21-24].

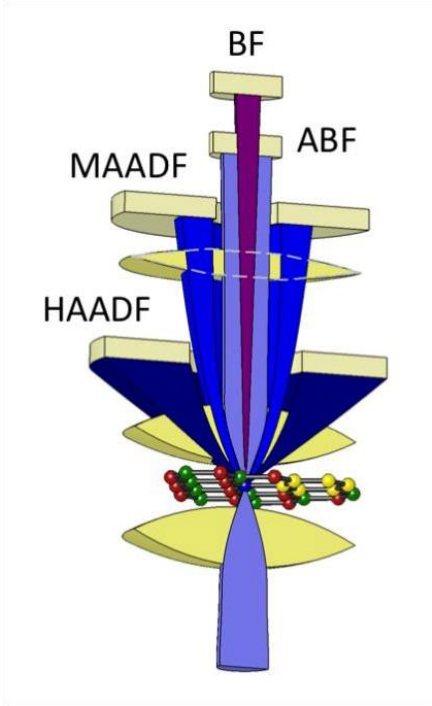

Figure 6. Schematic showing a few different possible imaging detectors in a scanning transmission electron microscope. Adapted from the Nion UltraSTEM User Manual.

The post-specimen optics consist of an objective lens that collects the electrons scattered at the sample and conduce them back parallel to the optic axis and the projector lenses. Together, these lenses make sure that the different signals enter the various detectors at the proper angles for any given detection mode as shown in Figure 6.

4.1. Imaging in STEM

The principal imaging and most commonly used modes in a STEM are the annular dark field (ADF) and bright field (BF) imaging [25]. The annular dark field images are usually referred as Z-contrast images [11, 12]. Depending on the detector angles, they can be medium angle MAADF (MAADF) or high angle ADF (HAADF) with a collection angular range from 100 to 200 mrad [28]. Both of them are used to detect electrons which are dispersed by the atomic cores (usually within 0.3 Å) which carry the information directly from the atomic number Z [25]. An incoherent image of the atomic distribution will be formed with this signal in a STEM, where the heaviest atoms will appear with higher brightness and the lighter ones will be darker [29]. The contrast is approximately proportional to Z^2, as dictated by Rutherford equation, which allows a very straightforward interpretation: it allows the study of the structural and chemical properties of a material with atomic resolution [19].

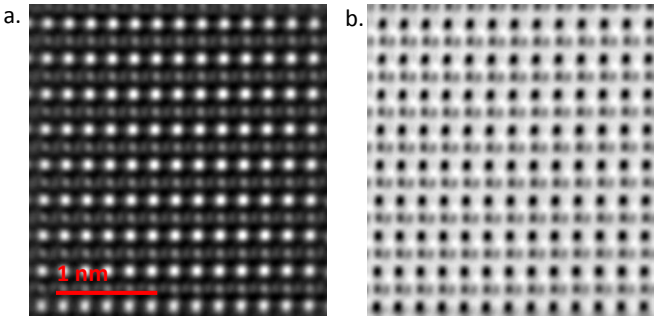

Figure 7. Simultaneously acquired HAADF (a) and annular BF (ABF) (b) images of $SrTiO_3$ down the (110) projection obtained with a JEOL JEMARM 200c operated at 200kV.

The latter most commonly used detector is the bright field (BF), in which the resultant image is formed by the direct-beam electrons, i.e. the "bright field disk" or illumination cone incident on the sample. The bright field is coherent, so the contrast depends on the relative phase of the scattered and unscattered electron waves. Thus, the BF images appear as dark spots sitting on a bright background. The image can change from dark to bright if the interference changes from destructive to constructive. Even though, the phase also varies with defocus, sample thickness or sample orientation, which make the interpretation of bright field images difficult in some cases.

The annular bright field (ABF) detector is an annular detector with an inner angle of 10 mrad and an outer angle of 20 mrad approximately. It has been recently introduced [30] and it is used in STEM mode to produce a contrast which, being similar to BF, is less sensitive to thickness or defocus changes [31]. This imaging mode is more sensitive to light atoms because atoms with higher Z goes to higher angles and hence the signal is not collected in the BF detector [32]. ABF is widely used to image light atoms such as oxygen and even hydrogen, as has been recently reported [33]. In Figure 7, an example of simultaneously acquired HAADF and ABF images of $SrTiO_3$ in the (100) orientation is shown. To obtain these images, a multiple-shot image sequence were taken and aligned by means of a cross-correlation process to remove noise [34].

4.2. Electron energy-loss spectroscopy

Besides the powerful technique of imaging in a STEM, other techniques have been used throughout this thesis to obtain information. Electron energy-loss spectrometry (EELS) relies on the analysis of the energy distribution of electrons that have gone through the specimen. Therefore, EELS gives us chemical and orbital information of our samples.

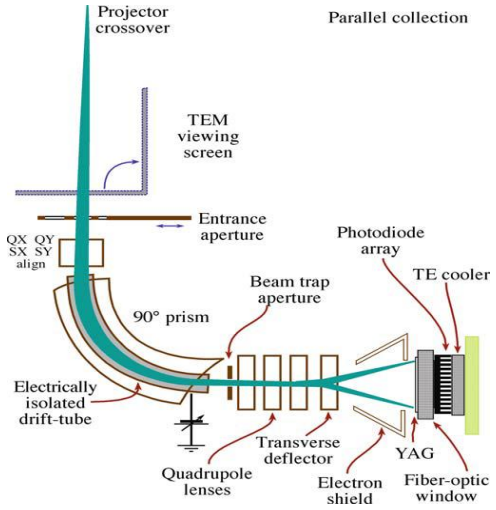

Figure 8. Schematic of an EEL spectrometer. Adapted from reference [9] .

When electrons are transmitted through the specimen, some of them are inelastically scattered, transferring part of their energy to the sample [35]. A number of different excitations may occur, including those of electrons in core levels that get excited to available higher energy orbitals. In this process the incident electron loses a given energy, which will be measured by the spectrometer. The EEL spectrometer consists of a magnetic prism that deflects electrons based on their energy. An illustration of this process is shown in Figure 8. An entrance aperture selects the electrons that will pass through a drift tube. In this tube, electrons are deflected by a magnetic field to angles that will depend of the energy loss. A set of magnetic lenses form the EEL spectrum in the dispersion plane, where a CCD camera or a photodiode is placed.

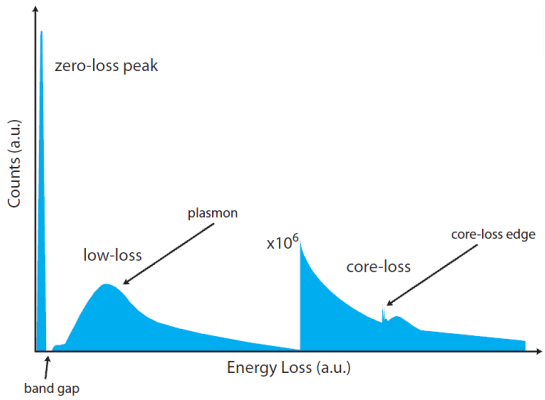

Figure 9. Schematic of an EEL spectrum. Adapted from reference [36].

The EEL spectrum can be classified in three main regions, as illustrated in Figure 9:

- Zero loss peak: It mostly gathers electrons that have been dispersed elastically. Two kind of electrons are collected, those which haven't lost energy and those which have excited phonons but have lost too little energy to be resolved by the spectrometer (typically < 1eV). The energy resolution will be indicated by the FWHM of this peak.
- Low loss region: In this region, we find the events corresponding to the lowest lying electronic transitions in the materials. In a semiconductor or an insulating material, the band-gap should be visible in this region [37-41]. We observe plasmon excitations produced by interaction between the electron beam and the sample. An estimation of the sample thickness can be done from the ratio between the zero-loss peak and the plasmon peaks integrated intensities. The interaction of the incident electrons with the outer shells of the atoms (e.g. valence band and intraband transitions) are visible in this region, as are inelastic scattering events for each element in the range of 5-50 eV.
- Core loss region: The signal produced is due to the interaction between the incident electrons with inner shells, which produces energy losses above 50 eV. In this interaction process, the electrons from the inner shells are excited into unoccupied states above the Fermi level. Thus, the edge energy onset corresponds to ionization thresholds, which are characteristic of core levels of a particular element, allowing the direct determination of the elements which compose the sample under study.

The EEL spectrum presents a background extended from the zero loss tail towards higher energies, which is created by plural scattering. The probability of electrons undergoing more than one scattering event increases with sample thickness and hence the intensity of the background signal. Therefore, specimens under study must be as thin as possible in order to reduce plural scattering and increase the signal-to-noise ratio (SNR).

4.2.1. The core-loss region

Within the core-loss region of the EEL spectrum, electrons from the inner shells are excited into unoccupied states above the Fermi level. Absorption edges which depend on the atomic number of the atom involved are observed. The EELS signal close to an edge is proportional to the local density of electronic states projected on the atom [35]. Thus, the analysis of this region in itself can give information on the local bonding, valence state, charge transfer, crystal field, etc. [26].

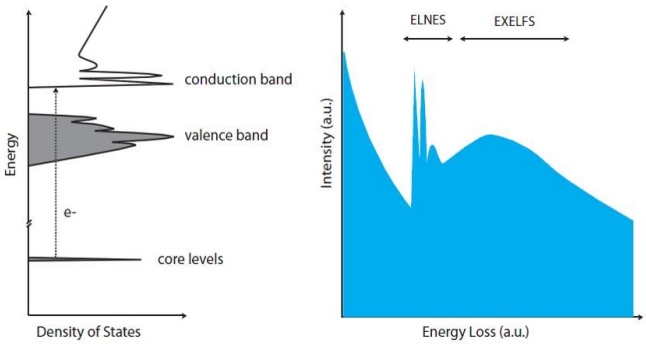

Figure 10. Schematic of the ionization edges fine structure demonstrating how EELS reflects the unoccupied density of states with electronic transitions from sharp core loss levels. Occupied states are indicated with gray shading in the density of states plot. Adapted from ref. [36].

In Figure 10 an example of the characteristic shape of these features is shown. The analysis of the fine structure provides information from the electronic structure of the specimen under study. The EEL spectra can be divided in two regions as displayed in the right scheme of Figure 10. The energy loss near-edge structure (ELNES) and extended energy loss-fine structure (EXELFS). The ELNES comprises the lowest energy features from the onset and reflects the unoccupied density of states, providing information about the local bonding environment (e.g. coordination and valence). On the other hand, the EXELFS exhibits modulations at higher energies which reflect the effects of ejected electrons with higher kinetic energies in the potential of the crystal.

4.2.2 Information of the data cube.

The EEL spectrometer produces different types of datasets. A single spectrum can be acquired while the beam is placed on a given position in the specimen, or on the contrary, it can be acquired while scanning over a region of interest (ROI). The set of data obtained is a 3D matrix or data cube, which contains an intensity value at each point (x,y,E) where x and y are the spatial coordinates and the E is the energy coordinate.

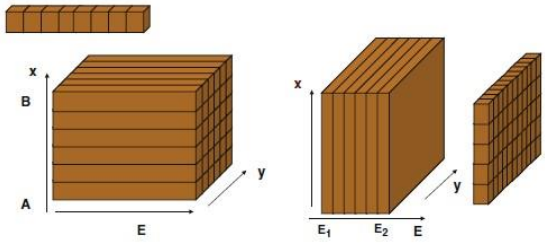

Figure 11. Schematic of the data cube. Left: The data cube in STEM SI mode. Right: The data cube in the EFTEM. Adapted from ref. [26].

Two different modes are used to measure spatially EEL spectra. The first one is displayed in the right scheme of Figure 11 and the technique is called Energy-filtered transmission electron microscopy spectrum image mode (EFTEM SI). In this technique the data cube is filled one image plane at a time. Other measurement method consists on scanning the probe over a region of interest (ROI), filling the data cube one spectrum at a time, thus acquiring an EEL spectrum for each pixel. This technique is called STEM spectrum image (SI) mode. Thereby a so-called spectrum image (SI) can be acquired [42,43]. This technique allows the mapping of the intensity of the spectroscopic features as a function on the position in the image, as well as their electronic properties with atomic resolution [44].

4.3. Advanced techniques for imaging and EELS in STEM

Throughout this work, some advanced data analysis techniques have been used for imaging and EEL spectra acquired with the STEM. A plug-in for Digital Micrograph (DM) has been used to analyze strain effects caused by the mismatch between the substrates and the films involved. This plug-in is called peak pairs analysis (PPA) and it is available from HREM Inc (Japan). For EELS data analysis, processing techniques as multivariate statistical analysis (MSA) are often used [45]. Through this work and we have employed principal component analysis (PCA) routines for Digital Micrograph written by Masashi Watanabe (Lehigh University) [46], mostly to remove random noise. For other purposes, as spatially resolved analysis of quantitative information, we have used advanced analysis techniques such as the compositional quantification routines available in in DM or multiple linear least square fits (MLLS) methods as needed.

4.3.1. Peak pairs analysis (PPA)

The PPA plug-in for Digital Micrograph has been used to study short and long range epitaxial strain effects, such as the ones produced by the different lattice parameters between two different materials or by structural defects [47,48]. This algorithm calculates the displacement field assuming a reference lattice in the real space, which is defined by the user. Special care must be taken at this step to select a non-distorted reference lattice in the image. The routine consists in, first, the location of the local intensity maxima, corresponding to the atomic column positions in the image (a filtered image will be used for this purpose to improve the resolution limit of the technique). Then, the user defines two basis vectors as reference for the strain calculations. For example, basis vectors can be the (001) and (100) directions, which are typical vectors

for strain analysis in the ABO_3 basic perovskite structure. After that, the algorithm identifies the pairs of peaks as the first neighbors of each peak maximum in the vector base defined previously. At this point, the displacements within the material are calculated using a non-distorted region as a reference for strain calculations. One of the most typical choices is the unit cell of the substrate for thin film analysis, or instead, a region in the thin film far away from the substrate so mismatch strain effects are already relaxed.

Resolving the following equations and using a 2D interpolation process, the strain tensor components are obtained at every point:

$$\left.\begin{array}{l} u_x = a_x\varepsilon_{xx} + a_y\varepsilon_{xy} \\ u_y = a_y\varepsilon_{yy} + a_x\varepsilon_{yx} \\ v_x = b_x\varepsilon_{xx} + b_y\varepsilon_{xy} \\ v_y = a_y\varepsilon_{yy} + b_x\varepsilon_{yx} \end{array}\right\} and \varepsilon_{xx} = \frac{\partial u}{\partial x}, \varepsilon_{xy} = \frac{\partial u}{\partial y}, \varepsilon_{yy} = \frac{\partial v}{\partial y}, \varepsilon_{yx} = \frac{\partial v}{\partial x}$$

[15]

Where (u_x, u_y) and (v_x, v_y) are the coordinates of the displacements with respect to the reference base vectors. The advantage of this method is that the strain around defects can be obtained without the user intervention and the local character of the analysis prevents the propagation of errors around the studied lattice.

4.3.2. Principal component analysis (PCA)

EELS can be used to extract information on the compositional and electronic properties of materials with atomic resolution, but the analysis of the spectral features is not always straightforward due noise in the signal. The principal component analysis (PCA) routines for Digital Micrograph written by Masashi Watanabe [46] are a very powerful way of applying MSA to SI datasets in order to remove white noise and also to identify spatially localized significant components. PCA reduces the dimensionality of a dataset to the minimum number of components that describe the original measurement without losing significant information [49]. The algorithm decomposes the EEL spectrum image data cube in a two dimensional matrix, in which the combination of the spatial coordinates are the columns of the data matrix and the spectral information is displayed in rows [45]. The spectral feature of each row is uncorrelated with the other rows and it is called an eigenspectrum. As the columns represent the other dimension, these are the amplitude of the eigenspectra in the matrix. Hence, a principal component is the individual product of each row and column. The magnitude of each eigenvalue corresponds to the amount of variance with which the corresponding principal component contributes to the dataset.

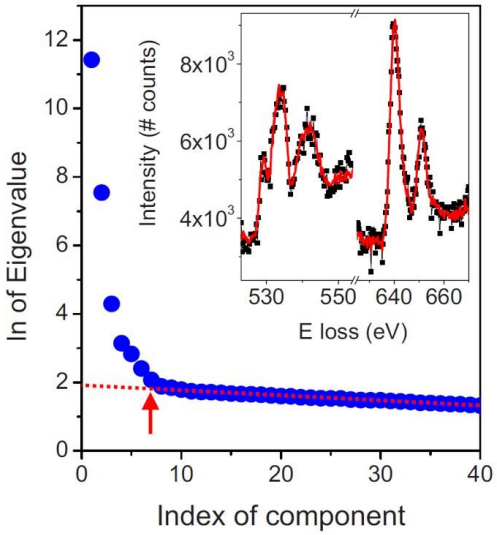

Figure 12. Scree plot representing the logarithm of the eigenvalues vs. the index of the principal component. A dotted red line highlights the portion of the plot where a flat behavior is observed (characteristic of uncorrelated noise). The red arrow points to the component index (n = 7) where the deviation from this flat behavior is observed. Inset: raw EEL spectrum showing an O *K* edge and a Mn $L_{2,3}$ edge (black dots). The red line is the same spectrum after PCA. Adapted from ref. [50].

The logarithms of the eigenvalues are plotted versus the component number in a Scree plot, as displayed in Figure 12. The principal components closer to the origin are dominant while those which contain random noise lie on a straight line at the end. Therefore, the original dataset can be reconstructed by selecting the dominant components and discarding the random noisy ones. The inset of Figure 12 shows a comparison between a raw spectrum (black points) and the noise reduced spectrum after applying PCA (red line). The high sensitivity of PCA and other multivariate analysis makes of them a very powerful tool, allowing the identification of various phases in the specimen displaying the different principal components of a SI [46]. However, experimental errors such as shifts in the energy, errors in the gain and dark current correction or energy misalignments must be addressed when applying PCA [51]. Special care must be taken also due its sensitivity to artifacts, which can be recognized as a component if these have a repetition in several spectra.

4.3.3. EELS compositional quantification

One of the most powerful capabilities of EELS can be found in the extraction of quantitative information about the chemical composition of a specimen. This way, non-stoichiometric areas in a sample or chemical segregation zones can be detected in the specimen under study. In a given spectrum, the area under an ionization edge, I_k, is proportional to the number of atoms of the chemical species per unit area [35]. Assuming that the electrons contributing to the edge have undergone a single ionization event, the probability, P_k, that a given incident electron will suffer a determined ionization event, k, can be expressed as:

$$P_k = N\sigma_k exp\left(\frac{t}{\lambda_k}\right)$$

[16]

Where N corresponds to the number of atoms per unit area, σ_k is the scattering cross section, t is the specimen thickness and λ_k is the mean free path for ionization losses. In this equation it is assumed that the spectrometer collects the complete angular range $(0 - 4\pi\ sr)$, which is not true. Therefore, the equation has to be modified. If we also assume that the specimen is very thin, the intensity above the background for a determined ionization edge(I_k) can be expressed as:

$$I_k(\Delta\beta) = N\sigma_k(\Delta\beta)I_T(\Delta\beta)$$

[17]

Where I_T is the total transmitted intensity, β is the collection angle, Δ is the integration window and $\sigma_k(\Delta\beta)$ is the partial ionization cross-section. If we have information about how large the investigated volume is and the cross-section of the element of interest, we can determine the absolute number of atoms of a given species. However, in practice, it is difficult to establish the exact thickness of the specimen and, hence, it is more convenient to obtain relative concentrations between different species. Thus, for a relative concentration ratio of two elements, the total transmitted intensity term drops out and the ratio can be written as:

$$\frac{N_A}{N_B} = \frac{I_k^A(\Delta\beta)\sigma_k^B(\Delta\beta)}{I_k^B(\Delta\beta)\sigma_k^A(\Delta\beta)}$$

[18]

4.3.4. Multiple linear least-square fit

The multiple linear least-square fit (MLLS) is a method based on the spatial-difference technique [52]. This analysis method is used to fit an experimental spectrum using two or more reference spectra [53,54]. So, the experimental EEL spectrum can be expressed as a linear combination of different components as follows:

$$F(E) = AE^{-r} + B_a S_a(E) + B_b S_b(E) + \ldots$$

[19]

Where AE^{-r} is the power-law background, B_a, B_b, etc are the scaling coefficients and $S_a(E)$, $S_b(E)$ ...are the reference spectra. The scaling coefficients obtained with this method give statistical weights associated with each reference spectra.

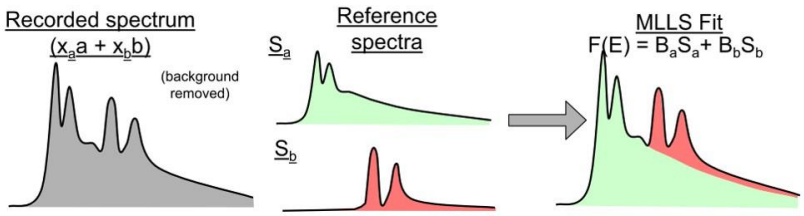

Figure 13. Illustration showing how the MLLS fit method can be used to separate overlapping edges. Adapted from the Gatan EELS Imaging and Analysis School materials.

Therefore, these coefficients are used to quantify changes in the fine structure, separate overlapping edges as shown in Figure 13, or even to produce better quality elemental maps with reduced noise (as an alternative to PCA). This method has been used mostly to obtain better quality elemental maps from SIs [55]. Usually, the background removal for core-loss edges is performed using a power law fitting [35], where the intensity of the background is given by $I = aE^{-r}$, where E is the energy loss and a and r are fitting constants. Using a MLLS fitting an improvement for mostly low energy edges can be achieved [56,57]. We use the estimated background and edge signal after background removal obtained with Digital Micrograph as our reference spectra as displayed in Figure 13. By means of this technique, the signal-to-noise ratio for elemental maps is improved because the background has to retain a constant shape for the whole spectrum image. However, to perform this type of analysis it is important to use data with very high signal-to-noise ratios and usually, random noise in the EEL spectrum images has been removed using principal-component analysis first [46].

Other uses of this method are, for example, the quantification of the oxidation states of *3d* metals as titanium. Taking into account a reference Ti $L_{2,3}$ edge spectra of a well characterized material, we can fit our experimental spectrum and obtain the statistical weight for the different valence states. An example is the use of reference titanium $L_{2,3}$ edges spectra for $LaTiO_3$ (Ti^{+3}) and $SrTiO_3$ (Ti^{+4}) from the work of J. Garcia-Barriocanal et al. [58] for the analysis of the oxidation state in a bombarded thin film of $SrTiO_3$ along the hole thickness of the sample [59].

4.3.5. Electron microscopes

A number of different aberration corrected microscopes have been used during this thesis: the JEOL JEM ARM200CF installed in the "ICTS Centro nacional de microscopía electronica" (CNME) at Universidad Complutense de Madrid (Spain), and also the Nion UltraSTEM100 and UltraSTEM200 both installed at the Oak Ridge National Laboratory, TN, U.S.A.

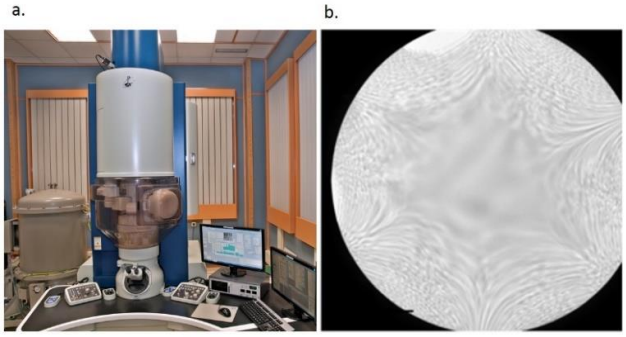

Figure 14. (a) Photograph of a JEOL JEM ARM200CF. (b) Image of a focused aberration corrected ronchigram over an amourphous specimen acquired in a JEOL JEM ARM200CF microscope at CNME.

The JEOL JEMARM 200CF electron microscope is equipped with a cFEG capable of working at 80, 100 and 200 KV acceleration voltages and a Gatan Quantum EEL spectrometer. It has a CEOS spherical aberration corrector in the condenser lens with a 6-fold symmetry, as shown in Figure 14b. This microscope is capable of working in both TEM and STEM modes and has the possibility of acquiring ABF images using a beam stopper with an outer radius of 10 mrad on top of the bright field detector.

An example of STEM imaging and EELS in the JEOL JEM ARM200CF is presented in Figure 15. The sample under study is a thermoelectric thin film of $Ca_3Co_4O_9$ grown on a YSZ buffer layer. The high resolution HAADF image given in Figure 15a show a high quality epitaxial growth of the $Ca_3Co_4O_9$ film. Some stacking faults are present which can be seen in the atomic resolution EELS chemical maps of Figure 15b. The microscope allows observing in detail the stacking faults, which consist of a double stacking of CoO_2 layers instead of the usual crystallographic sequence of alternating CoO_2 and Ca_2CoO_3 layers.

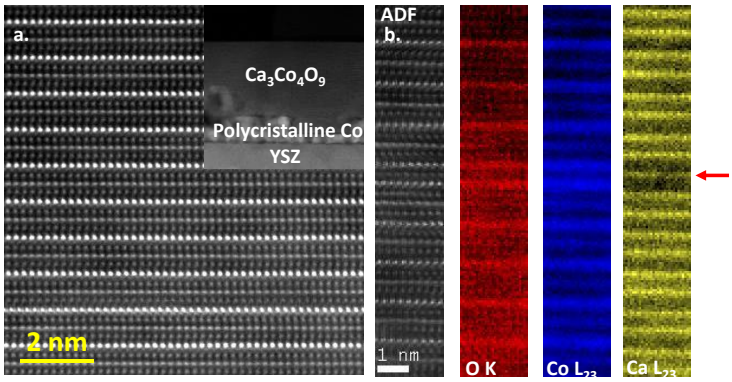

Figure 15. (a) High resolution HAADF image of a $Ca_3Co_4O_9$ thin film. Inset: Low magnification image of the sample. (b) Left: ADF image of a ROI where an EEL spectrum image was acquired. Right: atomic resolution EELS maps corresponding to the O K (red), Co $L_{2,3}$ (blue) and Ca $L_{2,3}$ (yellow) signals. The red arrow indicates a stacking fault (paper submitted)

These results are part of a study within a collaboration with A. Pérez Rivero and C. Prieto (CSIC). The growth of epitaxial thin films of the layered cobaltite $Ca_3Co_4O_9$ on cubic YSZ single crystals and its comparison with similar epitaxial films on hexagonal Al_2O_3(0001) has been studied. The thermoelectric characterization shows an enhanced Seebeck coefficient as well as a worsening of the electrical conductivity for YSZ-deposited films (paper submitted).

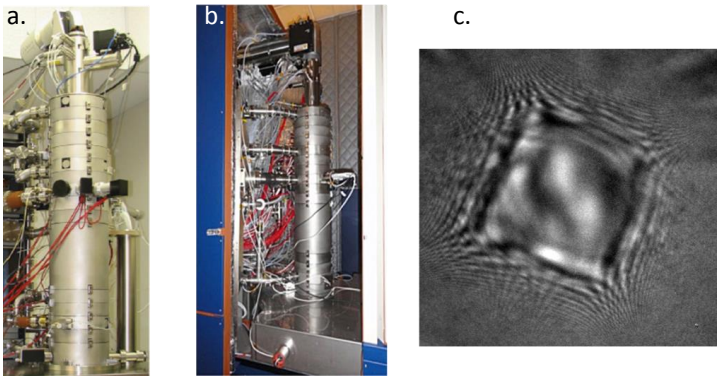

Figure 16. (a) Photograph of a Nion UltraSTEM 100. (b) Photograph of a Nion UltraSTEM 200. (c) Image of a focused aberration corrected ronchigram over an amorphous specimen acquired in a VG Microscopes HB603 STEM at ORNL.

The Nion UltraSTEM100 [60] uses a cFEG that can operate at 60 and 100 kV acceleration voltages and is equipped with a Gatan Enfina spectrometer. On the other hand, the Nion UltraSTEM200 is equipped with a cFEG that operates at 60, 100 and 200 kV and a Gatan Enfinium spectrometer. This microscope features also a dedicated ABF detector. Both of them are dedicated STEM microscopes equipped with Nion 5^{th} order aberration correctors using a cuadrupole/octupole geometry as shown by the 4-fold symmetry of the focused ronchigram image in Figure 16c.

5. Transport measurements

5.1. Closed-cycle Cryophysics helium

For low temperature resistance measurements in sections of multiferroic tunnel junctions of this work we used a closed-cycle Cryophysics helium refrigerator, which works with the expansion of highly-pure He-gas compressed in a Gifford McMahon cycle. The expansion through the capillaries undergoes two steps at 50 K and at 8.5 K. The sample is mounted onto a cooled copper piece in contact with the second cooling step. The system is evacuated by a rotary pump capable of a pressure down to 10 mTorr, measured with a Pirani vacuum sensor. The lowest temperature reached is 13 K. A silicon diode thermometer is in contact with the sample holder calibrated for measuring between 10 and 325 K. The system is also equipped with a heater controlled by a Lake Shore 330-11 temperature controller, which permits varying the sample's temperature between room temperature and 14 K with 10 mK accuracy. Micro-coaxial wires are used for low noise measurements. For magnetoresistance measurements we used an electromagnet (with a distance between magnetic cores of 10 cm), which can provide a magnetic field in the range of ± 4200Oe.

The resistance of thin films has been measured using the Van der Pauw four-point method [61] to eliminate any contribution given by the in-series contact resistance. Four electrical contacts were evaporated on the surface of the samples using silver and then connected to the low-noise wiring by indium or silver paint. In the case of tunnel junctions (current perpendicular to plane) electrical measurements have been done using 2-points method. The instruments used were a Keithley 2400 source meter, capable of apply voltage between 5μV and 210V and measure current from 10 pA to 1.055A.

5.2. Dielectric spectroscopy for ionic conductors

The classical measurements of resistance using dc current is not possible in ionic conductors for the special nature of the charge carriers. When a constant electrical field is applied in ionic conductors, the ions move towards the electrodes and accumulate since they cannot cross the electrodes to complete the circuit as electrons do. This effect is the so-called blocking effect of carriers and give rise to plateaus in the conductance measurements. Therefore, the electrical field inside the ionic conductor drops to zero in the limit of long times when a constant voltage is applied. To obtain the response in the frequency domain of ionic conductors an alternating current (ac) must be applied. Measuring the electrical response of materials in the frequency domain is called dielectric spectroscopy [62].

The principle of the measurement at one frequency is simple: a sinusoidal voltage is applied with and amplitude V_0 and frequency f and while the current intensity I is measured. If the sample is in the linear domain of response, the response of the sample can be considered as a sinusoidal current with amplitude I_0, the same frequency f and a phase difference of θ respect the initial voltage. The impedance of the sample at the frequency f is a complex number, whose modulus is the ratio between amplitudes and the angle is the difference between the applied voltage and the current measured.

To obtain an impedance spectrum the frequency must be changed in the desired range. The ionic conductors present negative phase displacements which correspond to a capacitive behavior. Thus the admittance Y, which is the inverse of impedance, is one of the most widely measured quantities. This magnitude is the conductivity of the sample except for a geometrical factor and it is mostly used for the analysis of transport in ionic conductors. The equivalence relation between the capacity and permittivity of the capacitor is given by the ratio A/d:

$$C = \frac{A}{d}\varepsilon\varepsilon_0, \qquad \sigma = \frac{d}{A}Y$$

[20]

Where C is the capacity, ε is the relative permittivity, ε_0 is the vacuum permittivity, σ is the conductivity, Y is the admittance, d is the thickness of the sample and A is the contact area [63].

The impedance spectroscopy equipment used in all the measurements is an AC Novocontrol BDS80 which allows to variate between 140 and 600 K using an inert N_2 flow.

6. Magnetic measurements for multiferroic tunnel junctions and bilayers

6.1. Vibrating sample magnetometer (VSM)

We performed magnetic measurements using a vibrating sample magnetometer (VSM). The VSM yields a direct and absolute measure of magnetization, since it measures the difference in magnetic induction between a region of space with and without the specimen. The magnetic moment of the sample is measured according to Faraday's law. The sample oscillates sinusoidally inside a small pick-up coil with a frequency of about 40Hz. The induced voltage due to $E = - d\varphi/dt$ is detected with the lock-in technique and converted to magnetic moment with an instrument specific calibration factor. It allows for the rapid measurement of M vs. T and M vs. H data with a useful sensitivity of approximately 10^{-6} emu. The sample is mounted on a diamagnetic stick fixed to a carbon rod. All the VSM measurements shown in this thesis were acquired in a Quantum Design physical properties measurement system (PPMS). The VSM measurements were carried out at the Mar García Hernández group by Roberto F. Luccas and Federico Monpean.

6.2. Ferromagnetic resonance

The ferromagnetic resonance (FMR) is a powerful technique to study the magnetic anisotropy of magnetic materials. Two main advantages are relevant of this technique. The first one is that this technique allows the exact determination of the anisotropy constants of a magnetic system (and the dependence with temperature). The second one is that is allows the study of the magnetic interactions between different magnetic materials in multilayered systems.

This technique consists in the absorption of microwaves due to the precessional motion of the magnetization M in a ferromagnetic sample around the effective magnetic field B_{eff} due the externally applied magnetic field $B_{appplied}$. The FMR is measured sweeping the applied magnetic field with a fixed microwave (typically on the order of tens of GHz).

7. References

[1] M. Varela, Z. Sefrioui, D. Arias, M. Navacerrada, M. Lucía, M. López de la Torre, C. León, G. Loos, F. Sánchez-Quesada, and J. Santamaría, "Intracell Changes in Epitaxially Strained YBa2Cu3O7-x Ultrathin Layers in $YBa_2Cu_3O_{7-x}$/$PrBa_2Cu_3O_7$ Superlattices," *Phys. Rev. Lett.* **83**, 3936–3939 (1999).

[2] N.W.Aschcroft and N.D. Mermin, Solid State Physics. Hong Kong (1987).

[3] A. Guinier, X ray diffraction in crystals, imperfect crystals, and amorphous bodies. Dpver publications, 1994.

[4] E. E. Fullerton and I. K. Schuller, "X-Ray Diffraction," *Phys. Rev. B* **45**, 9292–9310, 1992.

[5] D. M. Kelly, E. E. Fullerton, J. Santa-Maria, and I. K. Schuller, "A simple closed-form expression for the X-ray reflectivity from multilayers with cumulative roughness," *Scr. Metall. Mater.* **33**, 1603–1608 (1995).

[6] M. von Ardenne, "Das Elektronen-Rastermikroskop. Praktische Ausführung" *Z. Tech. Phys.* ***19****, 553–572* (1938).

[7] P. E. Batson, N. Dellby, and O. L. Krivanek, "Sub-ångstrom resolution using aberration corrected electron optics", *Nature* **418**, 617–620 (2002).

[8] P. D. Nellist, "Direct Sub-Angstrom Imaging of a Crystal Lattice", *Science* **305**, 1741–1741 (2004).

[9] D. B. Williams and C. B. Carter, *Transmission Electron Microscopy: A Textbook for Materials Science*, V1–V4 (2009).

[10] R. Erni, M. D. Rossell, C. Kisielowski, and U. Dahmen, "Atomic-resolution imaging with a sub-50-pm electron probe", *Phys. Rev. Lett.* **102**, 1–4 (2009).

[11] A. R. Lupini, S. N. Rashkeev, M. Varela, A. Y. Borisevich, M. P. Oxley, K. van Benthem, Y. Peng, N. de Jonge, G. M. Veith, S. T. Pantelides, M. F. Chisholm, and S. J. Pennycook, "Scanning Transmission Electron Microscopy" in *Nanocharacterisation*, J. Hutchison and K. Angus, Eds. Royal Society of Chemistry, 2007, pp. 28–65.

[12] O. L. Krivanek, N. Dellby, and A. R. Lupini, "Towards sub-Å electron beams", *Ultramicroscopy* **78**, 1–11 (1999).

[13] O. L. Krivanek, T. C. Lovejoy, N. Dellby, and R. W. Carpenter, "Monochromated STEM with a 30 meV-wide, atom-sized electron probe", *Reprod. Syst. Sex. Disord.*, **62**, 3–21 (2013).

[14] A. R. Lupini, "Aberration correction in STEM," University of Cambridge, 2001.

[15] O. Scherzer, "The Theoretical Resolution Limit of the Electron Microscope," *J. Appl. Phys.* **20**, 20 (1949).

[16] A. V. Crewe and D. B. Salzman, "On the optimum resolution for a corrected STEM", *Ultramicroscopy* ***9***, 373–377, (1982).

[17] O. Scherzer,"Über einige Fehler von Elektronenlinsen" *Zeitschrift für Phys.* **101**, 593–603 (1936).

[18] M. Haider, S. Uhlemann, E. Schwan, H. Rose, and B. Kabius, "Electron microscopy image enhanced" *Nature* **392**, 768–769 (1998).

[19]O. L. Krivanek, M. F. Chisholm, V. Nicolosi, T. J. Pennycook, G. J. Corbin, N. Dellby, M. F. Murfitt, C. S. Own, Z. S. Szilagyi, M. P. Oxley, S. T. Pantelides, and S. J. Pennycook, "Atom-by-atom structural and chemical analysis by annular dark-field electron microscopy" *Nature* **464**, 571–574 (2010).

[20]N. S. and Y. I. H. Sawada, N. Shimura, K. Satoh, E. Okunishi, F. Hosokawa, "Resolving 45 pm with 300 kV Aberration Corrected STEM" *Microsc. Microanal.* **20**, Supplementary 3, 124–125 (2014).

[21]D. a Muller, L. F. Kourkoutis, M. Murfitt, J. H. Song, H. Y. Hwang, J. Silcox, N. Dellby, and O. L. Krivanek, "Atomic-scale chemical imaging of composition and bonding by aberration-corrected microscopy" *Science* **319**, 1073–6 (2008).

[22]K. Y. Suenaga K, Sato Y, Liu Z, Kataura H, Okazaki T, Kimoto K, Sawada H, Sasaki T, Omoto K, Tomita T, Kaneyama T, "Visualizing and identifying single atoms using electron energy-loss spectroscopy with low accelerating voltage," *Nat. Chem.* **1**, 415 (2009).

[23]O. L. Krivanek, N. Dellby, M. F. Murfitt, M. F. Chisholm, T. J. Pennycook, K. Suenaga, and V. Nicolosi, "Gentle STEM: ADF imaging and EELS at low primary energies" *Ultramicroscopy* **110**, 935–945 (2010).

[24]T. O. K. Suenaga, Y. Iizumi, "K. Suenaga, Y. Iizumi, T. Okazaki, "Single atom spectroscopy with reduced delocalization effect using a 30 kV-STEM" *Eur. Phys. J. Appl. Phys.* **54**, 33508 (2011).

[25]A. R. Lupini, "Scanning transmission electron microscopy. In Nanocharacterization" H. J. L. Kirkland A.l., Ed. London: The Royal Society of Chemistry, 2007, pp. 28–65.

[26]Stephen J. Pennycook and Peter D. Nellist, *Scanning Transmission Electron Microscopy: Imaging and Analysis*. Springer, 2011.

[27]S. J. Pennycook, "Z-contrast stem for materials science" *Ultramicroscopy* **30**, 58–69 (1989).

[28]A. Howie, L. D. Marks, and S. J. Pennycook, "Ultramicroscopy," *PhD Propos.*, 8, 163–174 (1982).

[29]S. J. Pennycook, "Seeing the atoms more clearly: STEM imaging from the Crewe era to today," *Ultramicroscopy* **123**, 28–37 (2012).

[30]Y. I. and T. Y. Shunsuke Kobayashi1, Scott D. Findlay, Naoya Shibata, Teruyasu Mizoguchi, Yukio Sato, Eiji Okunishi, "Simultaneous visualization of oxygen vacancies and the accompanying cation shifts in a perovskite oxide by combining annular imaging techniques", *Appl. Phys. Lett.* **100**, 2012.

[31]Y. I. S.D. Findlay, N. Shibata, H. Sawada, E. Okunishi, Y. Kondo, "Dynamics of annular bright field imaging in scanning transmission electron microscopy", *Ultramicroscopy*, **110**, 903–923 (2010).

[32]N. S. S.D. Findlay, Y. Kohno, L.A. Cardamone, Y. Ikuhara, "Enhanced light element imaging in atomic resolution scanning transmission electron microscopy" *Ultramicroscopy* **136**, 31–41 (2014).

[33]E. Okunishi, I. Ishikawa, H. Sawada, F. Hosokawa, M. Hori, and Y. Kondo, "Visualization of light elements at ultrahigh resolution by STEM Annular Bright Field Microscopy" *Microsc. Microanal.* **17**, Supplementary 2, 164–165 (2009).

[34]R. Ishikawa, E. Okunishi, H. Sawada, Y. Kondo, F. Hosokawa, and & E. Abe, "Direct imaging of hydrogen-atom columns in a crystal by annular bright-field electron microscopy", *Nat. Mater.* **10**, 278–281 (2011).

[35]R. Egerton, *Electron Energy-Loss Spectroscopy in the Electron Microscope*. Springer 2011.

[36]T. J. Pennycook, "No Title," *Thesis*, p. Vanderbilt University.

[37]G. Brockt and H. Lakner, "Nanoscale EELS analysis of dielectric function and bandgap properties in GaN and related materials", *Micron*, **31**, 435–440 (2000).

[38]S. Schamm and G. Zanchi, S. Schamm, G. Zanchi, "Contamination and the quantitative exploitation of EELS low-loss experiments", *Ultramicroscopy* **88**, 211 (2001).

[39]S. Schamm and G. Zanchi, "Study of the dielectric properties near the band gap by VEELS: gap measurement in bulk materials", *Ultramicroscopy* **96**, 559–564 (2003).

[40]M. Stöger-Pollach, H. Franco, P. Schattschneider, S. Lazar, B. Schaffer, W. Grogger, and H. W. Zandbergen, "Čerenkov losses: A limit for bandgap determination and Kramers–Kronig analysis" *Micron* **37**, 396–402 (2006).

[41]M. Stöger-Pollach, "Optical properties and bandgaps from low loss EELS: Pitfalls and solutions", *Micron* **39**, 1092–1110 (2008).

[42]C. Jean Guillamume and C. Colliex, "Spectrum-image: the next step in eels digital acquisition and processing", *Ultramicroscopy* **28**, 252–257 (1989).

[43]J. A. Hunt and D. B. Williams, "Electron energy-loss spectrum-imaging" *Ultramicroscopy* **38**, 47–73 (1991).

[44]N. D. Browning, M. F. Chisholm, and S. J. Pennycook, "Atomic-resolution chemical analysis using a scanning transmission electron microscope", *Nature* **366**, 143–146 (1993).

[45]E. R. Malinowski, *Factor analysis in chemistry*, 3rd edition, vol. 16. New York: Wiley, 2002.

[46]M. Bosman, M. Watanabe, D. T. L. Alexander, and V. J. Keast, "Mapping chemical and bonding information using multivariate analysis of electron energy-loss spectrum images", *Ultramicroscopy* **106**, 1024–32 (2006).

[47]P. L. Galindo, S. Kret, A. M. Sanchez, J. Y. Laval, A. Yáñez, J. Pizarro, E. Guerrero, T. Ben, and S. I. Molina, "The Peak Pairs algorithm for strain mapping from HRTEM images" *Ultramicroscopy* **107,** 1186–1193 (2007).

[48]P. L. Galindo, "High Resolution Peak Measurement and Strain Mapping using Peak Pairs Analysis", *Microsc. Anal.* **23**, 23–25 (2009).

[49]I. . Jolliffe, *Principal Component Analysis*. Springer, 2002.

[50]M. Varela, M. Oxley, W. Luo, J. Tao, M. Watanabe, a. Lupini, S. Pantelides, and S. Pennycook, "Atomic-resolution imaging of oxidation states in manganites", *Phys. Rev. B* **78**, 1–14 (2009).

[51]S. Lichtert and J. Verbeeck, "Statistical consequences of applying a PCA noise filter on EELS spectrum images", *Ultramicroscopy* **125**, 35–42 (2013).

[52]P. R. Bevington and K. D. Robinson, "Data Reduction and Error Analysis for the Physical Sciences", *Recherche* **766**, 23–25 (2003).

[53]H. Shuman and A. P. Somlyo, "Electron energy l o s s analysis of near-trace-element concentrations of calcium," *Science* **21**, 23–32 (1987).

[54]R. D. Leapman and C. R. Swyt, "Separation of Overlapping Core E D G E S in Electron Energy Loss Spectra", *Ultramicroscopy* **26**, 393–404, (1988).

[55]P. Longo, P. J. Thomas, and R. D. Twesten, "Atomic-Level EELS Mapping Using High-Energy Edges in Dual-EELS TM Mode", *Micros.Today* **20**, 30–36 (2012).

[56]R. Door and D. Gängler, "Multiple least-squares fitting for quantitative electron energy-loss spectroscopy—an experimental investigation using standard specimens" *Ultramicroscopy* **58**, 197–210 (1995).

[57]K. Riegler and G. Kothleitner, "EELS detection limits revisited: Ruby - a case study", *Ultramicroscopy* **110**, 1004–1013 (2010).

[58]J. Garcia-Barriocanal, F. Y. Bruno, A. Rivera-Calzada, Z. Sefrioui, N. M. Nemes, M. Garcia-Hernández, J. Rubio-Zuazo, G. R. Castro, M. Varela, S. J. Pennycook, C. Leon, and J. Santamaria, "'Charge leakage' at $LaMnO_3/SrTiO_3$ interfaces" *Adv. Mater.* **22**, 627–632 (2010).

[59]B. M. Pabón, J. I. Beltrán, G. Sánchez-Santolino, I. Palacio, J. López-Sánchez, J. Rubio-Zuazo, J. M. Rojo, P. Ferrer, a. Mascaraque, M. C. Muñoz, M. Varela, G. R. Castro, and O. R. de la Fuente, "Formation of titanium monoxide (001) single-crystalline thin film induced by ion bombardment of titanium dioxide (110)", *Nat. Commun.* **6**, 6147 (2015).

[60]O. L. Krivanek, G. J. Corbin, N. Dellby, B. F. Elston, R. J. Keyse, M. F. Murfitt, C. S. Own, Z. S. Szilagyi, and J. W. Woodruff, "An electron microscope for the aberration-corrected era", *Ultramicroscopy* **108**, 179–195 (2008).

[61]L. J. van der Pauw, "A method of measuring the resistivity and Hall coefficient on lamellae of arbitrary shape", *Philips Tech. Rev.* **20**, 220–224 (1958).

[62]A. K. Jonscher, "Dielectric relaxation in solids", *J. Phys. D. Appl. Phys.*, **32**, R57–R70 (1999).

[63]F. Kremer and A. Schönhals, *Broadband Dielectric Spectroscopy*. Berlin Heidelberg, 2003.

Chapter 3: Effects of oxygen vacancies on the magnetic anisotropy of $La_{0.7}Sr_{0.3}MO_3/LaCoO_3/La_{0.7}Sr_{0.3}MO_3$ heterostructures.

In the search of novel functionalities driven by oxygen vacancies in ultrathin films and heterostructures, the $La_{1-x}Sr_xCoO_3$ (LSCO) system exhibits a very large potential. LSCO has a very wide spectrum of applications ranging from cathode in oxide fuel cells, ferroelectric memories, sensors or catalysis to spintronic devices [1,2]. Also, from the point of view of basic science, it constitutes an example of ferromagnetic metallic (FM) oxide with an additional degree of freedom: the spin state of Co atoms, which can give rise to unusual magnetic ground states even for finite Sr doping levels [3-5]. In fact, this family of materials has attracted much attention since the 1950's due to the spin-state transition phenomena reported in the $LaCoO_3$ (LCO) parent compound. These effects are due to the fact that the scales of the crystal-field splitting of the Co *d* states (E_{CF}) and the Hund's rule exchange energy (E_{EX}) are similar.

In the last decade, LCO epitaxial films under strain have been considered a model system for understanding the stabilization of novel ground states [6-8]. Bulk LCO does not exhibit any long-range magnetic order, coherently strained LCO films can be ferromagnetic (FM) at low temperatures [7,8]. This behavior is stabilized by the combination of epitaxial strain and the presence of arrays of O vacancies. LSCO thin films have also been shown to grow with a high density of oxygen vacancies [6,9-13], and the ordering of these defects can promote unexpected spin state superlattices. In general, the ability to control spin states via O vacancy engineering offers new avenues towards the tuning of magnetic properties. With this idea in mind, in this chapter, we set off to explore the possibilities of intercalating ultrathin cobaltite films in oxide devices and exploring new resulting from their magnetic properties. We will study the properties of magnetic tunnel junctions (MTJ's) where $La_{0.7}Sr_{0.3}MnO_3$ (LSMO) ferromagnetic electrodes are combined with O deficient LCO as the insulating barrier. To set the basis of our study, we will first present an in-depth STEM-EELS characterization of LSCO thin films with increasing amounts of O vacancies induced by low Sr doping levels, paying special attention to the development of O vacancy superstructures (it is well known that the introduction of Sr in the LSCO system provokes the appearance of such point defects). A section devoted to single, undoped LCO films will follow. Then, we will address the properties of cobaltite based MTJ's to find that the magnetic anisotropy of the system is strongly affected by the presence of O vacancies in the barrier. Based on the analysis of manganite/cobaltite bilayers, we will show that interfacing LSMO with ultrathin LCO layers drastically modifies the magnetic anisotropy of the manganite, making it independent of the substrate and closer to the magnetic isotropy proper of its rhombohedral structure.

1. $LaCoO_3$

The spin states of perovskite cobaltites are strongly influenced by the competition between the crystal-field splitting (Δ_{CF}) of the Co (*3d*) states into e_g and t_{2g} levels, and the Hund exchange. The first favors a low spin (LS) configuration while the second favors a high spin (HS) configuration as shown in Figure 1 [14][10].

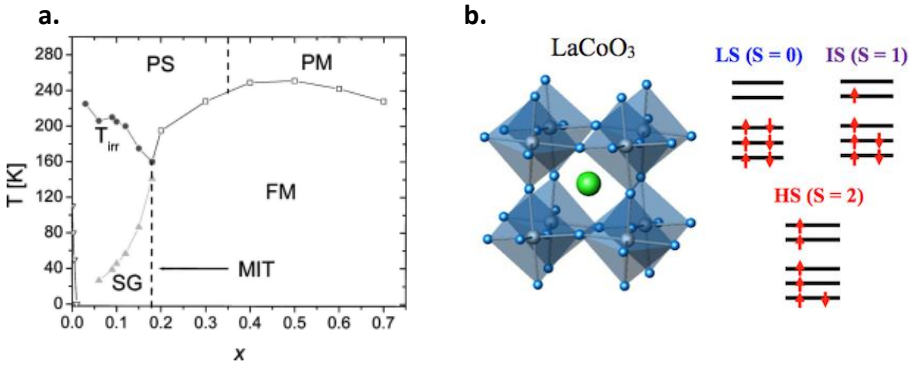

Figure 1. (a) Phase diagram of LCO, adapted from reference [14]. (b) Octahedral coordination of LCO along with a schematic of the *3d* levels showing the possible spin states. The lower energy levels correspond to the e_g states while the higher lying levels correspond to the t_{2g} states.

The gradual nonmagnetic to magnetic transition (upon increasing temperature) was first interpreted four decades ago as a gradual change in the population of high spin (HS, $t^4_{2g}\, e^2_g$, S=2) excited states, starting from a low-spin (LS, t^6_{2g}, S=0) ground state [15-21]. In 1996, a theoretical work by Korotin et al. proposed, on the basis of local density approximation + Hubbard U (LDA+U) band structure calculations, that the excited states exhibit an intermediate-spin (IS, $t^5_{2g}e^1_g$, S=1)-like character [22]. They reported three excited stable configurations, two of them of IS state with orbital ordering and the last one of HS nature. They explained the first transition from LS to IS near 90 K as a consequence of the thermal lattice expansion due an increase of the lattice parameter, while from the IS to the HS transition around 500K they proposed a gradual disorder of occupied e_g orbitals.

The dependence of the orbital overlap and crystal-field splitting on the Co-O distance ($r_{Co\text{-}O}$) and the Co-O-Co angle (θ) can be approximated by the expressions $W \propto r_{Co-O}^{-3.5}\sin(\theta/2)$ and $\Delta_{CF} \propto r_{Co-O}^{-5}$, where W is the overlap between the Co(*3d*) derived e_g and O(*2p*) orbitals [23,24]. Therefore, if either $r_{Co\text{-}O}$ or θ values are increased, Δ is reduced. A ferromagnetic order below 85 K can be explained in terms of the tetragonal distortion of LCO, which is critical for the appearance of magnetic moments. Extended x-ray absorption fine structure studies of LCO thin films on (La,Sr)(Al,Ta)O_3 (LSAT) have shown that the ferromagnetic order is due to a strain-induced suppression of the Jahn-Teller distortion that has been suggested (and also called into question) to occur in bulk LCO [25,27].

Under this scenario, some authors propose a novel-strain relaxation mechanism for LCO thin films that results in an ordered pattern of locally tetragonal and monoclinic distortions. These can promote the coexistence of LS-HS Co^{3+}, and introduce the possibility of a ferromagnetic interaction. Nevertheless, the origin of the ferromagnetic order in strained LCO is still under debate. Biskup et al. [12], proposed a complex relaxation mechanism of the epitaxial strain involving a superstructure including ordered stripe patterns of oxygen vacancies on tensile $SrTiO_3$(100) (STO) and compressive $LaAlO_3$(100) (LAO). They presented atomically resolved Z-contrast images of LCO thin films grown on a STO (100) substrates, along with simultaneously collected, atomically resolved EELS demonstrating unambiguously that there is a significant oxygen deficiency, which is responsible for the lattice relaxation and results in charge ordering (CO) within the Co sublattice. In

summary, epitaxial ultrathin LCO films exhibit unexpected magnetic properties associated with O deficiency, and we will use them as building blocks when designing novel oxide based devices. We will explore such possibilities and show how it is possible to use barrier properties to engineer the electrode performance via electronic or magnetic coupling.

2. STEM-EELS studies of LSCO thin films

In order to understand the nature and characteristics of O superstructures in the ultrathin colbaltite films for our heterostructures, a systematic study of LSCO thin films with low Sr contents has been carried out. Several samples have been grown on $SrTiO_3$ (STO) and $LaAlO_3$ (LAO) substrates in order to analyze the effects of both expansive and compressive epitaxial strain in the films. All the films were deposited by high pressure reactive DC sputtering. The systems under study are $La_{1-x}Sr_xCoO_3$ (LSCO) on STO(100) and LAO(100) substrates for x=0.05, 0.15 and 0.28 Sr-doping concentrations. LSCO grown on STO exhibits a 1.8% lattice mismatch, approximately, giving rise to tensile in-plane strain. On the other hand, LSCO on LAO exhibits a compressive lattice mismatch of 0.6 %.

Atomic resolution images for a series of LSCO thin films on LAO(100) are presented in Figure 2. Figures 2a, 2b and 2c display a set of HAADF images of LSCO with x = 0.05, 0.15 and 0.28 doping levels, respectively. Figure 2a indicates the zone axis for the three samples presented. The fast Fourier transform (FFT) of the images is shown on the right side. All the samples grow epitaxial and flat over long lateral distances. The interfaces are sharp and coherent, and no major defects or secondary phases are observed. For the x=0.05 doping, there is no evidence of the presence of Brownmillerite-like ordered arrays of oxygen deficient planes such as those reported in literature when other growth methods such as pulsed laser deposition (PLD) are employed. At this doping level the FFT indicates the expected cubic periodicity for the LCO bulk system. On occasion, CoO_2 planes exhibiting a contrast darker than the surroundings are observed, typical of local accumulations of O vacancies. However, no long range ordering is observed. Now, the Sr doping is increased (Figures 2b and 2c), a different contrast emerges. Dark stripes typical of CoO_{2-x} planes are observed more often (highlighted by red arrows). Red arrows also highlight the presence of bright spots which appear on the FFT patterns as a result of a doubling of the perovskite block. This modulation results from the extra periodicity introduced by the La-La elongated planes in the dark stripes. These stripes, which are well known for being associated with arrays of O vacancies lie within the in-plane direction (parallel to the interface). This result is not surprising. The presence of O deficient planes results in an enhancement of the average lattice parameter. In particular, in our case the measured dilation between adjacent the La-La columns across the dark planes is of ~4.4 Å, versus the ~3.6 Å measured between near La-La columns separated by a fully oxygenated (bright) CoO_2 plane. Since the LAO substrate induces a compressive strain in the film, the enlarged lattice distance (perpendicular to the dark planes) lies in the out-of-plane direction in order to release the compressive strain effect of the LAO(100) substrate [12]. These superstructures exhibit lateral domain sizes in the nanometric range. A high Sr doping level is needed to see clearly an ordered pattern of dark CoO_{2-x} planes every other unit cell (Brownmillerite-like, as reported for x=0.5 doping in literature) free of stacking faults and coherent over long lateral distances.

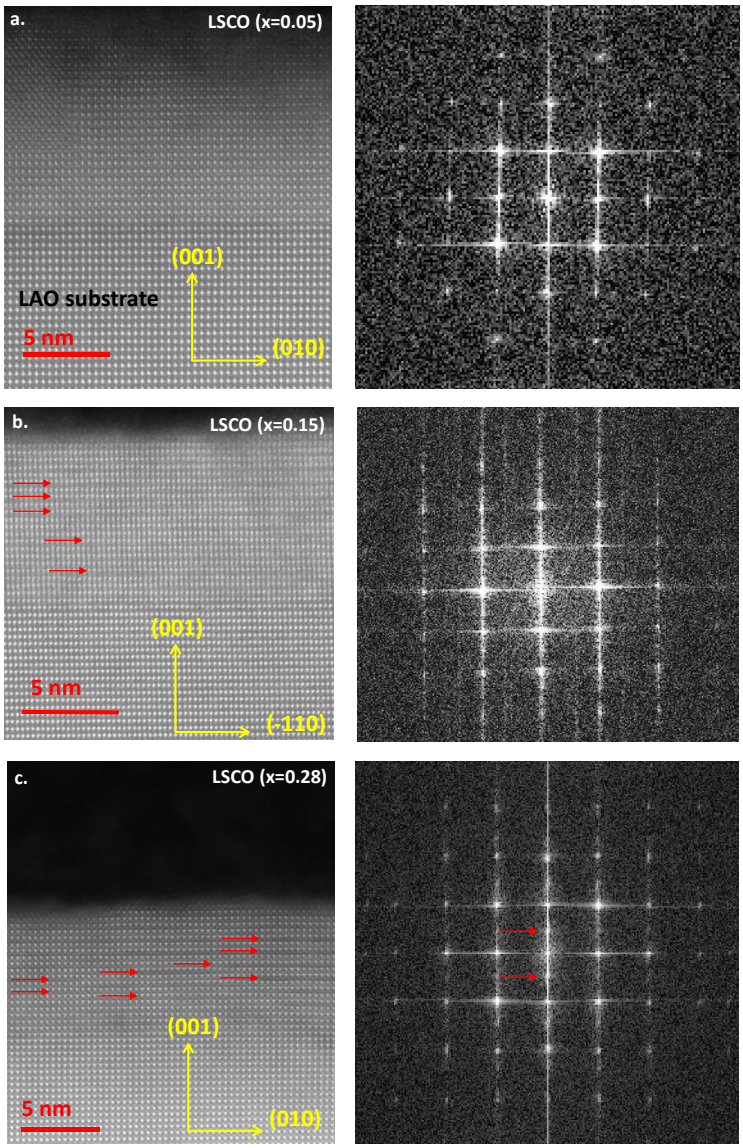

Figure 2. High angle annular dark field images of LSCO thin films grown on LAO(100) substrates with the corresponding FFT of the films for (a) x=0.05 (b) x=0.15 and (c) x=0.28 Sr doping levels.

A similar phenomenology occurs in LSCO thin films grown on tensile STO(100) substrates. Figures 3a, 3b and 3c show high resolution HAADF images of x = 0.05, 0.15 and 0.28 Sr-doped LSCO on STO(100), respectively. Again the red arrows on the FFTs highlight the superstructure spots associated with the doubling of the unit cell resulting from the presence of La-La dilated distances around CoO_{2-x} dark stripes in the real space images. This effect is again introduced by the ordering of O vacancies, giving rise to the extra periodicity. Since the mismatch strain in this case is tensile, the O deficient planes lie in the out-of-plane direction. Thus, the enlarged lattice parameter lies parallel to the interface plane, promoting accommodation of the tensile mismatch strain.

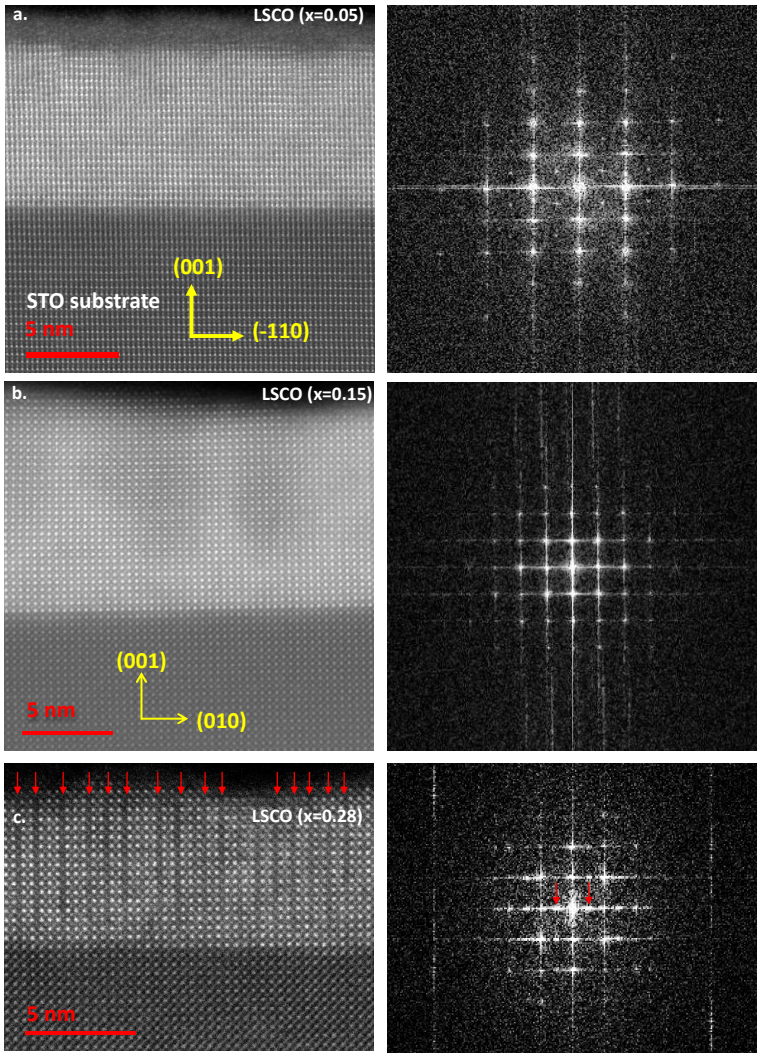

Figure 3. High angle annular dark field images of LSCO thin films grown on STO(100) substrates with the FFT of the films for (a) x=0.05 (b) x=0.15 and (c) x=0.28 doping levels.

Now we turn to study the electronic properties of these samples via the analysis of the fine structure of the EELS Co and O absorption edges. Transition metal $L_{2,3}$ edges result from excitations of *2p* electrons into empty bond states or the continuum. Therefore, these edges exhibit two white lines associated with transitions from the spin orbit split $2p^{3/2}$ and $2p^{1/2}$ levels to the available states in the 3*d* band. The expected value of the intensity ratio L_3/L_2 (also named L_{23} intensity ratio or L_{23} ratio) should be two, but it often differs from this value due to interactions between the 3*d* electrons, the core hole and the excited electron or the Coulomb exchange interactions between *p* and *d* electrons [28,29]. The L_{23} ratio increases with the number of electrons in the 3*d* bands across the periodic table when going from the $3d^0$ to $3d^5$ configurations, and decreases again when moving towards the high end of the 3*d* row. Also, for elements in the first half of the *3d* row the L_{23} ratio decreases as the oxidation number increases (opposite effects are found in the second half of the row) [29-32]. In this section we will obtain information about the L_{23} ratio for our Sr-doped cobaltite films in order to obtain an internal calibration for further experiments. We will analyze the fine structure of the O *K* edge, since it can also provide information on the Co oxidation state in our samples. This is because in the dipole approximation, the O *K* edge probes excitations of O 1*s* electrons into 2*p* bands, but those exhibit a pronounced *3d*-like character due to bonding effects. Hence, the O *K* near-edge fine structure also shows significant changes when the Co oxidation

state is modified. In particular, the pre-peak feature is related to the filling of the hybridized O *2p* and Co *3d* states (see peak 1 in Figure 4a). Aside from that, the main peak at 532 eV is attributed to the La *5d* band (see peak 2 in Figure 4a) and the feature at 548 eV contains information from the Co *4sp* bands (see peak 3 in Figure 4a) [33].

The fine structure of these edges has been analyzed before in order to obtain the average oxidation state of Mn in manganite oxides [34], providing three different ways to extract oxidation states of Mn.. These quantities are the normalized O *K* pre-peak intensity, the energy separation between the pre-peak and main peak (ΔE), and the ratio of the L_3 to L_2 white lines. They have also been successfully applied to cobaltites [35,36]. Here, the oxidation states of Co as function of the L_{23} ratio and ΔE obtained experimentally for strained thin films will be used as reference for the latter experiments with LCO heterostructures.

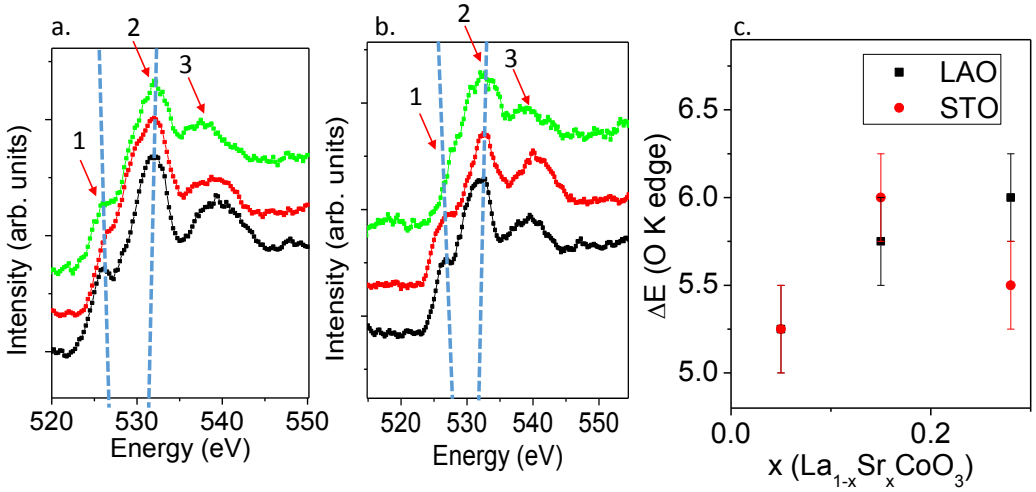

Figure 4. O *K* edge signals for LSCO films with x=0.05, 0.15 and 0.28 doping levels on (a) LAO and (b) STO substrates, from bottom to top, displaced vertically for clarity. The blue dashed lines indicate the position of the pre-peak feature and the principal peak of the edge, showing an increase of separation with higher doping levels. (c) Energy separation between the pre-peak and the principal peak vs. Sr content for LSCO films on LAO (black filled squares) and LAO (red filled circles).

Figures 4a and 4b display the O *K* edges for different Sr concentrations in LSCO thin films (0.05 in black, 0.15 in red and 0.28 in green) on LAO(100) and STO(100), respectively. The blue dashed lines go through the peaks 1 and 2 tagged in Figure 4a and show a shift in the relative pre-peak position compared to the main peak as the Sr content increases. The x=0.28 Sr-doped sample on STO shows no obvious pre-peak. This result suggests a noticeable deoxygenation of the sample, with a stoichiometry that deviates significantly from the nominal three O atoms per perovskite block. However, the Co oxidation state can still be analyzed via the difference in peak positions between the O *K* edge pre-peak and the adjacent main peak, the ΔE parameter. Figure 4c displays the ΔE of the O *K* edge is plotted versus the Sr content in LSCO thin films on STO(100) (red circles) and LAO(100) (black squares). For x=0.05 and x=0.15 the results are similar on both substrates, while there is a minor dispersion in the ΔE for x=0.28, which might be associated to local inhomogeneities in deoxygenation. Other methods can be used in the analysis of the Co oxidation states, as the L_{23} ratio in the Co $L_{2,3}$ edge.

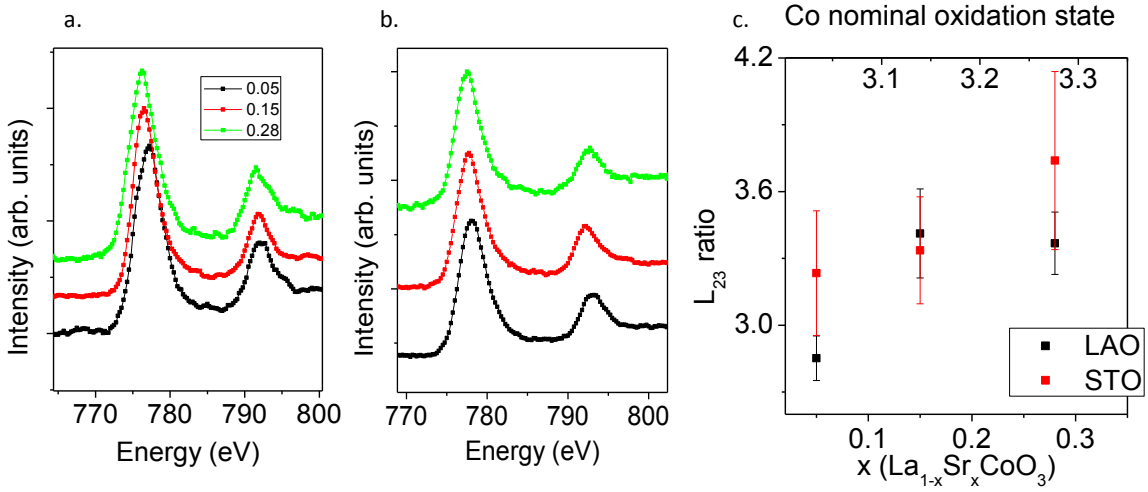

Figure 5. Co $L_{2,3}$ edge signals for LSCO films with x=0.05, 0.15 and 0.28 doping levels on (a) LAO and (b) STO substrates. (c) L_{23} ratio of the Co edge vs. Sr content and Co nominal oxidation states for 15 nm thin films of LSCO with different Sr content on STO(100) substrates (black squares) and LAO(100) substrates (red squares circles).

Figure 5 displays a set of Co $L_{2,3}$ edges measured on our samples both on LAO (a) and STO (b). To obtain these curves, an average of three spectra have been used for each Sr concentration avoiding the interfacial and surface signals.The L_{23} ratio values are plotted in Figure 5c versus the Sr doping and the nominal Co oxidation state for our series. The error bars are given by the mean square standard deviation. Some values are different for both substrates and have a large error bar, which would be consistent again with an inhomogeneous deoxygenation of the samples, but a general increasing trend is clear within error bars.

In summary, it is clear that Sr doping results in the introduction of O vacancies in our films, which can alter their structure and electronic properties. The lowest end of our analysis, LSCO with x=0.05, did not exhibit the well known O vacancy superstructure, but hints of small amounts of disordered O vacancies are detected. This finding points out that small amounts of O vacancies are present in general in cobaltite films, including low Sr doping levels. In the following, we will focus on the study of undoped LCO films. We will keep in mind that the presence of O defects is likely, and thus we will try to analyze the possible effects of their presence as appropriate.

3. LCO thin films for MFTJ's

Next we will analyze sinlge, undoped LCO films, since we will later use LCO as the insulating barrier in MFTJ's. LCO thin films have been grown on STO(001) substrates by an AC sputtering system at 750°C followed by an in-situ annealing at 900 mbar and 700°C. Reflectivity and X-ray diffraction measurements have been used primarily to calculate the thickness of the thin films and analyze the epitaxy of the samples.

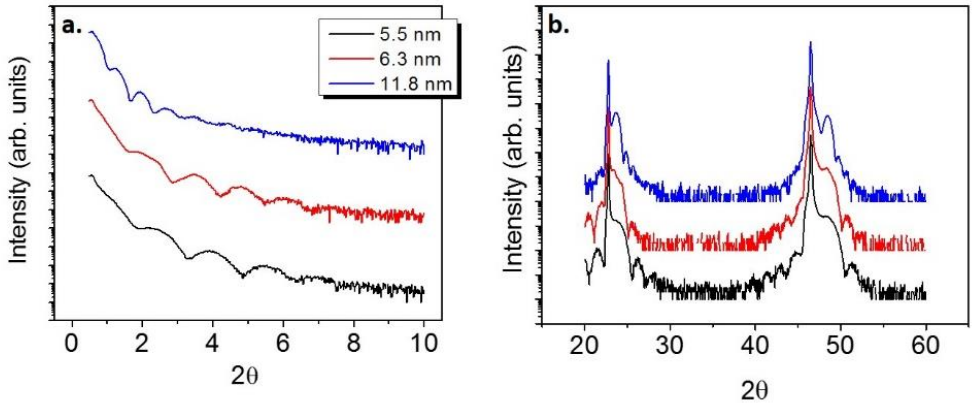

Figure 6. (a) XRR of several LCO ultrathin films grown of STO, displaced vertically for clarity. (b) XRD of the same set of thin films. The main peaks correspond to the STO(100) substrate peak while the others correspond to the *c*-axes of LCO.

Figure 6 displays a set of XRR and XRD patterns for LCO thin films grown on STO(100) substrates. The oscillations in XRR appear up to high angles (2θ=8º), which is an indicative of a high structural quality and flat surfaces. Oscillations are slightly damped for higher thickness values (e.g. 11.8 nm – blue curves). This result can be due to partial relaxation processes that may appear upon reaching a critical thickness value, but it does not constitute an issue for our experiment since the barriers of our MTJ's will stay within thickness ranges of approximately 3-4 nm in order to stay in a tunneling conduction regime. Figure 6b shows the XRD patterns of the same samples. A good epitaxy is inferred from the presence of finite size peaks around the substrate peaks. Our LCO films grow highly strained. The STO is an in-plane tensile substrate, which would tend to compress the *c* axis of the LCO. Bulk LCO exhibits a value of the *c* axis of 3.81 Å. Taking into account that the position of the LCO peak in the XRD patterns is at 2ϑ=48.45º, we calculate the *c* axis to have an average value of 3.7 Å. Hence, the compressive strain can be estimated to be around 2.8%.

LCO films exhibit a high structural quality, but to be a successful candidate as a barrier, they should be insulating as well. In order to evaluate the transport properties, two different kinds of measurements have been carried out. In-plane resistance vs. temperature measurements have been acquired using the Van der Pauw method to avoid in-series contributions of the contacts resistance [37]. On the other hand, impedance spectroscopy techniques (see chapter 2) have been employed to study possible conduction mecahnisms involving diffusion of oxygen vacancies.

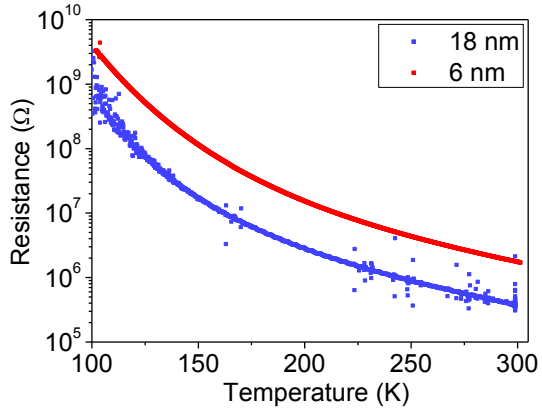

Figure 7. Resistance vs. temperature of a 18 nm (in blue) and a 6 nm LCO thin film (red) on STO(100). Low temperatures are noisy due the high values of the resistance.

Figure 7 shows a resistance vs. temperature curve for both a 18 and a 6 nm thick LCO thin films on STO(100). Both samples are insulating for the whole temperature range measured, so measurements of ionic conductivity have been carried out using impedance spectroscopy. Ionic conduction in these compounds takes place basically via diffusion of O vacancies. The possibility of having ionic paths in epitaxially strained rich patterned structures could result in higher values of the ionic conductivity or a reduction of the activation energy. Y. Yang *et al.* reported theoretically that the accommodation of a large amount of strain in perovskite-structure oxides give rise to octahedral tilts and oxygen vacancy ordering since the O atoms are tied to cations in octahedral formations [38]. Also, V. V. Metha *et al.* have reported that ordered oxygen vacancies contribute to the stability of structures under epitaxial strain in thin films grown on STO, LAO and (La,Sr)(Al,Ta)O_3 (LSAT) [39]. DFT calculations reported by Jeong Woo Han and Bilge Yildiz demonstrated that the planar tensile strain reduces the migration barrier of oxygen vacancy anisotropically on the LCO(001) surface, inducing an enhanced mobility along the [1-10] direction and a suppressed mobility along the [110] direction [40]. For these reasons, it is essential to study the ionic conductivity of our LCO thin films.

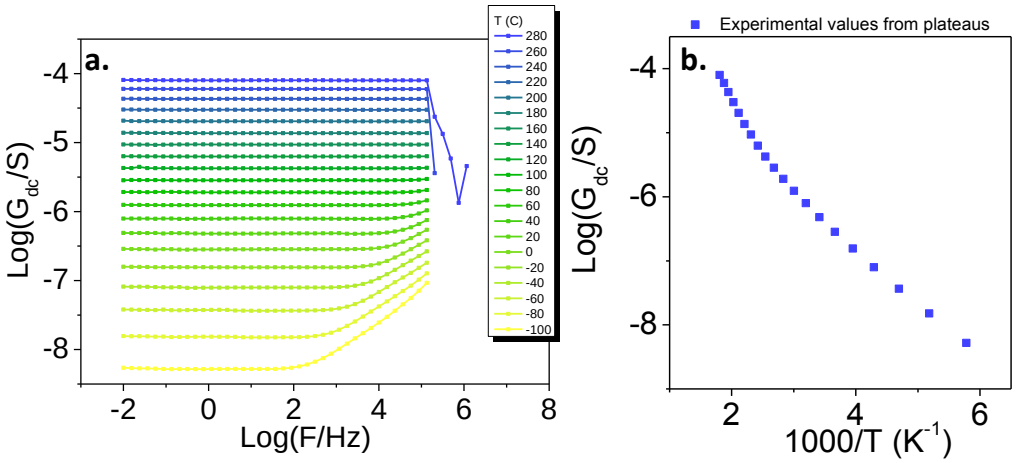

Figure 8. (a) Logarithm of conductance vs. logarithm of frequency of a 11 nm thick LCO thin film on STO(100) for several temperatures. (b) Arrhenius plot of the same sample. Blue filled squares represent the dc conductance values for each temperature in (a)

Figure 8 displays the dielectric response of a 11 nm LCO thin film on STO(100). Figure 8a shows the conductance vs. frequency for several temperatures. This conductance is independent of the frequency for almost all temperatures, which indicates that there are no blocking effects and the conduction process is purely electronic. Figure 8b displays the corresponding Arrhenius plot of the sample, which presents two different behaviors for high and low temperatures. The values of the activation energies are around E_A = 0.2 eV, typical for electronic conduction mechanisms. In view of these data, we can discard the possibility of a major ionic conductivity in our LCO thin films.

Magnetic hysteresis loops were also measured in order to study the magnetic properties of the LCO thin films. The magnetic field was applied parallel to the edge of the samples, and thus to the [100] or [010] crystal axes of the cubic STO substrate. Consequently, the magnetic field in these directions also coincides with the pseudocubic crystal axes of the cobaltite. The field was swept at 50 Oe/s for field values between 10000 and -10000 Oe. The typical saturation magnetization is 1-2x10^{-5} emu, whereas the noise floor of the VSM is in the range of a few times 10^{-7} emu. The results are presented in Figure 9, which shows a magnetization vs. magnetic field curve for a 18 nm thick LCO film on STO(100). The shape exhibits a pronounced round shape and a very large saturation field of ~0.3 T, which seem to behave like a superparamagnetic.

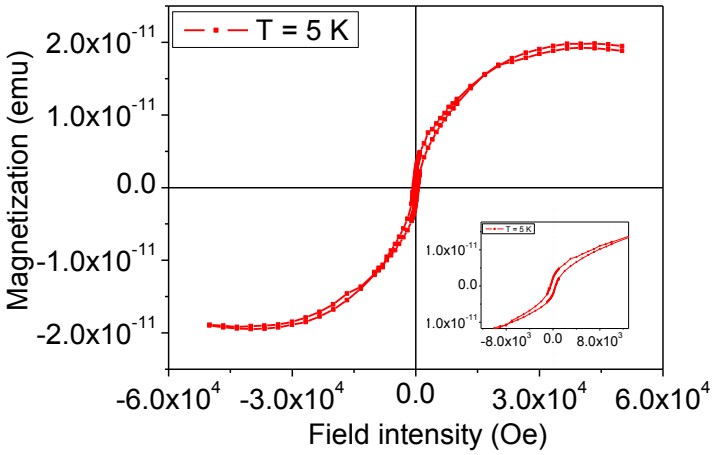

Figure 9. Magnetization as a function of magnetic field applied along the [100] of a LCO thin film of 18nm on STO(001). Inset: Zoom into the low field regime.

3. LSMO/LCO/LSMO heterostructures for magnetic tunnel junctions

Next, we move to the study of magnetic tunnel junctions (i.e., actual devices) combining ferromagnetic $La_{0.7}Sr_{0.3}MnO_3$ (LSMO) electrodes with LCO. LSMO exhibits a rhombohedral perovskite structure above and below T_C, with lattice parameters a = 3.876 Å and α = 90.46º at room temperature [41]. However, when LSMO is grown on a cubic substrate the unit cell is distorted in order to adopt a pseudocubic structure. As a result, the ratio between the in-plane (*a*) and out-of-plane (*c*) lattice parameters varies, being this parameter related to the magnetic properties of the manganite. As an example, Figure 10 depicts the effect of epitaxial strain (*c/a* ratio) on the orbital order of LSMO thin-films for different Sr compositions. In this orbital phase diagram the F region (orbital-disordered) is ferromagnetic and metallic, while the C ($3z^2$-r^2 ordered) and A regions (x^2-y^2 ordered) are insulating [42,43].

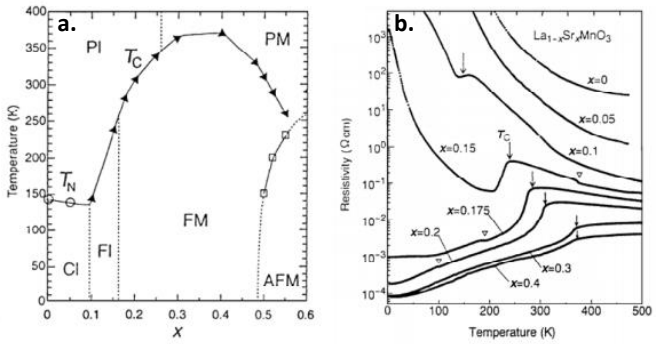

Figure 10. a) Phase diagram of $La_{1-x}Sr_xMnO_3$ adapted from references [44] and [45]. The AFM phase at large x is an A-type AF metal with uniform orbital order. PM, PI, FM, FI, and CI denote paramagnetic metal, paramagnetic insulator, FM metal, FM insulator, and spin-canted insulator states, respectively. T_C is the Curie temperature and T_N is the Neel temperature. (b) Temperature dependence of resistivity for various single crystals of $La_{1-x}Sr_xMnO_3$. Arrows indicate the Curie temperature. The open triangles indicate anomalies due to structural transitions.

For x=0.3 Sr doping, our case, bulk LSMO has a Curie temperature of 369 K and a saturation magnetization of Ms=3.7 μ_B/at_{Mn} at low temperatures. Also important for our experiment is the value of the resistivity at low temperatures, which turns out to be around 10^{-5} Ω cm. Another important property of LSMO is that it is a half-metallic ferromagnet as demonstrated by spin-resolved photoemission experiments. The half-metallic character of LSMO implies an empty minority spin conduction band. Thus, the material has 100% spin polarization at low temperature.

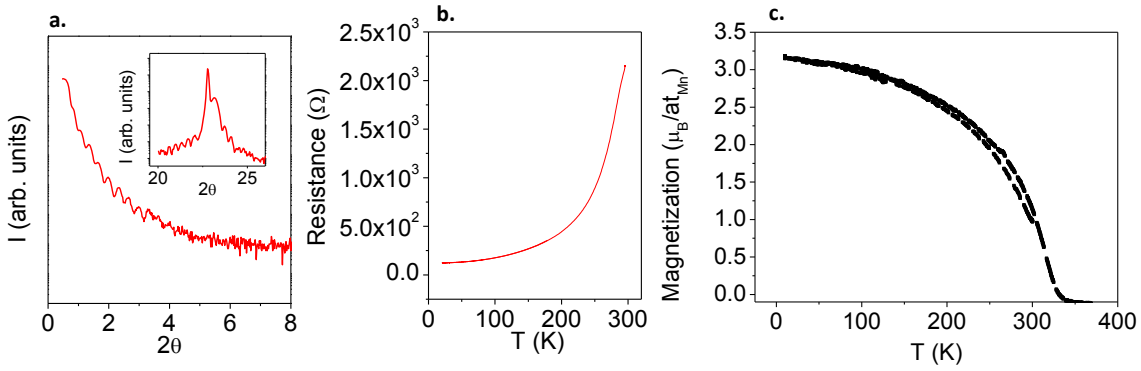

Figure 11. (a) X-ray reflectivity of a 30nm LSMO thin film grown on STO(100). Inset: X-ray diffraction pattern. (b) Resistance vs. temperature, again for a 30 nm thick LCMO film. (c) Magnetization vs. temperature of the same sample.

WE can obtain high quality LSMO films with optimal properties. Figure 11a shows the reflectivity of a 30 nm thick LSMO film on STO(100). Finite size oscillations run up to high angles, revealing a high degree of surface flatness. In the inset, the X-ray diffraction pattern of the same sample denotes good epitaxy and high quality of the film, since it also presents finite size peaks around the substrate reflection. In Figure 11b, the resistance vs. temperature curve shows a good metallicity as well. Finally, Figure 11c displays a typical value of the saturation magnetization for thin films, which reaches values near 3,2 μ_B/at_{Mn} at low temperatures.

So far, we have demonstrated the ability to grow high quality LSMO samples. Now, in order to study the properties of the MTJ's based on LSMO/LCO/LSMO heterostructures, we have also carried out both structural and magnetic characterization of LSMO/LCO/LSMO trilayers on STO(100) substrates, which we will show next. After that, we will address the fabrication of devices using lithography and ion milling techniques to measure the out-of-plane transport properties of the MFTs.

4.1. Magnetic tunnel junctions (MTJs) of LSMO/LCO/LSMO

To ensure good structural properties of these trilayers we have carried out both macroscopically averaged diffraction and local electron microscopy measurements. X-ray reflectivity and X-ray diffraction pattern of two trilayers of LSMO/LCO/LSMO on STO(100) substrates are presented in Figure 12a and 12b respectively. The samples shown are two different $LSMO_{15nm}/LCO_{3nm}/LSMO_{8nm}$ trilayers grown on STO(100) in two different positions inside the sputtering chamber to ensure homogeneity during the growth process, which could be critical wen producing devices at a later stage. The LSMO and LCO grow at different temperatures (900°C for LSMO and 750°C for LCO).

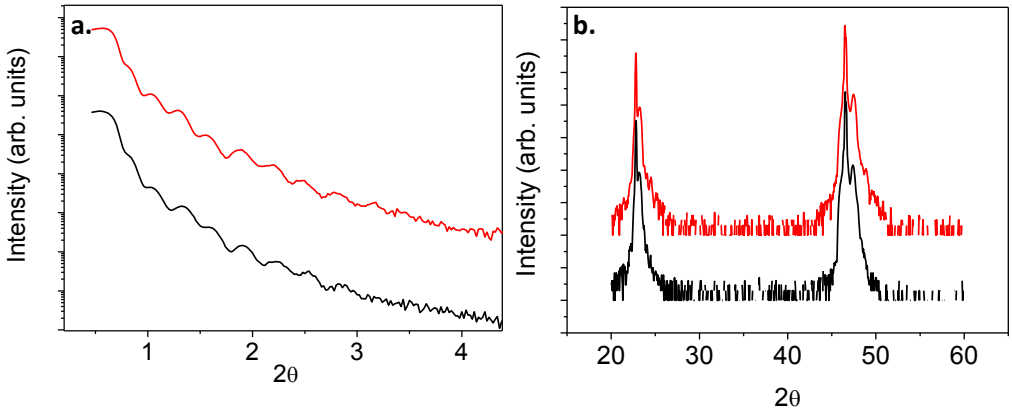

Figure 12. (a) XRR of two trilayers of LSMO/LCO/LSMO grown on STO(100) with the same thicknesses. Samples are grown in the same conditions but in different positions on the sputtering chamber. (b) XRD pattern of the same samples.

In order to define the MFTJs, the heterostructures have been patterned into micron size rectangle shaped pillars (9x18 μm^2 and 5x10 μm^2) using standard UV optical lithography and ion milling. Silver electrodes were evaporated to measure perpendicular transport. Figure 13 shows the schematic of such a junction for clarity.

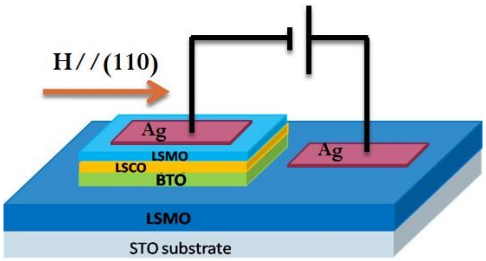

Figure 13. Schematic of the pillars defined for transport measurements.

Magnetic fields were applied along the easy axis of the LSMO ([110] direction) and swept between -4000 and 4000 Oe. Figure 14a shows the out-of-plane resistance vs. temperature of a MTJ of 5x10μm^2 $LSMO_{15nm}/LCO_{3nm}/LSMO_{8nm}$ on STO(100). The resistance values are very low compared to those expected, probably due to the small thickness of the LCO layer.

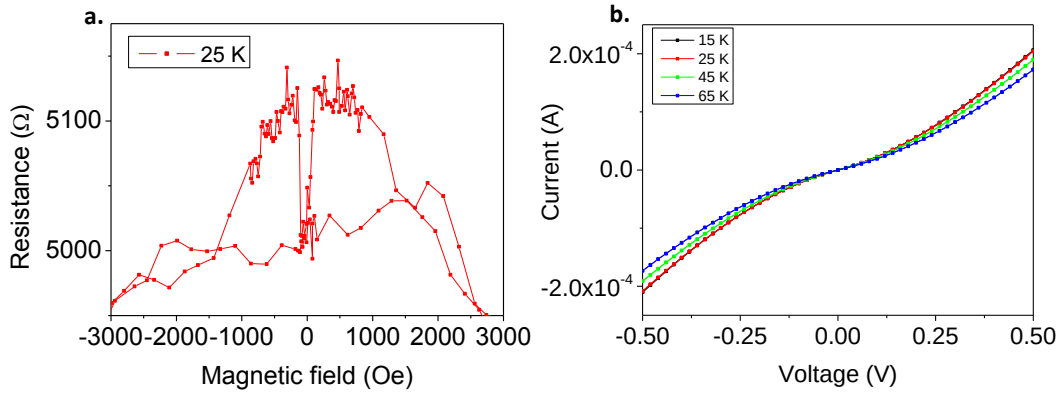

Figure 14. (a) Out of plane resistance vs. magnetic field of a MTJ of 5x10μm^2 consisting on a $LSMO_{15nm}/LCO_{3nm}/ LSMO_{8nm}$ trilayer grown on STO(100). (b) Intensity vs. voltage curves of the same sample measured for different temperatures.

The tunneling magnetoresistance (TMR) values obtained for these MTJ's are small, with maximum values of 3 % in the best junctions at low temperatures. We believe these low values are related to the magnetic properties of the electrodes, especially the coercive fields. The coercive field of the bottom layer for T=25 K is $H_{C\ bottom}$= 40 Oe as expected for this LSMO thickness, but the one associated with the top electrode is not clear from our data. The magnetic moments of the top electrode rotate gradually as the magnetic field is applied along a hard axis reaching a value of approximately 1600 Oe. This result is in good agreement with the magnetic behavior of bilayers, where LSMO layers grown on LCO do not saturate even for high values of the magnetic field (see the next sections). Figure 14b displays a typical IV curve, which shows the features typical of a tunnel conduction mechanism. Table II shows the values of the height of the barrier, φ, and the thickness, *t*, obtained by fitting these IV curves for small voltages with the Simmons model [46]. This model model considers a rectangular potential, which is in good agreement with symmetric tunnel junctions and same energy profiles on each side of the insulating barrier, while the Brinkman model describes a trapezoidal barrier considering different interface properties (see chapter 1). The Brinkman model did not converge for the experimental values so it not presented here [47].

	15 K	25 K	45 K	65 K
Barrier height (eV)	0.44	0.45	0.48	0.47
Thickness(Å)	21.5	21.3	20.8	21.1

Table I. Values of barrier heights and thicknesses obtained by fitting the IV curves of Figure 14 to the Simmons model.

As shown in table I, the values of the barrier thickness are small compared to those measured with XRR measurements around 3.5 nm. However, phenomena such as a minor Sr interdiffusion into the LCO layer could result in the presence of a thin interfacial metallic layer that would reduce the effective barrier thickness. As we have shown, the LCO is easy to dope with holes by introducing Sr in the lattice and there is an insulator/metal phase boundary at room temperature near Sr x=0.2 for $La_{1-x}Sr_xCoO_3$ [48]. In order to evaluate such posibility we have carried out atomic resolution STEM-EELS measurements, shown next.

4.2. STEM-EELS characterization of LSMO/ LCO/LSMO MTJ's

In order to understand the macroscopic effects of the LSMO/LCO/LSMO heterostructures, we study the local properties of the samples using the capabilities of the STEM-EELS. We will analyze aspects such as the presence of oxygen vacancies in the barrier, interdiffusion of Sr into the LCO layer or the fine structure of the Mn and Co $L_{2,3}$ edges in order to explain the origin of properties such as the change in the magnetic anisotropy of the top LSMO electrode.

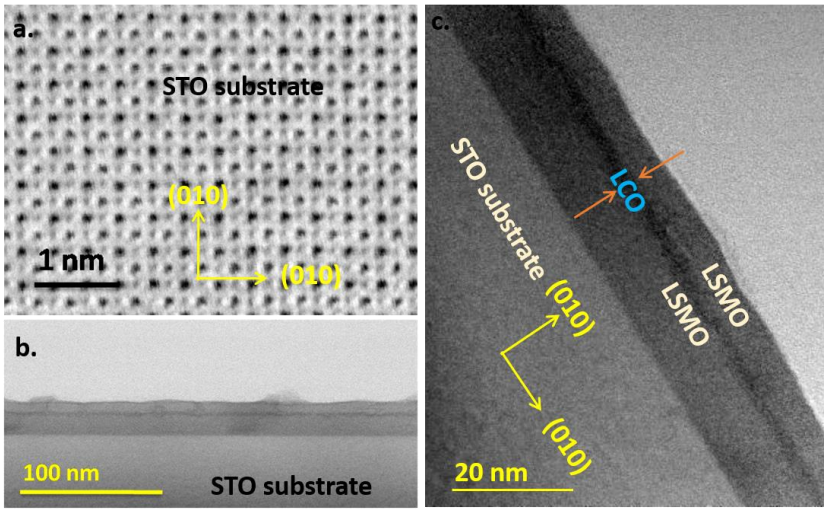

Figure 15. (a) Annular bright field image (ABF) of the STO(100) substrate showing the zone axis. (b) Low magnification ABF image of a $LSMO_{15nm}/LCO_{3nm}/LSMO_{8nm}$ trilayer. (c) Low magnification ABF image of the trilayer, where the LCO can be seen sandwiched between the two LSMO films.

Figure 15 exhibits several annular bright field images of a $LSMO_{15nm}/LCO_{3nm}/LSMO_{8nm}$ trilayer on STO(100). Figure 15a shows a high resolution ABF image of the substrate down the (100) zone axis. Low magnification images such as the ones in Figures 15b,c, show that the heterostructure is very flat over long lateral distances. The LCO layer is continuous, no pinholes or secondary phases are observed, and the LCO/LSMO interfaces are very flat.

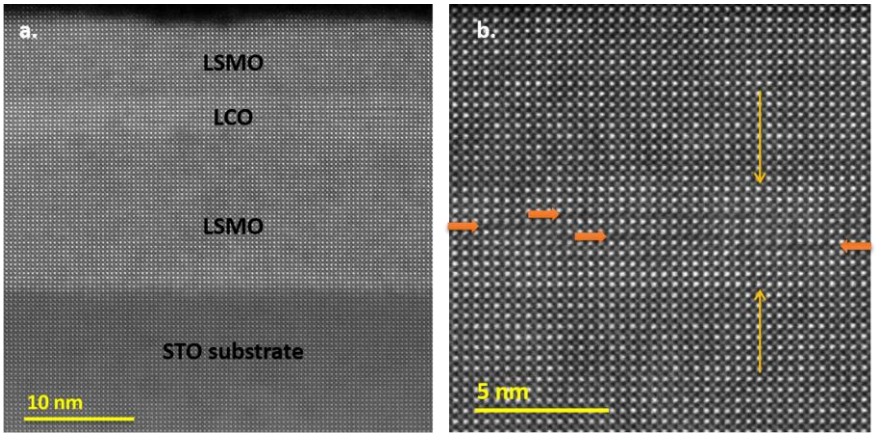

Figure 16. (a) High angle annular dark field image (HAADF) of the $LSMO_{15nm}/LCO_{3nm}/LSMO_{8nm}$ trilayer. (b) High resolution image of the same trilayer. The orange horizontal arrows indicate O vacancy rich planes. The vertical arrows indicate the width of the LCO film.

The high resolution HAADF images shown in Figure 16a show the high structural quality of the LSMO/LCO/LSMO interfaces and layers. The interfaces are coherent and free of major defects. However, some in-plane dark stripes can be detected within the LCO film. The dark stripes, highlighted by small orange horizontal arrows, correspond to dilated distances between adjacent LaO-LaO atomic planes separated by O deficient CoO_{2-x} planes. This result evidences the presence of oxygen vacancies clustering locally within CoO_2 planes such as those previously observed in ultrathin LSCO thin films [49,12]. The lateral length scale of these O-deficient platelets is of the order of a few nm, pointing to the presence of a low density of O vacancies.

We have used EELS to study the stoichiometry of the samples and interfaces. The dual EELS mode has been used to simultaneously acquire low and high energy-loss scales in order to analyze the possible presence

of Sr in the LCO as a result of interdiffusion during the growth process. A summary of the most significant results are presented in Figure 17.

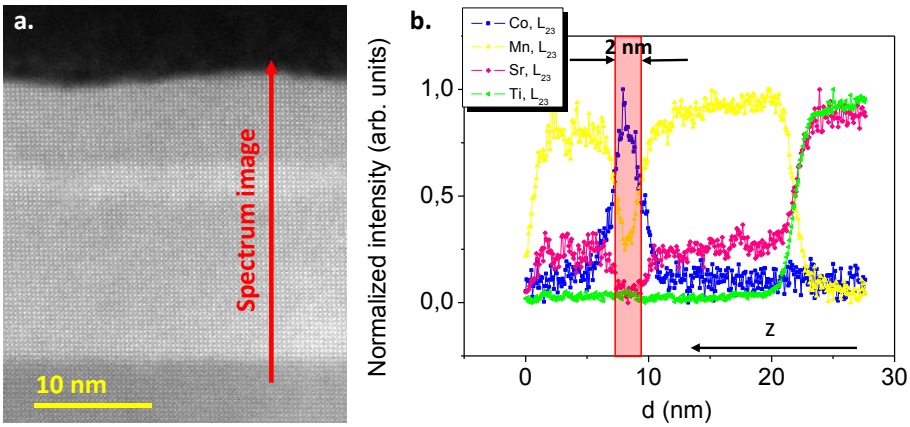

Figure 17. (a) HAADF image of a $LSMO_{15nm}/LCO_{3nm}/LSMO_{8nm}$ trilayer on STO(100). The red line corresponds to the direction of an EELS line-scan. (b) Normalized intensities corresponding to the integrated intensities below the Co, Mn, Sr and Ti $L_{2,3}$ edges. The black arrow indicates the growth direction and the red rectangle indicates the position of the LCO layer. Please, note that the direction of the scan has been rotated ninenty degrees respect to (a).

Figure 17a shows a HAADF image of the sample. The red line indicates the area where an EELS line-scan was acquired. The beam was raster scanned from the top to the bottom. The line scan was recorded using an energy dispersion of 0.25 eV/channel and an exposure time of 1.3 s/pixel, with a beam current of tens of pA. In Figure 17b, the normalized integrated intensities of the different signals of the Ti (green), Mn (yellow), Co (blue) and Sr (magenta) $L_{2,3}$ edges, with onsets around 452 eV, 642, 779 and 1950 eV respectively, are plotted along the heterostructure. The width of the LCO layer is around 2 nm (marked with a red rectangle). This result is in good agreement with the thickness values obtained by using the Simons model to fit the IV curves in MFTs (see previous section). Both the Sr (magenta) and the Mn (yellow) signals vanish within the LCO, pointing to negligible interdiffusion. Figure 18 summarizes a representative example, where atomic resolution chemical maps of a trilayer are presented. Images derived from the analysis of the La $M_{4,5}$, Mn $L_{2,3}$ and Co $L_{2,3}$ edges are shown in red, yellow and blue, respectively. Despite some spatial drift during measurements, a horizontal average can be made, shown in the right panel. The interfaces are chemically sharp and no Mn/Co intermixing is detected.

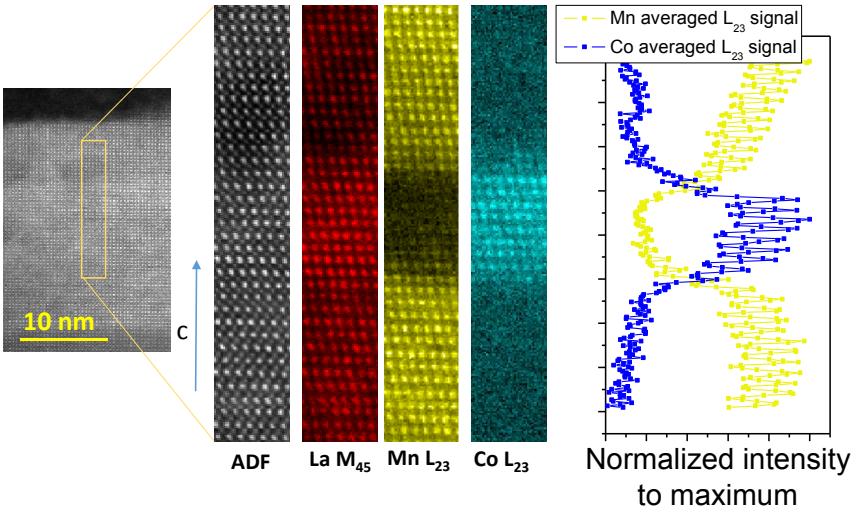

Figure 18. HAADF image of a $LSMO_{15nm}/LCO_{3nm}/LSMO_{8nm}$ trilayer. A yellow rectangle indicates the region of interest (ROI) for the spectrum image. Simultaneously acquired ADF signal along with the chemical maps extracted from the La $M_{4,5}$ (red), Mn $L_{2,3}$ (yellow), Co $L_{2,3}$ (blue) edges of an atomic resolution 2D EEL-spectrum image. Some spatial drift is present. The right panel shows the laterally averaged Mn (yellow) and Co (blue) signals.

To complete the experiment and analyze the interface electronic properties, we have studied the fine structure of the O *K* and the Mn and Co $L_{2,3}$ edges. This analysis can give significant information related to orbital reconstructions at interfaces, changes in the oxidation states, charge transfer processes, etc. An analysis of the O *K* edge pre-peak and the $L_{2,3}$ fine structure of the Co and Mn edges has been carried out for several spectrum images. As explained in section 1, we will make use of the difference in peak positions between the O *K* edge pre-peak and the adjacent main peak, ΔE, which increases with Mn oxidation state in mangnanites [32, 34]. We will use data from the literature to quantify the Mn oxidation state from the ELNES features through our LSMO/LCO/LSMO heterostructures [50-52]. For a qualitative study of the Co oxidation state in our LCO films, we will employ the values obtained for the L_{23} ratio from the reference films in section 1. The fit parameters obtained in this case are a=3.08±0.11 and b=2.2±0.6 (the correlation of the fit is 0.87). We will use these data as a calibration curve to quantify the Co valence in our ultrathin LCO barriers. Figure 19a exhibits some O *K* edges extracted from a spectrum image of a LSMO/LCO/LSMO heterostructure. The ROI is a rectangle comprising the LCO barrier and the top LSMO electrode. The simultaneous ADF exhibits some spatial drift. The red and blue squares mark the zones where the O *K* edge signals have been normalized in the LSMO and LCO layer, respectively. The pre-peak feature at the onset of the edge (near 527 eV) is suppressed in the LCO layer. This observation confirms that some degree of O deficiency exists in the dark stripes seen in Figure 16b.

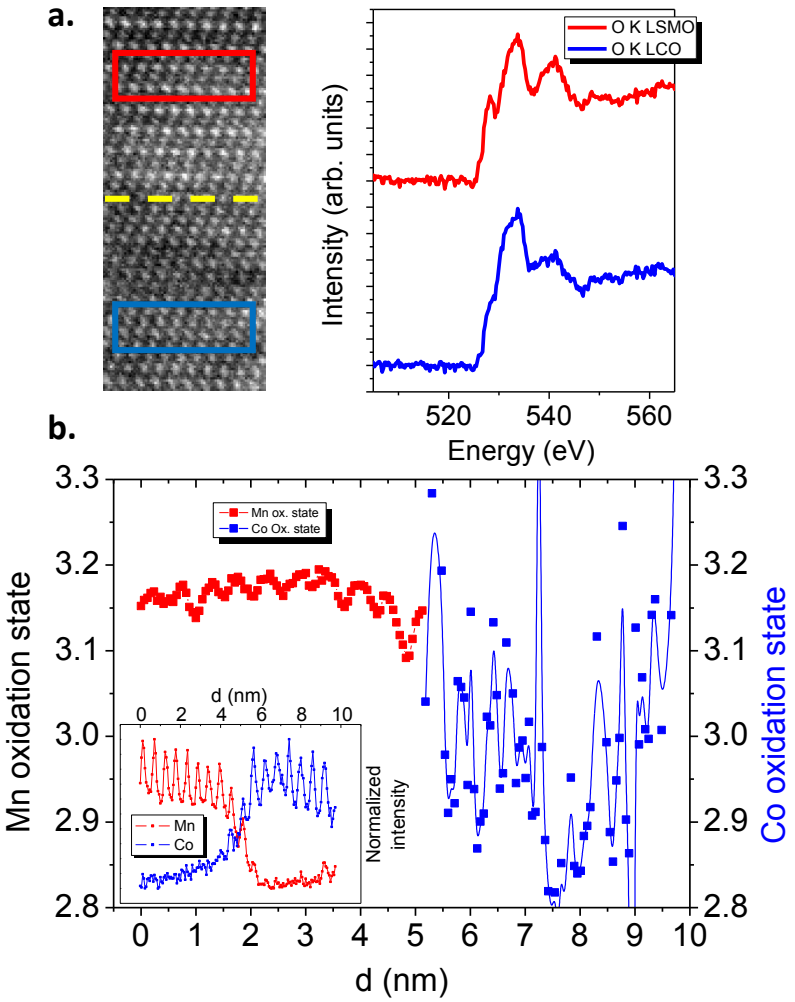

Figure 19. (a) ADF signal simultaneously acquired with a spectrum image acquired on a region in a LSMO/LCO/LSMO trilayer including a LCO / LSMO interface, which is highlighted by a yellow dashed line. The red rectangle marks the zone in the LSMO that was used to generate the averaged O *K* edge signal (red curve) displayed on the right panel. The blue square corresponds to the LCO zone, with the corresponding O *K* edge profile in blue (right) showing different features of the fine structure. (b) Mn oxidation state for the bilayer (black squares) and Co oxidation state (blue squares). The Mn oxidation state has been obtained using the ΔE method (O *K* edge) while the Co oxidation state has been quantified from the L_{23} ratio (hence, the noise) [35]. Inset: Mn and Co signals of the bilayer showing the interface location. Some spatial drift is present, which does not affect the lateral averaging performed here.

In Figure 19 the oxidation states of Mn and Co are plotted in black and blue, respectively, across a LCO/LSMO interface. The Figure in the inset shows the normalized integrated intensities of the Mn and Co $L_{2,3}$ edge signals. The point where the signals intersect can be used to accurately identify the position of the LCO/LSMO top interface. The values of the Co oxidation state are very noisy and surprisingly high for a deoxygenated layer in some regions, but they do not hinder a qualitative interpretation. It appears as the Co atoms exhibit a tendency to get further oxidized when approaching the LSMO interface. On the contrary, the Mn oxidation state tends to be reduced in the proximity of the LCO interface. Interestingly, the average Mn valence within the LSMO layer is fairly reduced when compared with the nominally expected value of +3.3, pointing to some degree of electron doping (possible due to the presence of O vacancies in the system). Unfortunately, the high degree of noise hinders an accurate analysis of any charge transfer in the system. Nevertheless, we can say that the electronic properties of our layers are not bulk-like, which probably affects the magnetism in general and the different anisotropy of the top LSMO electrode. In order to gain more insights into this issue a study of

LSMO/LCO and LCO/LSMO bilayers is presented in next section so we can deconvolve the magnetic properties of the top and bottom LSMO electrodes.

5. LSMO/LCO and LCO/LSMO bilayers

5.1. Magnetic characterization of bilayers

In the first place, we have carried out a structural and transport characterization of bilayers where LSMO and LCO are combined, changing the sequence of growth on the STO(100) substrates. Our main objective is to analyze and/or disregard growth sequence effects on the quality of the interfaces between both materials and also examine other structural effects on the different magnetic properties such as anisotropy. For this aim, a series of LCO/LSMO and LSMO/LCO samples on STO(100) have been grown.

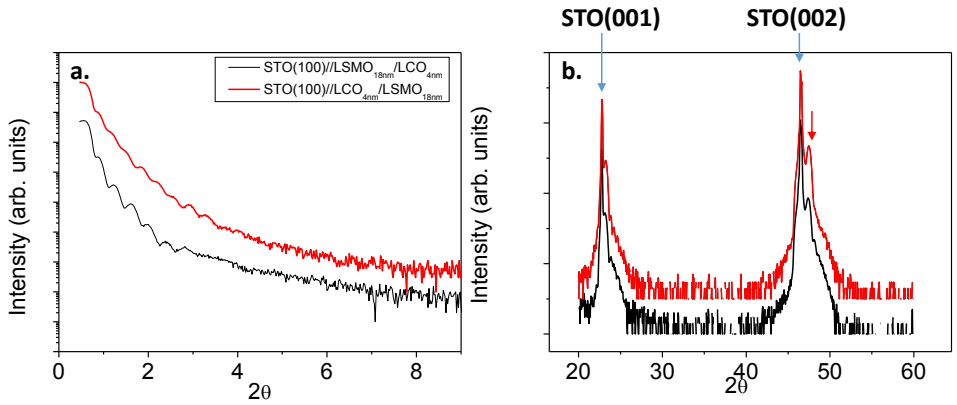

Figure 20. (a) XRR pattern of two bilayers with different sequences. The red curve corresponds to the STO(100)// LCO_{4nm}/ $LSMO_{18nm}$ bilayer, while the black one represents the STO(100)//$LSMO_{18nm}$/LCO_{4nm} specimen. (b) XRD patterns of the same samples (same color code). Blue arrows indicate the STO substrate reflections, and red arrows indicate the LSMO/LCO peak.

Figure 20 shows the X-ray reflectivity and the X-ray diffraction patterns of two bilayers. Both samples have been obtained under the same conditions but the top/bottom sequence in the growth is different. The red curves of Figures 20a and 20b correspond to a bilayer of LCO_{4nm}/$LSMO_{18nm}$, while the black ones correspond to a $LSMO_{18nm}$/LCO_{4nm} sample. Both types of heterostructures exhibit very high quality and appear flat and epitaxial. X-ray diffraction shows that, no matter the layer sequence, bilayers are uniformly strained to match the cubic in plane lattice parameters of the STO (100) what imposes a tensile epitaxial mismatch strain amounting 0.5% for the LSMO (a=3.87 Å) and 2% for the LCO (a=3.82 Å). Regarding the magnetic properties, hysteresis loops have been measured for the same samples at different temperatures in order to study the magnetic anisotropy.

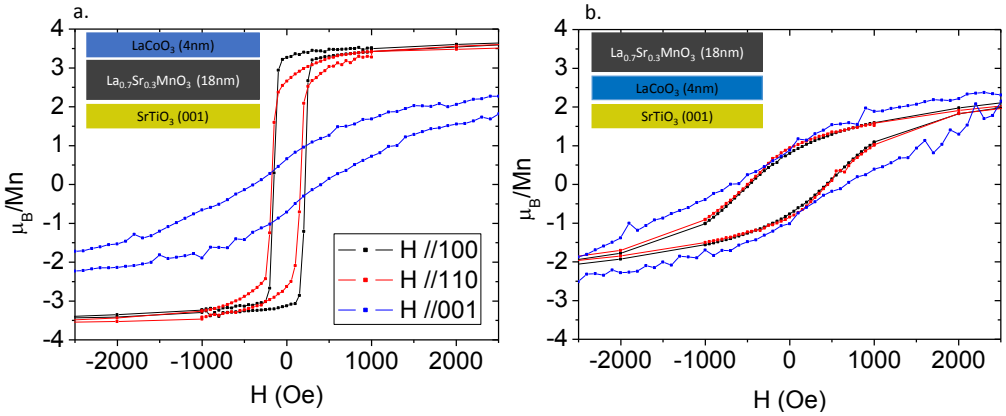

Figure 21. M(H) loops of the $LSMO_{18nm}/LCO_{4nm}$ (a) and $LCO_{4nm}/LSMO_{18nm}$ (b) at 5K with magnetic fields applied in plane along [100] (black squares), [110] (red squares) and out-of-plane [001] direction.

Figure 21 shows M(H) loops from both kind of bilayers with magnetic fields aligned along relevant [100], [110] (in plane), and [011] (out of plane) directions. The curves denote profound changes in the magnetic anisotropy. $LSMO_{18nm}/LCO_{4nm}$ samples show a biaxial in plane anisotropy with biaxial easy axes as shown previously in single layer manganites. A significant remanence is obtained in the out-of-plane loops, larger than that previously found in single manganite thin films. On the other hand, $LCO_{4nm}/LSMO_{18nm}$ samples were magnetically very different. M(H) loops show negligible in plane anisotropy and [100] and [110] in plane loops are quite similar to the out-of-plane [001] cycle, indicating that the sample is magnetically more isotropic, resembling the magnetic structure of the undistorted LSMO rhombohedral structure of bulk samples.

To gain further insights, two representative samples have been measured by Karoly Nagy and Titusz Feher using ferromagnetic resonance (FMR) in the Department of Physics of the Budapest University of Technology and Economics (Hungary). FMR spectra were recorded at 77 K and 9 GHz under an in plane rotating magnetic field. The angular dependence of the FMR for the two samples studied is shown in Figure 22. For rotations in the (*c*,*a*) plane we define the orientation with θ, where θ=0 refers to B//*c* and θ=90 to B//*a*, while for rotations in the (*a*,*b*) plane we define the orientation with Φ, where Φ=0 refers to B//*a* and Φ=45 to B//[110].

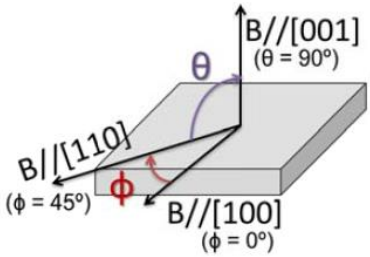

Figure 22. Schematics of the geometry of the sample with respect to the magnetic field.

The four minima of the FMR field, the radial value of the polar plot, along the [100] directions indicate the magnetic easy axis. These data can be explained in terms of the anisotropic magnetic free energy density:

$$f = -\mu_0 \boldsymbol{M} \cdot \boldsymbol{B_{applied}} \pm (\frac{1}{2}\mu_0 M_S^2 + K_{2c})\alpha_3^2 + K_{4ab}(\alpha_1^4 + \alpha_2^4) + K_{4c}\alpha_3^4$$

[1]

Which contains Zeeman, demagnetizing and magnetic anisotropy terms. In this expressions, M_s is the saturation magnetization ($\alpha_i=M_i/M_{sat}$, i=1,2,3 and $\alpha_1^2+\alpha_2^2+\alpha_3^2=1$), K_{2c} is the lowest order in-plane anisotropy term, K_{4ab} is the anisotropic in plane anisotropy and K_{4c} accounts for a higher order out of plane indistinguishable from the K_{2c} term without extra input. The anisotropy caused by $\mu_0 M_s$ is set to 0.75 T, which is equivalent to an extra easy-plane anisotropy with K_{2c}=219 KJ/m^3.

The resonance fields (B_0) are plotted vs. the rotation angles in Figure 23 (in-plane and out-of-plane rotations) for both types of bilayers. The data exhibit the typical sinusoidal variation of the FMR field, B_0 (T), vs. the angle between B and the sample. In Figures 23a and 23b, the top panels show the FMR fields B_0 measured experimentally (green spots) for the in-plane angles. In both samples, the results are characteristic of biaxial symmetry with easy axes along the [100] direction. The green points are the experimental values, while the blue line corresponds to theoretical simulations obtained. Despite the different shape of the in-plane graphs, the difference between the maxima and the minima in both samples is the same, 0.1 T. Bottom panels in Figure 23a and 23b display the B_0 vs. the out-of-plane angle. In this case, the red square indicates a zone where the theoretical results do not fit the experimental values.

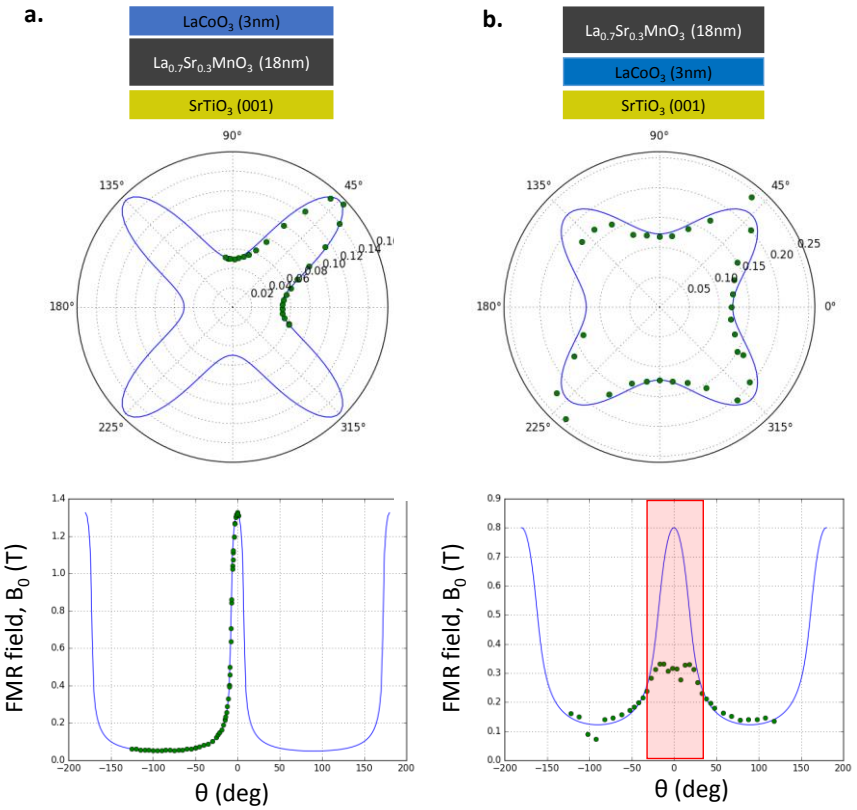

Figure 23. FMR resonance fields for the in-plane (top 360º circular plots) and out-of-plane (bottom plots) of (a) $LCO_{4nm}/LSMO_{18nm}$ bilayer and (b) $LSMO_{18nm}/LCO_{4nm}$ bilayer. Green spots correspond to experimental data and lines correspond to simulations obtained by using the classical model of equation [1] and parameters listed in Table II.

For both bilayers $LSMO_{18nm}/LCO_{4nm}$ and $LCO_{4nm}/LSMO_{18nm}$ we obtained, K_{4c}=0 (see Table II) since no higher order terms were needed for the description if the important features. However, while for $LSMO_{18nm}/LCO_{4nm}$ K_{2c}=71 KJ/m^3, for the $LCO_{4nm}/LSMO_{18nm}$ bilayer the negative K_{2c}=-83 KJ/m^3 indicates that without the shape anisotropy the magnetization would be perpendicular to the (001) preferred over [110]. It is

well known that STO distorts LSMO in such a way that in ultrathin LSMO the easy axis turns along the [100] direction.

	K_{2c} [KJ/m^3]	K_{4ab} [KJ/m^3]
$LSMO_{18nm}/LCO_{4nm}$	71	-8.3
$LCO_{4nm}/LSMO_{18nm}$	-83	-8.3

Table II. Anisotropy energies of LSMO/LCO and LCO/LSMO bilayers on STO(100) substrates at 77K.

It is worth to remark that although at first sight the similar values of the in plane anisotropy constant obtained for both kind of bilayers may seem inconsistent with the isotropic behavior found by M(H) loops in LCO_{4nm}/ $LSMO_{18nm}$ bilayer, it simply may result from the tendency of the manganite magnetization to point out of the plane in this sample. Moreover, a comparison is not straightforward since magnetization curves depends largely on inhomogeneities, domains and pinning. More relevant is the large difference in K_{2c} depending on whether the LCO is above or below the LSMO. FMR data show that without shape anisotropy the spins would favor perpendicular orientation when LSMO is grown of top of LCO. Also, the FMR was much broader (even beyond observation at certain B field directions) in this sample than in the other one, which is even consistent with small islands of perpendicular orientation (i.e. inhomogeneities with K_{2c} even defeating the shape anisotropy at some places). The slow saturation of the H//plane magnetization curves in LCO_{4nm}/ $LSMO_{18nm}$ bilayer is consistent with this.

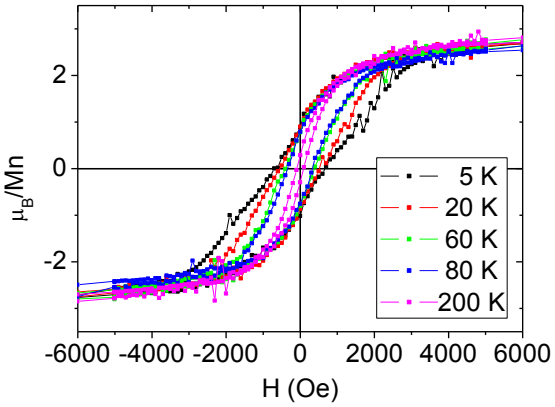

Figure 24. M(H) loops of the $LCO_{4nm}/LSMO_{18nm}$ samples at 5 (black line and symbols), 20 (red line and symbols), 60 (green line and symbols), 80 (blue line and symbols), 200K (magenta line and symbols) with magnetic field applied in plane in the [001] out of plane direction.

Figure 24 displays M(H) loops of the LCO_{4nm}/ $LSMO_{18nm}$ bilayer for several temperatures, where an intriguing widening at coercivity can be clearly observed, which suggests second magnetic phase with out of plane magnetization, and which disappears when the temperature is increased above the Curie point of the cobaltite. The large values of the associated magnetic moment indicate that the magnetic phase is related to the manganite and cannot be ascribed to the cobaltite layer of much lower thickness (and thus with much smaller saturation moment).

5.2. Structural characterization of bilayers.

The change in magnetic behavior can be discussed in the frame of different structural distortions within the LSMO layers. Bulk LSMO single crystals have [111] easy axes imposed by the rhombohedral distortion of its orthorhombic lattice. However, LSMO thin films on STO experience tetragonal distortions in the plane, which enlarge the in-plane parameters of the LSMO to match the square lattice of the STO substrate. The LSMO layers have biaxial in-plane anisotropy with [110] easy axis and [100] hard axes [53]. The magnetic measurement results obtained in section 5.1 suggest that both bilayers are in the same uniformly strained state macroscopically (see Figure 22), but the expanded lattice at the oxygen vacancies of the cobaltite (see Figure 16) can trigger a modification in the pattern of distortions. These distortions nucleating within the LCO layer can propagate into the manganite, giving rise to local inhomogenities in the LSMO upper layer, which could be responsible for the modification of the magnetic state.

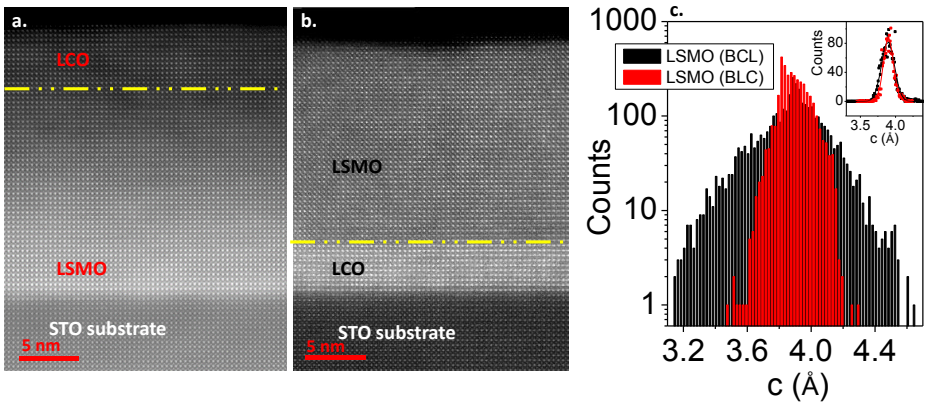

Figure 25. (a) Atomic resolution HAADF images of a STO/$LSMO_{18nm}$ /LCO_{4nm} (left) and a STO /LCO_{4nm} /$LSMO_{18nm}$ (right) bilayer. The yellow dashed lines indicate the interfaces between the LSMO and LCO layers. (b) Histograms (logarithmic scale) of the distribution of values of the LSMO layer *c* lattice parameter, calculated from column-by-column analyses of a number of atomic resolution images. Red (black) data correspond to the STO/ $LSMO_{18nm}$ /LCO_{4nm} (STO / LCO_{4nm} /$LSMO_{18nm}$). Inset: Histogram for the *c*-axis distribution measured on the STO(100) substrate for both samples, same color code, along with Gaussian fits (used for calibration) The scale bars represent 5 nm.

This effect is evident from the analysis of the local structure in HAADF images such as the ones in Figures 25a and 25b for both types of samples. The lattice constant of the perovskite block can be quantified in real space over lateral length scales of a hundred nm analyzing lattice dimensions in a unit-cell-by-unit-cell fashion. For this aim, we have measured the coordinates of the center of mass of the atomic columns of interest through a number of high resolution images. Once the individual columns are localized, a distribution of *c*-axis values can be obtained by subtracting nearest-neighbor coordinates along the growth direction. Since STEM images are prone to scan artifacts, we have used the substrate histogram distribution (inset, same color code) as an internal spatial calibration. This way, it is possible to track the evolution of the *c* lattice parameter across the LSMO layers of our samples. Figure 25b plots the histograms of the distribution of *c* lattice constant values obtained from our analysis. Black (red) data correspond to the LCO_{4nm}/$LSMO_{18nm}$ ($LSMO_{18nm}$/LCO_{4nm}) bilayer. The average lattice parameters of both samples are very close to each other, 3.88 vs. 3.89 Å, which is consistent with the X ray diffraction data. However, the distribution of *c* values in the LCO_{4nm}/$LSMO_{18nm}$ sample (LSMO on top, black) is noticeably wider than the case when LSMO grows directly on top of the single crystal substrate. This finding points to a lower degree of structural homogeneity when the manganite is deposited on top of the oxygen deficient cobaltite layer. Indeed, the data suggest that the lattice expansions around oxygen vacancies

(nucleating in the cobaltite) propagate well into the manganite layer disrupting the cubic order imposed by the STO. On the other hand, when the cobaltite is the top layer as in $LSMO_{18nm}/LCO_{4nm}$ samples, our maps show a more regular, undistorted structure with a lower dispersion of lattice constant values.

6. Conclusions

Across this chapter, we have fabricated heterostructures based on LSMO and LCO thin films, aimed at the fabrication of MTJ's using LCO as ferromagnetic barrier. We have confirmed that all LSMO, LSMO and trilayers are epitaxial and of high structural quality. Insulating behavior is observed for the LCO thin films as expected, and the magnetic properties of the LSMO and LCO thin films correspond with results obtained before. The tunnel conductance has been measured in the devices but very low TMR values of 3% have been obtained. In addition, the results obtained in the RH curves of Figure 16 reveal that the LSMO upper electrode is in a hard axis when the magnetic field is applied along the [110] direction, while the bottom LSMO electrode is in an easy axis with the coercive field around 80 Oe, as expected. We have analyzed by STEM-EELS aspects such as the presence of oxygen vacancies in the barrier, interdiffusion of Sr into the LCO layer and the fine structure of the Mn and Co $L_{2,3}$ edges in order to explain the origin of the properties, such as the change in the magnetic anisotropy of the top LSMO electrode. The STEM results give proof of a high structural quality of the heterostructures. O vacancies are present in the LCO barrier, but they are not arranged in an ordered fashion as in the LSCO films. The La-La interatomic distances around the CoO_{2-x} dark stripes are in good agreement with the literature for LCO strained thin films and the section 1 of this chapter. We have verified that there is no major Sr interdiffusion from the LSMO into the LCO barrier, but we have also observed that the interfaces are not atomically abrupt. The effective thickness of the LCO layer measured by EELS is of 2 nm, which corresponds with the thickness predicted using the Simons model from the IV curves. An analysis of the fine structure of the O *K*, Mn $L_{2,3}$ and Co $L_{2,3}$ edges has been done. The small pre-peak of the O *K* edge suggests again the presence of oxygen vacancies in the LCO layer. On the other hand, the Mn is slightly reduced in the interface while the Co is oxidized. The profile obtained in Figure 19 shows that Co atoms are reduced in the middle of the layer. This last result suggests a charge transfer process of electrons from the LCO to the LSMO layer. However, these results do not explain the origin of the anisotropy observed in the LSMO top electrode.

In order to study separately both LSMO layers, we have studied the top and bottom LSMO layer independently by growing bilayers combining LCO and LSMO. In these samples the magnetic anisotropy of the LSMO is surprisingly different when it is grown on top of a LCO buffer layer. The [110] easy axis of bulk LSMO becomes a hard axis and the magnetization does not saturate. FMR measurements demonstrate that LSMO layers on top of LCO change their easy axis to the out-of-plane direction. This finding indicates that magnetic interactions occurring at the interface with the cobaltite may trigger out-of-plane moments in the manganite. In fact, this is consistent with the out-of-plane low temperature magnetization loops of Figure 24, which suggest a second magnetic phase with out-of-plane magnetization that disappears when the temperature is increased above the Curie temperature of the LCO.

The analysis of atomic resolution STEM images throws differences in the structural features of top and bottom LSMO electrodes. The histogram presented in Figure 25 reveals a wider distribution of the *c* axis values in the LSMO layer when it is grown on top of LCO. This result can be understood having in mind that the LCO layer has oxygen vacancies distributed in nanometric platelets which give rise to inhomogeneous strain fields. These can propagate towards the surface, distorting locally the LSMO *c* axis. On the other hand, FMR data show that without shape anisotropy the spins would favor perpendicular orientation when LSMO is grown on top of

LCO, which is in good agreement with the fact that the modifications in the bond distances propagate into the manganite control the magnetic anisotropy through their effect on band width and orbital polarization [54]. Finally, it would be of great interest to measure LSMO reciprocal space maps for bilayers with different sequences to refine the distortions in the LSMO films.

7. References

[1] R. Ramesh, D.G. Schlom, "Whither Oxide Electronics", *MRS Bull.* **33,** 1006–1014 (2008).

[2] C.H. Kim, G. Qi, K. Dahlberg, W. Li, "Strontium-doped perovskites rival platinum catalysts for treating NOx in simulated diesel exhaust", *Science.* **327,** 1624–1627 (2010).

[3] M. Imada, A. Fujimori, Y. Tokura, "Metal-insulator transitions", *Rev. Mod. Phys.* **70**, 1039–1263 (1998).

[4] S. Yamaguchi, Y. Okimoto, H. Taniguchi, Y. Tokura, "Spin-state transition and high-spin polarons in $LaCoO_3$"., *Phys. Rev. B.*. **53,** R2926–R2929 (1996).

[5] S.R. English, J. Wu, C. Leighton, "Thermally excited spin-disorder contribution to the resistivity of $LaCoO_3$," *Phys. Rev. B.* **65,** 220407 (2002).

[6] S. Park, P. Ryan, E. Karapetrova, J.W. Kim, J.X. Ma, J. Shi, J.W. Freeland, W. Wu, "Microscopic evidence of a strain-enhanced ferromagnetic state in $LaCoO_3$ thin films", *Appl. Phys. Lett.* **95,** 0-3 (2009).

[7] V. Mehta, Y. Suzuki, "Ferromagnetism enhanced by structural relaxation of biaxially compressed $LaCoO_3$ films", *J. Appl. Phys.* **109,** 07D717 (2011).

[8] A. Herklotz, A.D. Rata, L. Schultz, K. Dörr, "Reversible strain effect on the magnetization of $LaCoO_3$ films", *Phys. Rev. B* **79,** 1–4 (2009).

[9] D. Fuchs, E. Arac, C. Pinta, S. Schuppler, R. Schneider, H. V. Löhneysen, "Tuning the magnetic properties of $LaCoO_3$ thin films by epitaxial strain", *Phys. Rev. B* **77,** 1–8 (2008).

[10] G.E. Sterbinsky, P.J. Ryan, J.W. Kim, E. Karapetrova, J.X. Ma, J. Shi, J.C. Woicik, "Local atomic and electronic structures of epitaxial strained $LaCoO_3$ thin films", *Phys. Rev. B* **85,** 1–5 (2012).

[11] H. Hsu, P. Blaha, R.M. Wentzcovitch, "Ferromagnetic insulating state in tensile-strained $LaCoO_3$ thin films from LDA + U calculations", *Phys. Rev. B* **85**, (2012)

[12] N. Biskup, J. Salafranca, V. Mehta, M.P. Oxley, Y. Suzuki, S.J. Pennycook,S.T. Pantelides, M. Varela, "Insulating ferromagnetic $LaCoO_{3-\delta}$ films: A phase induced by ordering of oxygen vacancies", *Phys. Rev. Lett.* **112,** 1–5 (2014).

[13] A. Herklotz, M.D. Biegalski, H.M. Christen, E.-J. Guo, K. Nenkov, a D. Rata, et al., "Strain response of magnetic order in perovskite-type oxide films.", *Philos. Trans. A. Math. Phys. Eng. Sci.* **372**, 20120441 (2014).

[14] J. Wu, C. Leighton, "Glassy ferromagnetism and magnetic phase separation in $La_{1-x}Sr_xCoO_3$", *Phys. Rev. B.* **67,** 174408 (2003).

[15] G. Blasse, "Magnetic properties of mixed metal oxides containing trivalent cobalt", *J. Appl. Phys.* **36** , 879–883 (1965).

[16] J.B. Goodenough, P.M. Raccah, "Complex vs band formation in perovskite oxides", *J. Appl. Phys.* **36**, 1031–1032 (1965).

[17] P.M. Raccah, J.B. Goodenough, "First-order localized-electron collective-electron transition in $LaCoO_3$", *Phys. Rev.* **155,** 932–943 (1967).

[18] V.G. Bhide, D.S. Rajoria, G.R. Rao, C.N.R. Rao, "Mössbauer studies of the high-spin-low-spin

equilibria and the localized-collective electron transition in $LaCoO_3$", *Phys. Rev. B.* **6**, 1021–1032 (1972).

[19]K. Asai, O. Yokokura, N. Nishimori, H. Chou, J.M. Tranquada, G. Shirane, S. Higuchi, Y. Okajima, K. Kohn, "Neutron-scattering study of the spin-state transition and magnetic correlations in $La_{1-x}Sr_xCoO3$ (x=0 and 0.08)", *Phys. Rev. B.* **50**, 3025–3032 (1994).

[20]M. Itoh, I. Natori, S. Kubota, K. Motoya, "Hole-doping effect on magnetic properties of $La_{l-x}Sr_xCoO_3$", *J. Magn. Magn. Mater.* **140,** 1811–1812 (1995).

[21]S. Yamaguchi, Y. Okimoto, H. Taniguchi, Y. Tokura, "Spin-state transition and high-spin polarons in $LaCoO_3$", **53**, 2926–2929 (1996).

[22]M. Korotin, S. Ezhov, I. Solovyev, V. Anisimov, D. Khomskii, G. a Sawatzky, "Intermediate-spin state and properties of $LaCoO_3$", *Phys. Rev. B.* **54,** 5309–5316 (1996).

[23]J.S. Zhou, J.Q. Yan, J.B. Goodenough, "Bulk modulus anomaly in $RCoO_3$ (R=La, Pr, and Nd)", *Phys. Rev. B* **71**, 1–4 (2005).

[24]M. Tachibana, T. Yoshida, H. Kawaji, T. Atake, E. Takayama-Muromachi, "Evolution of electronic states in $RCoO_3$", *Phys. Rev. B.* **77**, 094402 (2008).

[25]M.W. Haverkort, Z. Hu, J.C. Cezar, T. Burnus, H. Hartmann, M. Reuther, C. Zobel, T. Lorenz, A. Tanaka, N. B. Brookes, H. H. Hsieh, H.-J. Lin, C.T. Chen, L. H. Tjeng, "Spin State Transition in $LaCoO_3$ Studied Using Soft X-ray Absorption Spectroscopy and Magnetic Circular Dichroism", *Phys. Rev. Lett.* **97**, 176405 (2006).

[26]N. Feature, "Enter the Oxides", *Nature* **459**, 28–30 (2009).

[27]N. Sundaram, Y. Jiang, I.E. Anderson, D.P. Belanger, C.H. Booth, F. Bridges, J.F. Mitchell, Th. Proffen, H. Zheng, "Local structure of $La_{1-x}Sr_xCoO_3$ determined from EXAFS and neutron pair distribution function studies", *Phys. Rev. Lett.* **102**, 1–4 (2009).

[28]R. D. Leapman, L. A. Grunes, P. L. Fejes, "Study of the L_{23} edges in the 3d transition metals and their oxides by eels with comparisons to theory", *Phys. Rev. B.* **26** (1982).

[29]T.G. Sparrow, B.G. Williams, C.N.R. Rao, J.M. Thomas, "L_3/L_2 white-line intensity ratios in the electron energy-loss spectra of 3d transition-metal oxides", *Chem. Phys. Lett.* **108**, 547–550 (1984).

[30]H. Kurata, E. Lefèvre, C. Colliex, R. Brydson, "Electron-energy-loss near-edge structures in the oxygen K -edge spectra of transition-metal oxides", *Phys. Rev. B.* **47,** 13763–13768 (1993).

[31]W.G. Waddington, P. Rez, I.P. Grant, C.J. Humphreys, "White lines in the $L_{2,3}$ electron-energy-loss and x-ray absorption spectra of 3d transition metals", *Phys. Rev. B.* **34**, 1467–1473 (1986).

[32]M. Varela, M. Oxley, W. Luo, J. Tao, M. Watanabe, A. Lupini, S.T. Pantelides, S.J. Pennycook "Atomic-resolution imaging of oxidation states in manganites" *Phys. Rev. B.* **79**, 085117 (2009).

[33]M. Abbate, J.C. Fuggle, a. Fujimori, L.H. Tjeng, C.T. Chen, R. Potze, G. A. Sawatzky, H. Eisaki, S. Uchida, "Electronic structure and spin-state transition of $LaCoO_3$", *Phys. Rev. B.* **47**, 16124–16130 (1993).

[34]M. Varela, M. Oxley, W. Luo, J. Tao, M. Watanabe, A.R. Lupini, S.T. Pantelides, S.J. Pennycook, "Atomic-resolution imaging of oxidation states in manganites", *Phys. Rev. B.* **79**, 1–14 (2009).

[35]M. Varela, J. Gazquez, S.J. Pennycook, "STEM-EELS imaging of complex oxides and interfaces", M*RS Bull.* **37**, 29–35 (2012).

[36]J. Gazquez, W. Luo, M.P. Oxley, M. Prange, M. a. Torija, M. Sharma, C. Leighton, S. T. Pantelides, S. J. Pennycook, M. Varela, "Atomic-Resolution Imaging of Spin-State Superlattices in Nanopockets within Cobaltite Thin Films", *Nano Lett.* **11**, 973–976 (2011).

[37]L.J. van der Pauw, "A method of measuring the resistivity and Hall coefficient on lamellae of arbitrary shape", *Philips Tech. Rev.* **20**, 220–224 (1958).

[38]Y.Y. Zhang, R. Mishra, T.J. Pennycook, A.Y. Borisevich, S.J. Pennycook, S.T. Pantelides, "Oxygen disorder, a way to accommodate large epitaxial strains in oxides", *Adv. Mater. Interfaces.* **2** (2015).

[39]V. V Mehta, N. Biskup, C. Jenkins, E. Arenholz, M. Varela, Y. Suzuki, "Long-range ferromagnetic order in $LaCoO_{3-\delta}$ epitaxial films due to the interplay of epitaxial strain and oxygen vacancy ordering", *Phys. rev. B* **91**, 1–12 (2015).

[40]J.W. Han, B. Yildiz, "Enhanced one dimensional mobility of oxygen on strained $LaCoO_3$(001) surface", J. Mater. Chem. **21**, 18983–18990 (2011).

[41]J. Coey, M. Viret, S. Von Molnar,"Mixed-valence manganites", *Physics* **48**, 167–293 (1999).

[42]Y. Tokura, N. Nagaosa, "Orbital Physics in Transition Metal Oxides", *Science* **288**, 462–468 (2009).

[43]Y. Konishi, Z. Fang, M. Izumi, T. Manako, M. Kasai, H. Kuwahara, M. Kawasaki, K. Terakura, Y. Tokura, "Orbital-state-mediated phase-control of manganites", *J. Phys. Soc. Japan.* **68**, 3790–3793 (1999).

[44]A. Urushibara, T. Arima, A. Asamitsu, G. Kido, Y. Tokura, "Insulator-metal transition and giant magnetoresistance in $La_{1-x}Sr_xMnO_3$", *Phys. Rev. B.* **51**, 14103–14109 (1995).

[45]H. Fujishiro, "Phase-transition to antiferromagnetic state in $La_{1-x}Sr_xMnO_3$ (x-greater-than-or-equal-to-0.5)", *J. Phys. Soc. Japan.* **67**, 1799–1800 (1998).

[46]J.G. Simmons, "Generalized Formula for the Electric Tunnel Effect between Similar Electrodes Separated by a Thin Insulating Film", *J. Appl. Phys.* **34**, 1793–1803 (1963).

[47]W.F. Brinkman, R.C. Dynes, J.M. Rowell, "Tunneling conductance of asymmetrical barriers", *J. Appl. Phys.* **41**, 1915–1921 (1970).

[48]A.. Moodenbaugh, B. Nielsen, S. Smabasivan, D.A. Fischer, T. Friessnegg, S. Aggarwal, R. Ramesh, R.L. Pfeffer, "Hole-state density of $La_{1-7}Sr_xCoO_{3-\delta}$ ($0<x<0.5$) across the insulator/metal phase boundary", *Phys. Rev. B.* **61,** 5666–5671 (2000).

[49]M. a. Torija, M. Sharma, M.R. Fitzsimmons, M. Varela, C. Leighton, "Epitaxial $La_{0.5}Sr_{0.5}CoO_3$ thin films: Structure, magnetism, and transport", *J. Appl. Phys.* **104**, 023901 (2008).

[50]J.H. Rask, B.A. Miner, P.R. Buseck, "Determination of manganese oxidation states in solids by electron energy-loss spectroscopy", *Ultramicroscopy*. **21**, 321–326 (1987).

[51]J.H. Paterson, O.L. Krivanek, "Elnes of 3d transition-metal oxides", *Ultramicroscopy* **32**, 319–325 (1990).

[52]T. Riedl, T. Gemming, W. Gruner, J. Acker, K. Wetzig, "Determination of manganese valency in $La_{1-x}Sr_xMnO_3$ using ELNES in the (S)TEM", *Micron.* **38**, 224–230 (2007).

[53]Y. Suzuki, H.Y. Hwang, S.-W. Cheong, T. Siegrist, R.B. van Dover, A. Asamitsu,Y. Tokura, "Magnetic anisotropy of doped manganite thin films and crystals", *J. Appl. Phys.* **83,** 7064 (1998).

[54]H. Boschker, M. Mathews, E.P. Houwman, H. Nishikawa, A. Vailionis, G. Koster, G. Koster, G. Rijnders, D.H.A. Blank, "Strong uniaxial in-plane magnetic anisotropy of (001)- and (011)-oriented $La_{0.67}Sr_{0.33}MnO_3$ thin films on $NdGaO_3$ substrates", *Phys. Rev. B* **79,** 1–6 (2009).

Chapter 4: Oxygen vacancy doping in multiferroic tunnel junctions

Multiferroic tunnel junctions (MFTJ) are tunnel junctions with ferromagnetic electrodes and ferroelectric barriers, which allow ferroelectric control of the tunneling spin polarization through the magnetoelectric coupling at the ferromagnetic/ferroelectric interface [1-6]. In the last few years, efforts to improve design and functionality of MTJs have focused on barrier engineering [7-9]. In this work, we have explored new avenues to modulate doping by introducing an extra player: O vacancies. These point defects may act as electronic donors but also can be mobile and hence be transferred between electrodes, possibly providing additional functionalities. For example, in resistive switching devices, the interface-type conducting path can be driven by electrochemical migration of oxygen vacancies [10]. To this aim, we introduced an interface between the barrier and the top electrode consisting in an additional layer that will act as O vacancy reservoir, so carriers can be injected into the FE barrier. In fact, we will show how ferroelectric tunnel junctions with $La_{0.7}Sr_{0.3}MnO_3$ electrodes and $BaTiO_3$ tunneling barriers may exhibit an enhancement of the TER by up to ~10,000% thanks to the introduction of a 2 nm thick nominal $La_{0.86}Sr_{0.14}CuO_3$ ultrathin film in between the ferroelectric barrier and the top electrode. The 2 nm thick insulating cuprate layer stores a large density of oxygen vacancies and ensures an electronic screening asymmetry, which yields such large electroresistance upon the switching of the ferroelectric polarization. The drastic change in the TER is coupled with an inversion in the sign of the tunneling magnetoresistance (TMR) observed for a given polarization direction.

1. Introduction

In the past few years, magnetic tunnel junctions with ferroelectric barriers have attracted a great interest due the rich physics present along with their high potential for technological applications such as data storage [2]. Thanks to the advances in thin-film characterization and deposition techniques, it is now possible to control the switching of polarization of ferroelectric barriers like $BaTiO_3$ or $PbZrTiO_3$ with nanoscale thicknesses. Such possibility enables in a wide variety of functionalities, especially when combined with the control of magnetization of ferromagnetic electrodes [11-13]. For example, the nucleation of small ferroelectric domains with polarization vectors parallel to uncharged domain walls can cause large changes in the tunneling resistance upon polarization switching [3,9,7]. This behavior allows controlling the resistance through ferroelectric domains in a controlled fashion via an applied voltage. The process yields a multiplicity of memresistance states [14]. Along this line, further developments in barrier engineering may consist in introducing new elements between the ferroelectric barrier and one of the electrodes. For instance, Yin et al. have proposed the introduction of an ultrathin $La_{0.5}Ca_{0.5}MnO_3$ layer, 2 nm thick, between the upper electrode and the ferroelectric barrier which yielded in a very large TER effect for $La_{0.7}Sr_{0.3}MnO_3/BaTiO_3/La_{0.7}Sr_{0.3}MnO_3$ junctions [7]. More recently, Liu et al. studied theoretically the effect of ferroelectric polarization on the TER effect in a metal-ferroelectric-semiconductor FTJ taking $SrRuO_3/BaTiO_3/n\text{-}SrTiO_3$ as a model system. They found a metallic interface at the $n\text{-}SrTiO_3$ side in the ON state, which reduced the barrier width. This width is controlled, as a space charge region, by the band alignment between the semiconductor and the ferroelectric insulator [8].

In our experiment, an ultrathin film of nominal $La_{0.84}Sr_{0.16}CuO_{3-\delta}$ (LSCuO) has been introduced between the ferroelectric barrier and the top electrode in order to break the symmetry of the junctions and introduce

oxygen vacancies as a new degree of freedom in the system. LSCuO has been reported to behave as a hole-doped semiconductor, just like most cuprates [15,16]. It exhibits a wide range of oxygen stoichiometries while maintaining the basic perovskite structure, being its properties are very sensitive to changes in the doping level [17]. Most interestingly, LSCuO tends to accumulate a high density of oxygen vacancies. For these reasons, along with the chemical affinity to LSMO, we have chosen LSCuO for our experiment.

2. $La_{0.86}Sr_{0.14}CuO_3$ as an oxygen vacancy reservoir

We have introduced an ultrathin film of the nominal $La_{1.84}Sr_{0.16}CuO_3$ between the ferroelectric and the top manganite contact of asymmetric $La_{0.7}Sr_{0.3}MnO_3$/ $BaTiO_3$/ $La_{0.7}Sr_{0.3}MnO_3$ (LSMO/BTO/LSMO) junctions. The parent compound $LaCuO_{3-\delta}$ belongs to the lanthanum copper oxide family which has been considered as a potential source of superconducting materials. However, superconductivity has not been found. It seems that the determining factor is that a 3D network of O-Cu-O bonds can be found in $LaCuO_3$, contrary to the 2D (planar) structure of high Tc-superconductors. There is a large uncertainty regarding the electrical and magnetic properties of this material, probably due to uncertainties about oxygen deficiency. $LaCuO_{3-\delta}$ exhibits a remarkably wide oxygen stoichiometry range, $0 \leq \delta \leq 0.5$, displaying at least three well-ordered structures. A model of $LaCuO_{3-\delta}$ proposed by M.T. Czyzyk and G. A. Sawatzky predicted this material to be an insulator for the ideal stoichiometric tetragonal phase, a poor metal (doped semiconductor) for $0 \leq \delta \leq 0.5$, and again an insulator for $\delta=0.5$ [16]. Regarding magnetic properties, $LaCuO_3$ was predicted to be antiferromagnetic in all doping ranges, but for intermediate values it is very likely that some ferromagnetic component may develop due to disorder and moment canting. These results are in agreement with the experimental findings by J. F. Bringley et al., which show that the copper valence varies continuously from 3+ to 2+ in the oxygen-defficient perovskite [18]. A tetragonal phase exists between $0 < \delta \leq 0.2$, and a monoclinic phase is found between $0.2 \leq \delta \leq 0.4$. Both phases are metallic with room-temperature resistivities of $(1.0\text{-}3.0)\text{x}10^{-3}$ Ω cm. Above doping levels of 0.4, the phase turns into an orthorhombic structure and the material becomes an insulator again. It presents a ferromagnetic behavior in the tetragonal phase but it disappears at the $\delta \approx 0.2$ phase boundary [17,18]. The parent compound is extremely difficult to prepare with a stoichiometric tetragonal phase without oxygen vacancies.

The role of Sr addition in the $LaCuO_3$ parent compound is to stabilize a perovskite structure [15], associated with the presence of trivalent copper ions that are created to balance charge neutrality. With increasing concentrations of trivalent copper ions upon to Sr doping, lanthanum copper oxide evolves from a semiconductor to a metallic conductor. Several Sr-doped lanthanum copper oxides have been reported to crystallize in an oxygen deficient perovskite structure. Typically, $La_{1-x}Sr_xCuO_{2-\delta}$ has a tetragonal cell of $a \approx 2\sqrt{2}\ a_p$ and $c \approx a_p$ (a_p is the lattice parameter of the primitive cubic perovskite, 3.84 Å) for $0.15 \leq x \leq 0.25$ [19].

3. Ferromagnetic $La_{0.7}Sr_{0.3}MnO_3$ electrodes and ferroelectric $BaTiO_3$ barrier

Barium titanate (BTO) is a wide band-gap insulator that exhibits ferroelectric behavior at room temperature. It presents a perovskite structure, and has a structural phase transition at Tc = 393 K from a paraelectric cubic (a = b = c = 4.000 Å) to a ferroelectric tetragonal structure (a = b = 3.987 Å and c = 4.040 Å). The saturation polarization is $P_s = 25\ \mu C \cdot cm^{-2}$. The Ti^{+4} ions move away from their equilibrium position (which corresponds to

the center of the oxygen octahedra), giving rise to a finite dipolar moment. BTO presents another structural phase transition is present below T = 278 K, to an orthorhombic structure (a = 5.704 Å, b = 3.963 Å, c = 5,683 Å, and P_s = 33 $\mu C \cdot cm^{-2}$), and then at T = 183 K to a rhombohedrical structure (a = 5.704 Å, θ = 89.56º, and P_s = 33 $\mu C \cdot cm^{-2}$) [20]. These structural phase transitions result also in a change in the alignment of the polar axis, changing from the <100> in the tetragonal phase, <110> for the orthorhombic and <111> in the rhombohedric phase.

The strain state in perovskite oxide thin films can cause drastic changes in their properties. Ferroelectricity, in particular, is highly sensitive to external stress. Bulk ferroelectric properties can be enhanced in BTO thin-films using strain engineering. Biaxial compressive strain increases transition temperature nearly 500º C, and gives rise to values of the remanent polarization which are at least 250 % higher than those of bulk BTO [21]. The in-plane compression enhances tetragonality and favors spontaneous polarization along the *c*-axis, which reduces the ferroelectric critical thickness and allows implementing BTO as an active tunnel barrier. Theoretical calculations predicted the critical thickness to be in the range between 12 to 1 nm [22-27], but Gruverman et al. have evidenced the presence of ferroelectricity in BTO ultrathin-films grown on $SuRO_3$//$SrTiO_3$ with PFM experiments, reaching a critical thickness limit of 2.4 nm [12]. Also, V. Garcia *et al.* measured values of the critical thickness down to 1.2 nm [8].

When O vacancies are introduced in BTO, i.e, when the material is doped with electrons, ferroelectricity should be quenched because itinerant electrons screen the long range Coulomb interactions. However, these electrons partially stabilize ferroelectricity due to the screening of the strong crystal perturbation caused by the oxygen vacancies [28]. Actually, ferroelectric displacements have been observed in oxygen-reduced conducting BTO [28,29], and first-principles calculations have shown that the ferroelectric instability in BTO requires only a short-range portion of the Coulomb interactions of the order of the lattice constant, below a critical doping concentration n_c=0.11 e^-/u.c. [30]. Doping BTO with electrons below this critical concentration may enhance its range of functionalities, opening opportunities for using doped ferroelectrics in novel electronic devices.

As ferromagnetic electrodes we use $La_{0.7}Sr_{0.3}MnO_3$ (LSMO), which has been demonstrated to be ferromagnetic and has almost a 100% spin polarization (see chapter 3 for details).

4. Experimental results: growth and STEM-EELS characterization

A series of LSMO/BTO/LSCuO and LSMO/BTO/LSCuO/LSMO heterostructures were grown on (100) oriented $SrTiO_3$ substrates at 900ºC using high O_2 pressure RF sputtering system. After growth, an *in-situ* annealing was carried out in 900 mbar O_2 pressure at 700ºC [31]. XRR and XRD patterns have been measured with a Philips X´pert MRD diffractometer using a Cu tube as X-ray source (λ_x=1.541 Å).

Thin films of LSCuO were grown on STO(100) substrates using a nominal $La_{1.84}Sr_{0.16}CuO_3$ (LSCuO) target in order to determine structural and transport properties. These films exhibit a tetragonal phase (P4/mbm) $La_{1.54}Sr_{0.46}CuO_5$-like structure, which presents one vacancy every two unit cells.

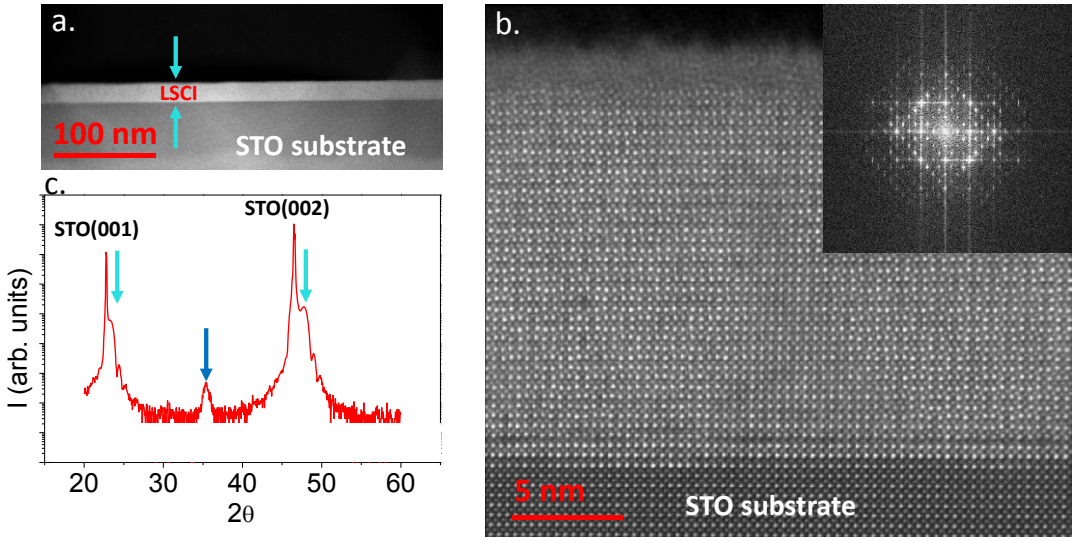

Figure 1. (a) Low magnification HAADF image of a 25 nm thin film of LSCuO on STO(100). (b) High resolution HAADF image of the same thin film. Inset: FFT of the thin films showing the superstructure (c) XRD diffraction pattern of the thin film. The cyan arrows indicate the substrate peaks and the blue one indicates the double perovskite peak of the LSCuO thin film.

Figure 1 displays a 25 nm LSCuO thin film grown on STO(100). The film grows flat and epitaxial over long lateral distances. Figure 1b shows an atomic resolution Z-contrast image. The interface is coherent and the crystal quality is high. A clear ripple in the crystal structure of the film is visible, which is characteristic of the features mentioned above. Figure 1c exhibits an XRD pattern that shows a peak at 35º, which corresponds to the doubling of the unit cell resulting from the oxygen deficient phase. This phase implies a reduction in the oxygen content in a 20% respect to the nominal composition of the LSCuO target.

The resistance of the thin films has been measured using the Van der Pauw. Four electrical contacts were made on the surface of the sample by evaporating a thin silver layer. In order to study the dependence of the transport properties on the oxygen vacancies content, two twin samples where measured under different conditions.

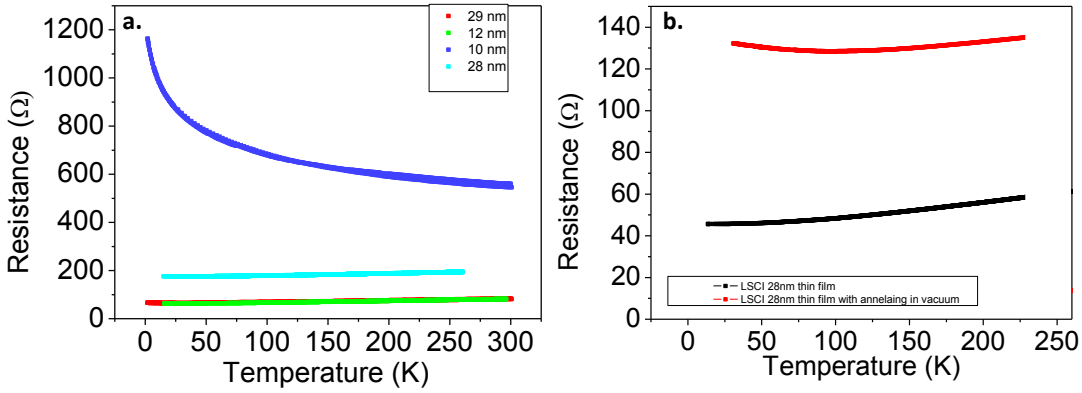

Figure 2. a) Resistance vs. temperature of several thin films of LSCuO grown on STO(100) measured with the Van der Pauw configuration. b) Resistance vs. temperature of two twin samples 28 nm thick. The sample giving rise to the red curve has been annealed in vacuum at 550ºC for three hours in order to deoxygenate the film.

Figure 2 displays resistance vs. temperature measurements for several thin films. Figure 2a shows the resistance vs. temperature for a number of thicknesses, being all samples metallic down to the 10 nm thickness range, where films become insulating. In order to study the dependence of the transport properties on the oxygen content, two twin films (grown simultaneously) where measured under different conditions. One of them was annealed during three hours at 550ºC in a vacuum chamber, while the other was not. Figure 2b shows the resistance vs. temperature characteristics of both samples. The film annealed in vacuum exhibits a significantly higher resistance for the whole temperature range and becomes insulating below 100K. This finding suggests that our material is a hole doped semiconductor [15], and the electron doping induced by the creation of oxygen vacancies suppresses the hole conductivity.

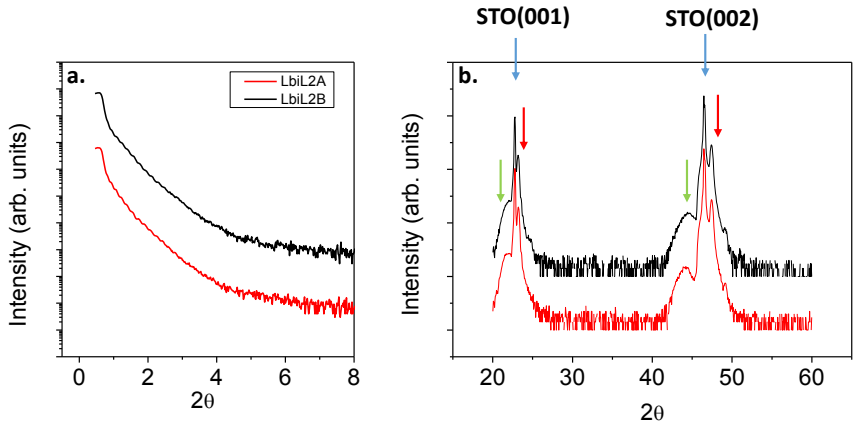

Figure 3. (a) XRR pattern of two $LSMO_{25nm}$/ BTO_{4nm}/ $LSCuO_{2nm}$/ $LSMO_{10nm}$ heterostructures grown in the same conditions but different positions in the chamber. Small peaks indicating the total thickness are present, although the signal dies upon 4º. (b) XRD patterns of the same samples. Blue arrows indicate the STO(001) substrate peaks, red and green indicate the peaks of the LSMO and BTO respectively.

The structural characterization of MFTJ samples, including an ultrathin LSCuO layer, are shown in Figure 3. Figure 3a shows the x-ray reflectivity of a $LSMO_{25nm}$/ BTO_{4nm}/ $LSCuO_{2nm}$/ $LSMO_{10nm}$ heterostructure. The finite size fringes allow determining the total thickness of the sample. They only reach the $2\theta=5^{o}$ range, suggesting a small degree of surface roughness. X-ray diffraction patterns in Figure 3c show the texture and epitaxy of the films. The peaks of the STO(100) substrate are indicated by the blue arrows, while the peaks which correspond to the *c*-axis of the LSMO and BTO films are indicated by red and green arrows, respectively. The XRD diffraction pattern allows extracting the *c* parameter average value for LSMO and BTO. The bulk STO lattice parameter is 3.905 Å, while the LSMO lattice parameter is a=3.876 Å. The BTO lattice parameters in bulk are a=3.992 Å and c=4.036 Å. These values would in principle suggest a compressive in-plane strain for BTO films grown on STO. On the other hand, the in-plane strain state would be expected to be expansive for LSMO. The green peak in the XRD pattern of Figure 3b shows an enlarged out-of-plane parameter for BTO of c=4.08 Å, while for the LSMO the red peak shows a compressed out-of-plane parameter of c=3.83 Å.

In order to study the properties of the interfaces of our system, STEM-EELS techniques have been used. Aberration-corrected STEM Z-contrast images were obtained using a Nion UltraSTEM200 equipped with a 5th-order corrector and a Gatan Enfinium electron energy-loss spectrometer (EELS) operated at 200 kV at Oak Ridge National Laboratory on cross section samples prepared by conventional mechanical grinding and polishing and Ar ion milling as described in chapter 2 [29]. The probe forming aperture was approximately 30 mrad and the EELS collection semi-angle was 33 mrad. Random noise in the EEL spectrum images was removed using principal-component analysis [32].

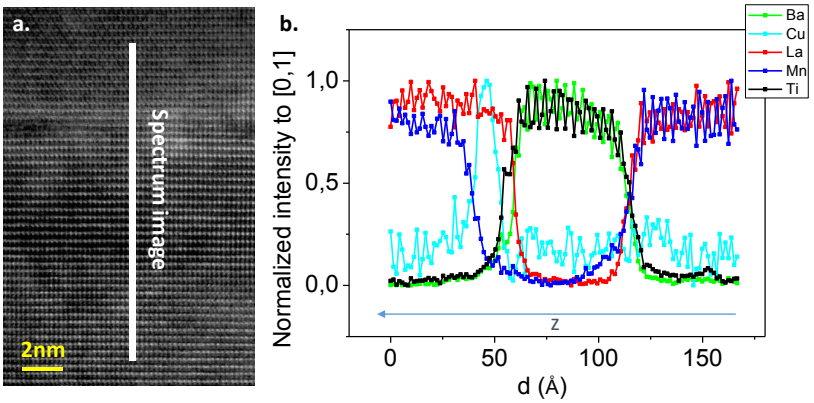

Figure 4. EELS line-scan along with Ba, Cu, La, Mn and Ti signals of a $LSMO_{12nm}$/ BTO_{6nm}/ $LSCuO_{2nm}$/ $LSMO_{15nm}$ heterostructure (a) HAADF atomic resolution image showing the area of the scan (yellow line). (b) EELS data, showing the integrated, normalized signals below the Ti $L_{2,3}$, Mn $L_{2,3}$, La $M_{4,5}$, Cu $L_{2,3}$ and Ba $M_{4,5}$ edges acquired with a beam current of 13 pA and an exposure time of 1s per pixel.

Figure 4 shows an EELS line-scan of a $LSMO_{12nm}$/ BTO_{6nm}/ $LSCuO_{2nm}$/ $LSMO_{15nm}$ heterostructure. The relative offsets between different signals allow determining the interface atomic plane stacking sequence. We find that the BTO interfaces are symmetric, being both the bottom LSMO/BTO and the top BTO/LSCuO interfaces LaO/TiO_2 terminated. The upper LSCuO/LSMO interface sequence has not been determined due the poor signal measured from the high energy lying Sr $L_{2,3}$ edge.

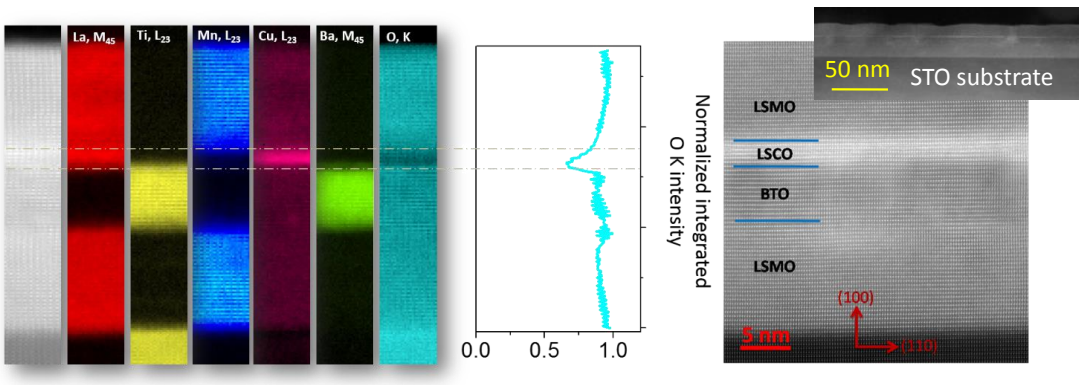

Figure 5. (a) Simultaneous Z-contrast signal (left) and chemical maps obtained from an EEL spectrum image of a magnetic tunnel junction of $LSMO_{12nm}$/ BTO_{6nm}/ $LSCuO_{2nm}$/ $LSMO_{15nm}$ grown on STO(100). (b) Normalized integrated O *K* signal. Dashed lines mark the interfaces of the cuprate layer. (c) HAADF image of the heterostructure.

Figure 5 displays a set of compositional maps derived from an electron energy-loss spectrum image of a $LSMO_{12nm}$/ BTO_{6nm}/ $LSCuO_{2nm}$/ $LSMO_{15nm}$ heterostructure grown on STO(100). Figure 5a shows the simultaneous annular dark field image (left end) across the heterostructure along with the chemical maps for La $M_{4,5}$ (red), Ti $L_{2,3}$ (yellow), Mn $L_{2,3}$ (blue), Cu $L_{2,3}$ (magenta), Ba $M_{4,5}$ (green) and O *K* (cyan) edges. The junctions exhibits abrupt interfaces, and the termination planes, again, between LSMO and BTO and between BTO and LSCuO are LaO/TiO_2 and TiO_2/LaO, respectively. In Figure 5b, the averaged normalized intensity of the O *K* edge is presented. The grey dashed lines depict the cuprate interfaces. A sharp dip (near 20%) is observed in the O *K* normalized intensity, suggesting that the LSCuO layer stores a very large amount of oxygen vacancies.

Figure 5c shows a HAADF image of the same sample and a low magnification HAADF image (top). The film is epitaxial and interfaces are coherent. In order to disregard artifacts, the O *K* edge signal obtained after the background subtraction has been normalized by the incoming beam intensity, I_0. The value of I_0 has been estimated by integrating a wide background window before the edge onset, in order to avoid the effect of Rutherford scattering at higher angles in LSCuO. No signs of major defects, changes in the crystallinity or secondary phases are detected.

5. Transport measurements in LSMO/ BTO/ LSCuO/ LSMO MFTJ's

To define the MFTJ's the same optical lithography of patterning have been used as in chapter 3. Perpendicular transport has been measured in rectangle shaped pillars of 9x18 μm^2 and 5x10 μm^2. Magnetic fields were applied along the easy axis of the LSMO ([110] direction) were swept between -4000 and 4000 Oe.

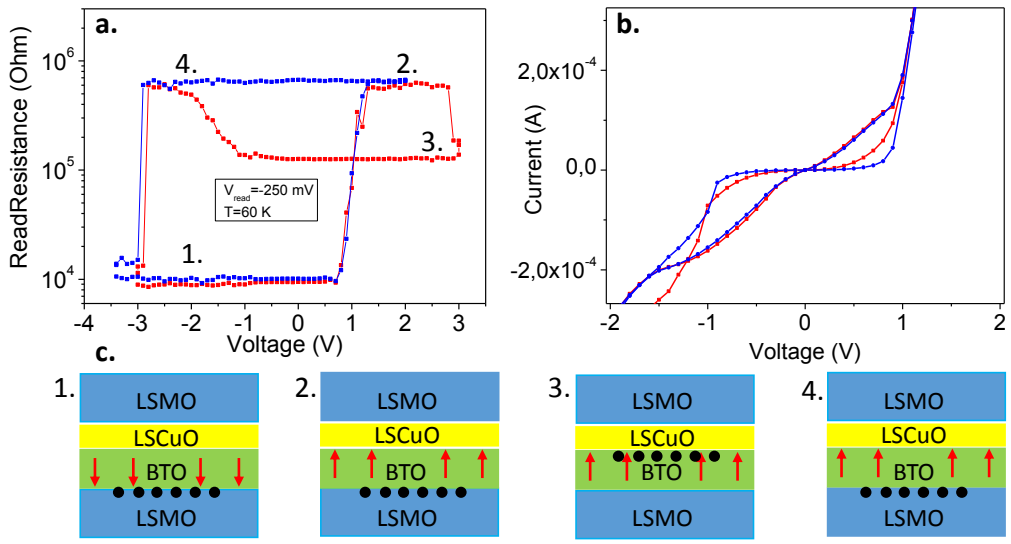

Figure 6. (a) Read resistance versus writing voltage for a MFTJ of 5x10μm^2 at 60 K and a read voltage of -250 mV. Two different cycles are shown. (b) IV curves for both cycles. (c) Schematic of the proposed polarization state along with position of oxygen vacancies in the heterostructure. The direction of polarization is indicated with red arrows while the O vacancies are indicated with black filled circles.

Figure 6 displays two different resistance switches at 60K for a 5x10 μm^2 junction of $LSMO_{10nm}$/ BTO_{4nm}/ $LSCuO_{2nm}$/ $LSMO_{10nm}$. Figure 6a shows the resistance reading with a voltage of -250 mV vs. the writing voltage. The tunnel electroresistance (TER) for both cases is of 10^4 %. Such enhancement results from the introduction of the LSCuO ultrathin layer in between the BTO barrier and the top LSMO electrode. The blue polarization cycle goes from -3 V to 2V, while the red one reaches values of 3V. We will refer to the initial state as level 1 for both cycles (see schematic in Figure 6c for clarity). The electronic asymmetry does not result from the different screening lengths at both sides of the interface, as recently discussed by Zhulaev et al [33] . Instead, it is triggered by the generation and accumulation of oxygen vacancies either towards the botttom or the top BTO interface. Under strong electric fields pointing downwards, oxygen vacancies leak from the cuprate into the BTO. This behavior can be tracked by a strong decrease of the device resistance, which results from the effective reduction of the width of the tunneling barrier (which does not include the LSCuO layer). Level 1 of Figure 6a

corresponds to polarization pointing downwards and oxygen vacancies accumulating near the bottom BTO interface. As the electric field is increased, polarization eventually switches and a change in the resistance state is detected as an abrupt increase to state 2 at 0.8 V (for both red and blue cycles). Therefore, electroresistance results from the modulation of the effective barrier height by the ferroelectric polarization. When oxygen vacancies are accumulated near the bottom interface a Schottky barrier appears there. Polarization pointing down yields a reduction of the effective barrier height, and hence a resistance reduction, while polarization up leads to the opposite effect. If after reaching state 2 (polarization up, vacancies down) the electric field is further increased (see single red cycle) oxygen vacancies will eventually switch to the top interface (near 2.8 V), as shown in the schematic of Figure 6c as level 3. A reduction of resistance is observed now because polarization points towards the Schottky contact, which is now transferred to the top interface. This state, despite its lower resistance, is less favorable energetically (polarization pointing to the interface). If the electric field is now reversed, oxygen vacancies switch back to the bottom interface where they seem to accumulate preferentially, and we return to a state 4 (blue cycle) with oxygen vacancies down and polarization up, identical to state 2. By further reducing the electric field, the polarization will eventually switch to point downwards again. Figure 6b displays the IV curves measured simultaneously, where a clear change in the conduction process can be seen.

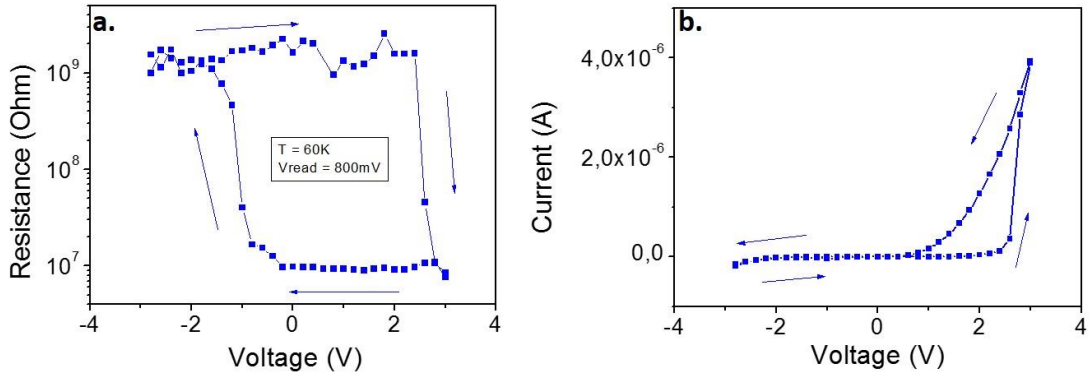

Figure 7. (a) Read resistance vs. writing voltage for a MFTJ of 5x10μm^2 with the LSCuO thin film between the LSMO bottom electrode and the BTO barrier. The growth sequence is the following: $LSMO_{25nm}$/ $LSCuO_{2nm}$ /$BTO_{4,4nm}$/$LSMO_{10nm}$ at 60 K and a read voltage of -800 mV. The initial voltage was -3 V, and the cycle is indicated by the arrows. (b) IV curves for the entire cycles.

In Figure 7 we show the measurements obtained on a structure where the LSCuO barrier is below the BTO layer, i.e, the stacking is ordered as follows: STO(100) substrate/ $LSMO_{25nm}$/ $LSCuO_{2nm}$/ $BTO_{4.4nm}$/ $LSMO_{10nm}$. Notice that in this geometry electric fields pointing down will not transfer any oxygen vacancies into the BTO layer. As described above, the accumulation of vacancies within the cuprate layer yields a large resistance due to hole compensation. This behavior results in an effective increase of the width of the tunneling barrier. On the other hand, polarization charges at the cuprate interface must now be screened by the compensating charges in a p-side space charge region, which develops in the ultrathin cuprate layer. Notice that now space charges are negative due to the p-type character of the cuprate in contact with the LSMO (which acts as the n-side).

When polarization points towards the LSCuO (down), positive polarization charges have to be compensated by negative space charge. This occurs by increasing the width of the space charge region, resulting in an increased effective barrier height and thus in a high resistance state. When the electric field is increased, and the polarization switches to point upwards, the polarization charges to be compensated at the cuprate contact are negative. This is now accomplished by a reduction of the width of the space charge region, that yields a reduction in barrier height and thus in a low resistance level. Notice finally that now the energetically favorable polarization

orientation is pointing towards the interface because it is compensated by a forward current flow (holes from the cuprate into the manganite).

Finally, the resistance level is several orders of magnitude higher than in the previous sample due to the increased resistance resulting from the accumulation of oxygen vacancies in the cuprate layer (the applied voltage for reading the resistance state is of 0.8 V). The application of electric fields pointing upwards activates transfer of oxygen vacancies from the cuprate (which lowers its resistance) into the BTO (which lowers the resistance further due to electron doping) and the resistance level is reduced by 5 or 6 orders of magnitude as shown in Figure 6a.

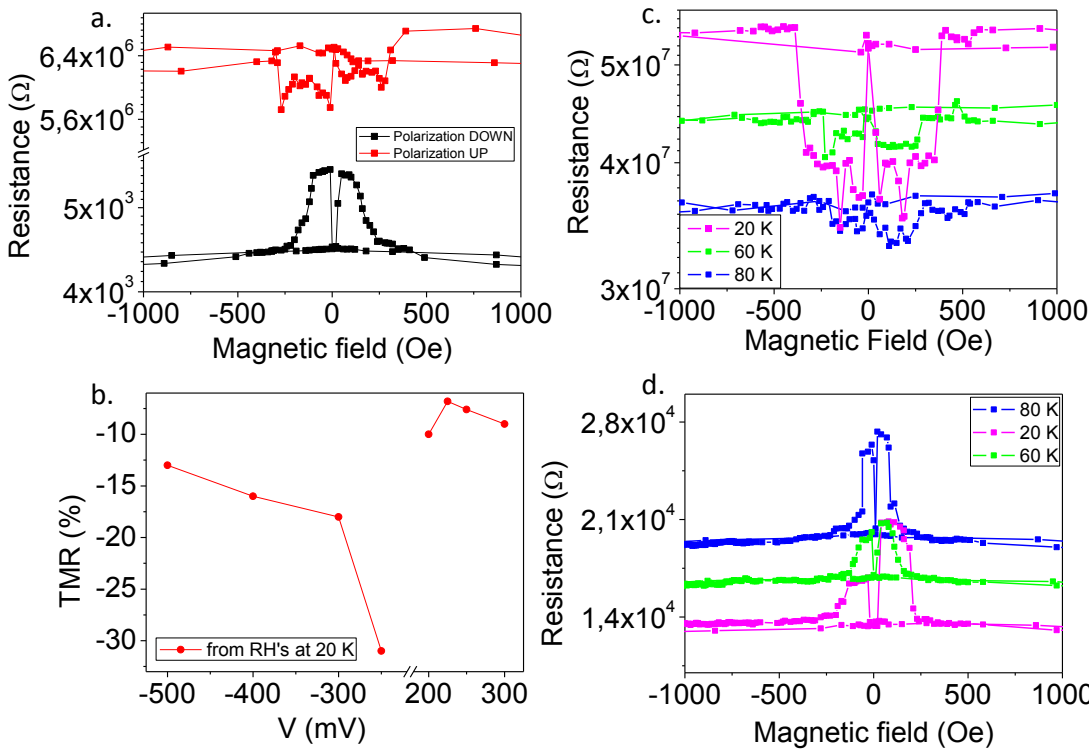

Figure 8. (a) Resistance vs. Magnetic field of a 5x5 μm^2 MFTJ of $LSMO_{25nm}$/ $BTO_{4.4nm}$/ $LSCuO_{2nm}$/ $LSMO_{10nm}$. Data taken at 40 K while applying a voltage of -500 mV. Red values correspond to the resistance for ferroelectric polarization pointing towards the LSCuO layer (up) and black values for polarization pointing towards the bottom LSMO electrode (down). (b) TMR vs. bias at 20 K for polarization up, calculated from RH curves. Points are connected using straight lines for clarity. (c) Resistance vs. magnetic field of the same junction for several temperatures and an applied voltage of -250mV. (d) Resistance vs. magnetic field of the same junction for several temperatures and an applied voltage of 200 mV for polarization down.

Figure 8 shows the resistance vs. magnetic field cycles of a MFTJ sized 5x10 μm^2. In Figure 8a two curves are displayed. Black (red) corresponds to polarization down (up) in a LSMO/BTO/LSCuO/LSMO junction. Interestingly, we have observed an inversion of the sign of the tunneling magnetoresistance for up polarization. Both curves are measured at 40 K and –0,5 V. Coercive fields are H_{c1} = 80 Oe and H_{c2} = 480 Oe in both cases and correspond to the bottom and the top electrode, respectively. The negative TMR is a highly anomalous feature in a symmetric tunnel junctions with highly spin polarized electrodes. Notice that the magnitude of the TMR is highly asymmetric with voltage and that it becomes very small when voltages are positive. This behavior has been previously described to originate at resonant transport through magnetic states at the interface which have a spin filtering effect.

An important detail to be discussed is the case of the coercive field H_{c2} for polarization down (Figure 8a), where the change in the resistance state is not abrupt (as it can be seen for smaller coercive fields). This effect can be appreciated in Figures 8 c,d, where three resistance vs. magnetic field curves for different temperatures at 0.2 V are shown. We find a two-step change of the relative magnetization, with coercive fields of 80 Oe (as expected for the LSMO bottom electrode), 150 Oe (expected for the top LSMO electrode) and 480 Oe. Other possible scenario is in terms of interfacially induced changes of magnetic anisotropy along with their effect on the tunneling probability through the tunneling anisotropy magnetoresistance phenomenon. I.e., by forcing the oxygen vacancies to pile up either against the top or the bottom interface in the BTO one may trigger a significant electron doping at the other side of the interface due to oxygen vacancy transfer. This charge transfer may affect the magnetism of the cuprate/manganite at the interface and eventually also its magnetic anisotropy.

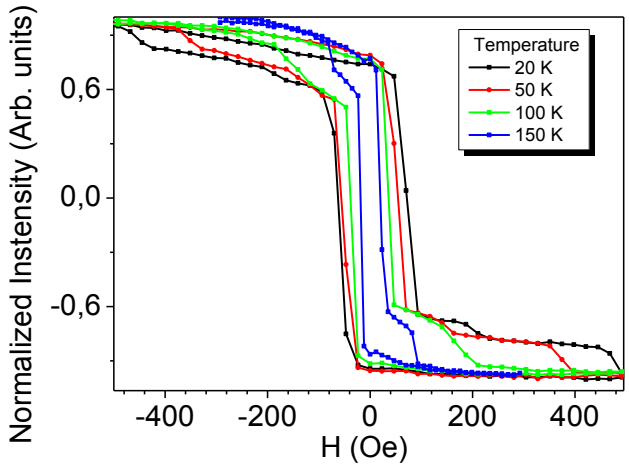

Figure 9. Magnetic hysteresis loops at the Mn-L_3 edge by X-ray magnetic scattering on a $LSMO_{10nm}$/ BTO_{4nm}/ $LSCuO_{2nm}$/ $LSMO_{3nm}$ sample. The magnetic field was applied along the (100) axis.

Indeed, preliminary results obtained at BESSY by using the ALICE chamber point in this direction. Figure 9 displays several hysteresis loops measured by means of X-ray magnetic scattering (XRMS) at the Mn L_3-edge for a $LSMO_{10nm}$/ BTO_{4nm}/ $LSCuO_{2nm}$/ $LSMO_{3nm}$ sample. Dashed lines indicate point the steps in the hysteresis loops. At least four different coercive fields can be seen at 20 K, which we interpret as an indication for the nucleation of different magnetic states at the LSMO interfaces when compared to those of the bulk of the LSMO layers. Further work will be necessary to assess the effect of polarization switching on these magnetic states.

6. Conclusions

We have fabricated a number of high quality $La_{0.7}Sr_{0.3}MnO_3$ /$BaTiO_3$ /$La_{0.86}Sr_{0.14}CuO_3$ /$La_{0.7}Sr_{0.3}MnO_3$ multiferroic tunnel junctions using a high O_2 pressure RF sputtering system. The STEM-EELS results show that the heterostructures are flat over long lateral distances and the ultrathin LSCuO layer also grows laterally continuous. The introduction of the LSCuO barrier results in a large enhancement of the TER effect by four orders of magnitude compared to symmetric LSMO/BTO/LSMO junctions. This enhancement is also accompanied by a change in the sign of TMR, which we interpret as a spin filter effect for the up polarization state of the barrier. This result is especially surprising for electrodes with positive spin polarization. The presence of a relatively high concentration of O vacancies contributes to the complexity of the physical properties measured. Indeed, the EELS data show a dip of the oxygen *K* edge overall intensity in the LSCuO layer, pointing to a large reduction of the local O content. Oxygen vacancies in the structure can explain the various resistance states found in the junctions. In addition, it has been observed that the conduction process is vacancy-mediated. In summary, we show that the mechanisms of ferroelectric polarization and oxygen vacancy migration through the barrier are coupled, and this result should be taken into account in the design of novel devices based on complex oxides.

7. References

[1] M.Y. Zhuravlev, S.S. Jaswal, E.Y. Tsymbal, R.F. Sabirianov, "Ferroelectric switch for spin injection", *Appl. Phys. Lett.* **87**, 1-3 (2005).

[2] J.P. Veev, C.G. Duan, J.D. Burton, A. Smogunov, M.K. Niranjan, E. Tosatti et al., "Magnetic tunnel junctions with ferroelectric barriers: Prediction of four resistance states from first principles", *Nano Lett.* **9,** 427–432 (2009).

[3] V. Garcia, M. Bibes, L. Bocher, S. Valencia, F. Kronast, a Crassous, et al., "Ferroelectric control of spin polarization", *Science* **327**, 1106 (2010).

[4] M. Hambe, A. Petraru, N.A. Pertsev, P. Munroe, V. Nagarajan, H. Kohlstedt, "Crossing an interface: Ferroelectric control of tunnel currents in magnetic complex oxide heterostructures", *Adv. Funct. Mater.* **20**, 2436-2441 (2010).

[5] Y.W. Yin, M. Raju, W.J. Hu, X.J. Weng, X.G. Li, Q. Li, "Coexistence of tunneling magnetoresistance and electroresistance at room temperature in $La_{0.7}Sr_{0.3}MnO_3$/(Ba, Sr)TiO_3/ $La_{0.7}Sr_{0.3}MnO_3$ multiferroic tunnel junctions", *J. Appl. Phys.* **109**, 3-6(2011).

[6] D. Pantel, S. Goetze, D. Hesse, M. Alexe, "Reversible electrical switching of spin polarization in multiferroic tunnel junctions", *Nat. Mater.* **11**, 289-293 (2012).

[7] Y.W. Yin, J.D. Burton, Y.-M. Kim, a Y. Borisevich, S.J. Pennycook, S.M. Yang et al., "Enhanced tunnelling electroresistance effect due to a ferroelectrically induced phase transition at a magnetic complex oxide interface", *Nat. Mater.* **12**, 397-402 (2013).

[8] X. Liu, J.D. Burton, E.Y. Tsymbal,"Enhanced Tunneling Electroresistance in Ferroelectric Tunnel Junctions due to the Reversible Metallization of the Barrier", *Phys. Rev. Lett.* **116,** 197602 (2016).

[9] Z. Wen, C. Li, D. Wu, A. Li, N. Ming, "Ferroelectric-field-effect-enhanced electroresistance in metal/ferroelectric/semiconductor tunnel junctions", *Nat Mater.* **12**, 617-621 (2013).

[10] A. Sawa, "Resistive switching in Rapid advances in transition metal oxides", *Mater. Today.* **11**, 28-36 (2008).

[11] V. Garcia, S. Fusil, K. Bouzehouane, S. Enouz-Vedrenne, N.D. Mathur, a Barthélémy and M. Bibes, "Giant tunnel electroresistance for non-destructive readout of ferroelectric states", *Nature* **460**, 81-84 (2009).

[12] A. Gruverman, D. Wu, H. Lu, Y. Wang, H.W. Jang, C.M. Folkman, M. Ye. Zhuravlev, D. Felker, M. Rzchowski, C.C. Eom and E. Y. Tsymbal, "Tunneling electroresistance effect in ferroelectric tunnel junctions at the nanoscale", *Nano Lett.* **9**, 3539-3543 (2009).

[13] P. Maksymovych, S. Jesse, P. Yu, R. Ramesh, A.P. Baddorf, S. V Kalinin, "Polarization Control of Electron Tunneling into Ferroelectric Surfaces", *Science* **324**, 1421-1425 (2009).

[14] A. Chanthbouala, V. Garcia, R.O. Cherifi, K. Bouzehouane, S. Fusil, X. Moya, S. Xavier, H. Yamada, C. Deranlot, N. D. Mathur, M. Bibes, A. Barthélémy and J. Grollier, "A ferroelectric memristor", *Nat Mater.* **11**, 860-864 (2012).

[15] H.-C. Yu, K.-Z. Fung, "Role of Sr Addition on the Structure Stability and Electrical Conductivity of Sr-Doped Lanthanum Copper Oxide Perovskites", *J. Mater. Res.* **19**, 934-949 (2004).

[16] M.T. Czyyk, G.A. Sawatzky, "Local-density functional and on-site correlations: The electronic structure of La_2CuO_4 and $LaCuO_3$", *Phys. Rev. B.* **49,** 14211 (1994).

[17]J.F. Bringley, B. a. Scott, S.J. La Placa, R.F. Boehme, T.M. Shaw, M.W. McElfresh, S.S Trail and D.E. Cox, "Synthesis of the defect perovskite series $LaCu0_{3-\delta}$ with copper valence varying from 2+ to 3+", *Nature* **347**, 263- 265 (1990).

[18]J.F. Bringley, B.A. Scott, S.J. La Placa, T.R. McGuire, F. Mehran, M.W. McElfresh and D. E. Cox, "Structure and properties of the $LaCuO_{3-x}$ perovskites", *Phys. Rev. B.* **47**, 15269-15275 (1993).

[19]T. Siegrist, S.M. Zahurak, D.W. Murphy, R.S. Roth, "The parent structure of the layered high-temperature superconductors", *Nature* **334**, 231-232 (1988).

[20]J.J. Wang, F.Y. Meng, X.Q. Ma, M.X. Xu, L.Q. Chen, Lattice, "Elastic polarization and electrostrictive properties of $BaTiO_3$ from first-principles", *J. Appl. Phys.* **108** (2010).

[21]K.J. Choi et al., "Enhancement of Ferroelectricity in Strained BaTiO3 Thin Films", *Science* **306**, 1005-1009 (2004).

[22]J. Junquera, P. Ghosez, "Critical thickness for ferroelectricity in perovskite ultrathin films", *Nature* **422**, 506-509 (2003).

[23]N. Sai, A.M. Kolpak, A.M. Rappe, "Ferroelectricity in ultrathin perovskite films", *Phys. Rev. B* **72**, 1-4 (2005).

[24]R. Nakao, K. Ishizumi, I. Takahashi, H. Terahuchi, Y. Hayafuji, K. Miura, "Critical thickness for ferroelectricity of $BaTiO_3$ by first-principles calculations", *Appl. Phys. Lett.* **86** (2005).

[25]G. Gerra, A.K. Tagantsev, N. Setter, K. Parlinski, "Ionic polarizability of conductive metal oxides and critical thickness for ferroelectricity in $BaTiO_3$", *Phys. Rev. Lett.* **96**, 1-4 (2006).

[26]X.M. Ge, S.H. Chan, Q.L. Liu, Q. Sun, "Solid oxide fuel cell anode materials for direct hydrocarbon utilization", *Adv. Energy Mater.* **2** 1156–1181 (2012).

[27]Y. Liu, X. Lou, M. Bibes, B. Dkhil, "Effect of a built-in electric field in asymmetric ferroelectric tunnel junctions", *Phys. Rev. B.* **88**, 1-9 (2013).

[28]T. Kolodiazhnyi, M. Tachibana, H. Kawaji, J. Hwang, E. Takayama-Muromachi, "Persistence of ferroelectricity in $BaTiO_3$ through the insulator-metal transition", *Phys. Rev. Lett.* **104**, 1-4 (2010).

[29]D. Muller, L.F. Kourkoutis, M. Murfitt, J.H. Song, H.Y. Hwang, J. Silcox, N. Delby and O.L. Krivanek, "Atomic-scale chemical imaging of composition and bonding by aberration-corrected microscopy", *Science* **319**, 1073 (2008).

[30]X.Y. Wang, Y.L. Wang, R.J. Yang, "Lattice model for strained nanoscale ferroelectric capacitors: Investigation on fundamental size limits in ferroelectricity", *Appl. Phys. Lett.* **95**, 142910 (2009).

[31]M. Varela, Z. Sefrioui, D. Arias, M. Navacerrada, M. Lucía, M. López de la Torre, et al., "Intracell Changes in Epitaxially Strained $YBa_2Cu_3O_{7-x}$ Ultrathin Layers in $YBa_2Cu_3O_{7-x}/PrBa_2Cu_3O_7$ Superlattices", *Phys. Rev. Lett.* **83**, 3936-3939 (1999).

[32]M. Bosman, M. Watanabe, D.T.L. Alexander, V.J. Keast, "Mapping chemical and bonding information using multivariate analysis of electron energy-loss spectrum images", *Ultramicroscopy* **106,** 1024–32 (2006).

[33]M.Y. Zhuravlev, R.F. Sabirianov, S.S. Jaswal, E.Y. Tsymbal, "Giant electroresistance in ferroelectric tunnel junctions", *Phys. Rev. Lett.* **94**, 1-4 (2005).

Chapter 5: Interfacially enhanced conductivity in YSZ thin films.

The search of novel materials with enhanced ionic conductivity for their application in energy devices constitutes an exciting direction in the expanding field of oxide interfaces [1]. In particular, exploiting size effects in ion conducting materials by the controlled reduction of ion conducting sample dimensions down to the nanoscale holds the promise to yield large improvements in the performance of oxides based devices for energy generation and storage [1-3]. Enhancements of oxide-ion conductivity at interfaces could be relevant towards lowering the operation temperature of solid oxide fuel cells (SOFC) (usually 800-1000ºC), which imposes serious restrictions on materials selection due to thermal stress or fatige [1]. In recent years, a number of works have reported enhanced ion conductivities at strained or textured epitaxial heterostructures involving yttria-stabilized zirconia, ZrO_2:Y_2O_3 (YSZ), and a non-conducting insulator [4-14] when the thickness of the ion conducting layer is reduced to the 10–20 nm range. Furthermore, Garcia-Barriocanal et al. [10] have reported a colossal conductivity enhancement in multilayers combining $SrTiO_3$ (STO) and highly strained ultrathin YSZ layers with thicknesses of the order of a unit cell level (< 1 nm). The result was discussed in terms of an interface oxygen disordered plane resulting from the matching of perovskite and fluorite structures combined with the huge 7% epitaxial strain imposed by the STO [10, 15]. Other routes to improve oxygen diffusivities may rely on the growth of single-domain oxide interfaces with crystal symmetry discontinuity, i.e., the combination of dissimilar symmetries at the interfacial planes, which imply exploiting different substrate orientations (hence, different degrees of strain). An example can be found in the work of M. Scigaj et al. [16]. They showed that YSZ can grow epitaxially on STO (110) in a layer-by-layer mode, with RHEED oscillations up to thickness values above 15 nm, thus demonstrating that high quality single-domain YSZ(001)/STO(110) oxide interfaces with symmetry discontinuity can be achieved. These results pave new avenues towards exploiting the effects of symmetry discontinuity in the search of enhanced ionic conductivities. However, several questions remain open such as deconvolving the effects of actual strains or substrate or electronic contributions to the conductivity.

In this work we will focus on fluorite/perovskite interfaces with negligible amounts of epitaxial mismatch (in the <1% range) in order to study the interfacial contribution to the conductivity in the absence of large amounts of mismatch strain. Thin films (2 to 87 nm thick) of ZrO_2:Y_2O_3 (YSZ) with (111) crystalline orientation have been epitaxially grown on top of insulating $YAlO_3$ substrates (101). As we will show, this system remains epitaxial with no signs of strain relaxation up to a layer thickness of 80 nm. We have found a large conductivity enhancement in these virtually unstrained epitaxial YSZ ultrathin films. Interestingly, the dc conductivity of the thin films shows an increase of up to five orders of magnitude at 333K with respect to the bulk material, together with a decrease in the activation energy down to the 0.7 eV range. These findings will be discussed in terms of enhanced carrier density and mobility. In particular, the effects of the structural mismatch of the oxygen sublattices of both structures, associated with their dissimilarity, will be discussed as likely sources of the enhanced conductivity values measured.

1. YSZ thin films

YSZ is an ionic conductor of oxygen ions with a fluorite-like structure. O vacancies are introduced by the aliovalent substitution of Zr by Y, since the substitution of Zr 4+ by Y 3+ needs of the introduction of one oxygen vacancy every two Y atoms for charge neutrality to be preserved. Y doping results in the stabilization at room temperature of a fluorite cubic structure, as shown in Figure 1, in where O atoms occupy the tetrahedral positions of the cubic unit cell.

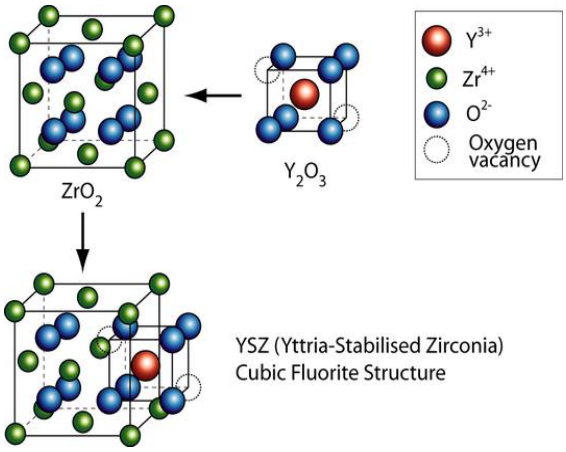

Figure 1. Unit cell of YSZ. Figure adapted from reference [10].

For the present experiment, a series of thin films (with thicknesses ranging from 2 to 87 nm) of YSZ with (111) crystalline orientation were epitaxially grown on top of $YAlO_3$ (YAP) (110) substrates by high pure oxygen pressure RF sputtering technique at 900 °C. In-situ annealings followed in 900 mbar O_2 pressure at 700 °C. The crystalline structure of $YAlO_3$ (YAP) is orthorhombic with lattice parameters a=5.179 Å, b=5.326 Å, c=7.369 Å [17]. On the other hand, in YSZ the fluorite lattice parameter is a=5.14 Å. Despite the difference between the lattice parameters of both materials, the distances between nearest neighbor cations are quite similar: pseudocubic lattice parameters of YAP are a'=3.66 Å, b'=3.76 Å and c'=3.68 Å, while the lattice parameter of the FCC YSZ Zr sublattice is d = 3.63 Å. These parameters allow good epitaxial growth. Figure 2a displays a set of X-ray diffraction spectra of the YSZ thin films grown on YAP (110) substrates with thicknesses from 2 to 87 nm. All of them show a main peak at 34.26° corresponding to the YAP (110) substrate orientation, while the 30° peak corresponds to the YSZ (111) oriented film. The large number of finite size satellites around the YSZ(111) peaks in the diffraction spectra of Figure 2a indicate the high quality and smoothness of the films. Figure 2b shows the reflectivity spectra of the same set of samples. These values are close to the bulk ones, pointing to a limited amount of strain in the films. A low substrate interface roughness is also evidenced by the large number of thickness fringes. The AFM image of the 2 nm thick YSZ film shown in Figure 2c displays one unit cell high substrate terraces over micron size areas, indicating a two dimensional growth mode.

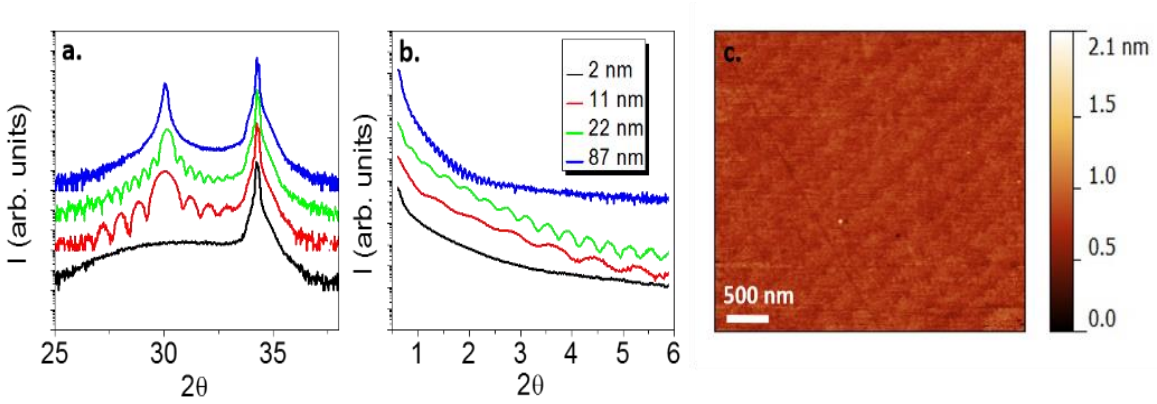

Figure 2. (a) X-ray diffraction patterns of several YSZ(111) thin films showing the epitaxial growth on YAP(110) substrates. (b) X-ray reflectivity of the same samples shown in (a). (c) AFM topography image of an ultrathin film 2 nm thick, exhibiting very smooth surfaces.

2. Impedance spectroscopy on thin films

2.1. Measurements in N_2 atmosphere

The electrical response of the samples has been analyzed by dielectric spectroscopy. Two contacts in planar geometry of 5 x 2,4mm^2 separated a distance of 0.1 mmwere fabricated by evaporating Ag on the film surface. Measurements were conducted while cooling down after heating the sample above 280 °C.

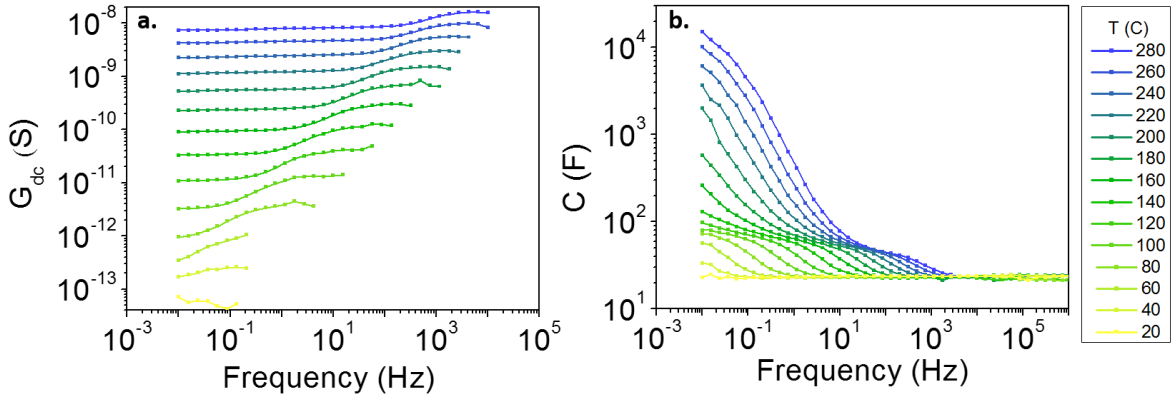

Figure 3. (a) Conductance vs. frequency of a 11nm YSZ thin film measured for several temperatures, in logarithmic scale. **(**b) Capacitance vs. frequency of the same sample measured for the same several temperatures, in logarithmic scale.

Figures 3a and 3b display the conductance and capacitance measurements of an 11 nm thick YSZ thin film for several temperatures. Both graphs show the presence of two different plateaus, which may reveal the presence of two different types of carriers involved in the conduction process. The dc conductance values were obtained from the low frequency plateaus for the Arrhenius plots. The conductivity decrease observed at low frequencies and high temperatures, along with the strong increase of the capacitance at low frequencies, suggest the possibility of an ionic contribution to the total conductance. On the other hand, the existence of a well defined conductance plateau down to the lowest frequencies is an indication of an electronic contribution to the total conductance.

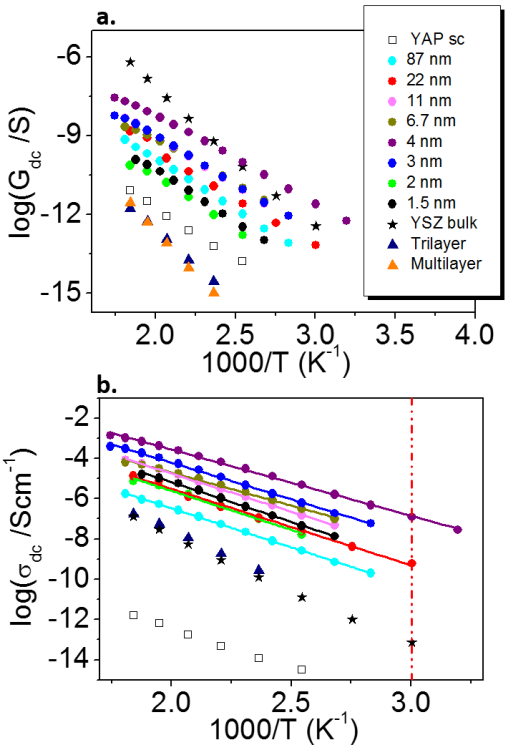

Figure 4. (a) Temperature dependence of the conductance for different YSZ thin films (filled circles), a YAP single crystal (empty squares), YSZ bulk (stars), a tri-layer made of amorphous YAP/polycrystalline YSZ/amorphous YAP (blue triangles) and a (YSZ_{2nm}/YAP_{10nm})x6 multilayer (orange triangles). (b) Temperature dependence of conductivity for the same samples. The Arrhenius plots correspond to YSZ thin films.

Figure 4a shows the temperature dependence of the dc conductance of a series of YSZ single layers of different thicknesses. A sharp enhancement is observed when thickness is increased above two unit cells, reaching a maximum value for 4 nm. From that thickness on, the conductance decreases slightly and then saturates above 20 nm. Notice that the conductance of the YSZ thin films is two to three orders of magnitude higher than that of the bare YAP substrates, which are highly insulating. The temperature dependence of the conductivity (obtained from the conductance measurements) is presented in Figure 4b for the YSZ layers. An enhancement of up to 5 orders of magnitude is observed near room temperature (333K) when compared to bulk single crystals (also shown in the figure). This conductivity enhancement is associated with both a decrease in the activation energy, from 1 eV in the YSZ single crystal to 0.7 ± 0.02 eV in the films, and to an increase of the pre-exponential factor of about one order of magnitude for the samples with the largest conductivity enhancement. This finding reflects an improved mobility landscape at the interface and possibly an increase of the carrier density. The high temperature extrapolation of the conductivity is a rough upper limit of the carrier density due to the effect of disorder and ion-ion correlations, which affect the low temperature conductivity.

2.2. Measurements in oxygen atmosphere

As the conductance measurements in a N_2 atmosphere indicate the possible presence of two kinds of carriers, another set of measurements have been carried out in a dry air atmosphere. For a purely ionic conductivity, the conductance should essentially be independent of the atmosphere oxygen partial pressure. However, as we show next, in our samples the atmosphere oxygen content strongly affects the conductance values. In Figure 5, three Arrhenius plots of a 4 nm thick YSZ film are presented.

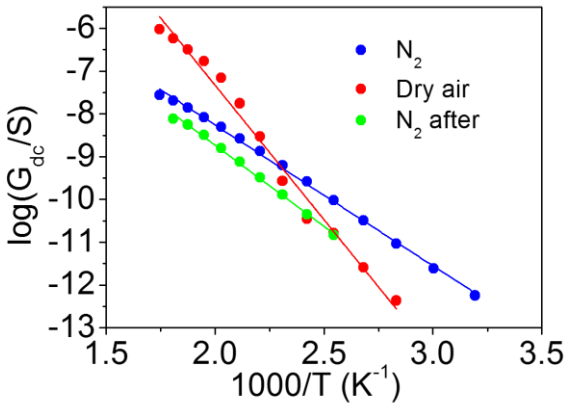

Figure 5. Arrhenius plot of a 4 nm YSZ thin film measured in different conditions. Blue dots stand for measurements carried out in a N_2 atmosphere, red dots correspond to air atmosphere while the green data were obtained in N_2 again after all measurements. The lines correspond to linear fits of the experimental results.

First, measurements have been obtained in a N_2 atmosphere (blue circles). Then, another set of measurements was carried out under a dry air atmosphere (red circles). Last, in order to evaluate irreversible sample degradation (if any), a measurement under a N_2 atmosphere was performed again (green circles). The green and blue curves show essentially the same activation energy (as can be seen from the slope of the fits), disregarding any irreversibility effects. On the other hand, the red dataset exhibits a quite different behavior. This finding suggests that a redox reaction dependent on the atmosphere may take place at the surface of the samples and influences strongly the conduction process. This result, in addition to the measurements mentioned in Figures 4a and 4b, indicates the presence of carriers of electronic character. However, their nature (whether they are of *p* or *n character)* remains still unclear. Further work including a study under a controlled partial pressure of oxygen should be done in order to clarify this issue, but here we set off to analyze the enhancement of the conductivity itself. This enhancement appears to take place within the first four nm of the films. Hence, in what follows we will focus on understanding if it is in any way related to any interfacial features using techniques that can probe the structure with atomic resolution.

3. Interfacial strain characterization by X-ray diffraction and STEM-EELS

3.1. Reciprocal space maps (RSM)

To visualize the interface structure, we have studied our YSZ thin films grown on (110) YAP substrates by means of X-ray diffraction using grazing incidence. Synchrotron reciprocal space maps (RSM) and reciprocal space and azimuthal scan with X-rays of λ=0.62 Å have been carried out at the beamline BM25B of the European Synchrotron Radiation Facility.

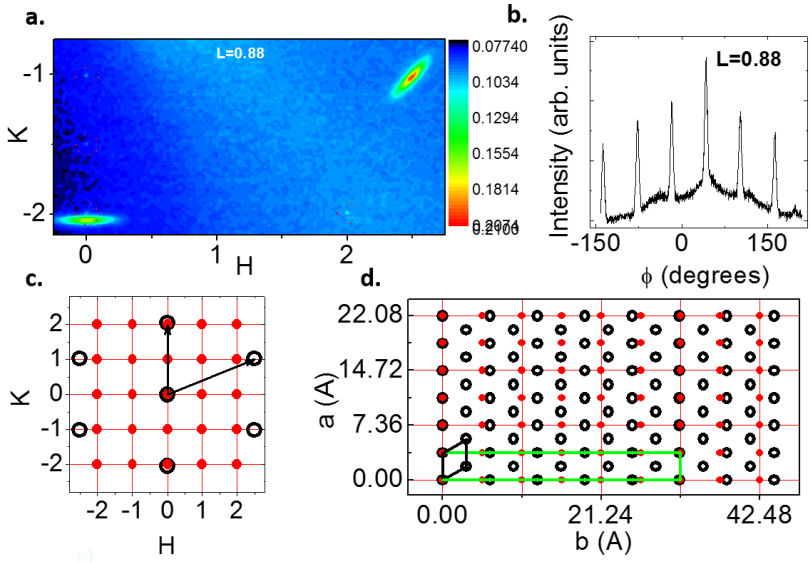

Figure 6. (a) In-plane RSM of the YSZ thin film obtained for L=0.88. Note that the highlighted red dashed circles are the tails of the maxima corresponding to the substrate. (b) Azimuthal scan of the in plane YSZ thin films, where the hexagonal symmetry is revealed. **(**c) Representation of the reciprocal space lattice of the YSZ thin film (black open dots) and the YAP substrate (red solid dots) obtained from RSM and azimuthal scans. (d) Representation of the real space unit cell of both the YSZ thin film and the YAP substrate using the same color code than in (a).

Figure 6 shows the HK RSM measured at L=0.88, which corresponds to the RS of the YSZ (note that HKL corresponds to the RS units of the YAP substrate calculated after the refinement of the single crystal). Two broad maxima corresponding to the YSZ thin film, with an evident hexagonal symmetry, can be observed along with sharper but less intense maxima associated with the YAP substrate (highlighted with red dashed circles in Figure 6a). We have further probed the hexagonal symmetry of the YSZ thin film by measuring an azimuthal scan of the YSZ crystal that can be observed in Figure 6b. The in-plane hexagonal symmetry of the YSZ lattice is revealed with the appearance of peaks rotated 60 degrees when the sample is scanned in the surface plane. Interestingly, the RSM of the YSZ also reveals the good match of the YAP and YSZ lattices in the H direction. However, along the K axis we observe a misfit between the maxima of the substrate and the thin film. Hence, the epitaxy results from the matching of the (111) YSZ and (110) YAP planes with triangular symmetry: the YSZ (111) plane is hexagonal, with a lattice parameter of 3.63 Å while the YAP (110) distorted square plane has 3.68 Å and 5.31 Å in-plane lattice parameters (corresponding to *c'* and $a\sqrt{2}$) axes in the pseudocubic notation). Both planes are superimposed in Figures 6c and 6d, where a suggested matching is presented. Zr atoms

are shown as black open dots, while Y and Al atoms are presented in red. Along the *a* direction, Zr atoms match the vertical Al or Y positions with a minimum distortion for the center column of atoms. However, the large mismatch of 16 % in the perpendicular direction hinders an atom-on-atom coincidence of both lattices. Still, some commensurability can be found in the system in the form of a matching of the atomic columns every five YSZ unit cells, giving rise to a form of linear-domain matching epitaxy.

3.2. STEM-EELS

In order to further investigate the origin of the enhanced conductivity observed in our experiment, we have carried out a number of atomic resolution STEM-EELS studies in our samples. The conductivity enhancement observed in Figure 4 might be ascribed to the structural incompatibility of the oxygen sublattices (oxygen occupies tetrahedral positions in the fluorite versus octahedral positions in the perovskite). This mismatch can result in a varying oxygen content along the interface which may affect both carrier density and mobility. In order to gain more insights into the interface structural features, a study of the strain along the growth direction along with an analysis of the O *K* edge EELS fine structure have been performed.

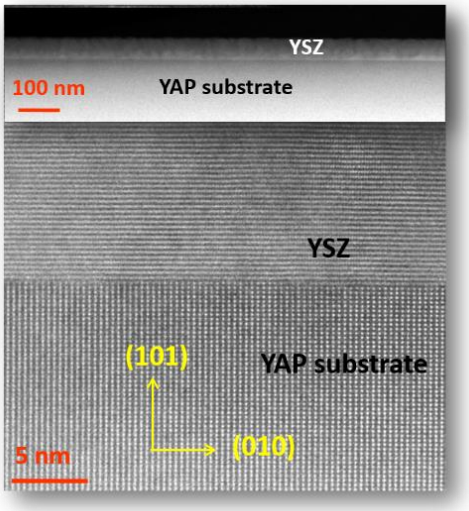

Figure 7. Z-contrast STEM image of a 50 nm thick YSZ thin film. The yellow arrows show the orientation of the substrate. (top) Low magnification image of the thin film.

Aberration corrected STEM images of cross-sectional samples confirm the high structural quality of the layers and the sharpness of the interfaces. Figure 7 displays both low and high magnification high-angle annular dark field (HAADF) images of the 50 nm thick YSZ thin film on YAP (110). Low magnification images (top) show that the film is flat over long lateral distances (over several hundreds of nanometers), in good agreement with XRD. Good epitaxy is observed up to large thickness values without major signs of strain relaxation or island growth, which again highlights the reduced effects of epitaxial strain.

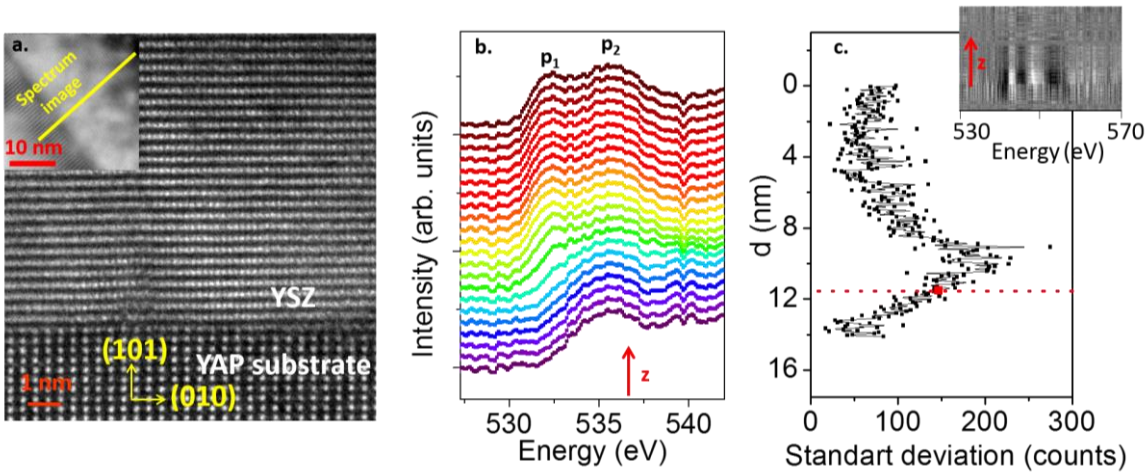

Figure 8. (a) Z-contrast STEM images of a 50 nm YSZ thin film. The HAADF image inset on the left shows the region where a line scan has been taken, indicated by the yellow line. (b) O *K* edge spectra (normalized and displaced vertically for clarity) extracted from the line scan measured while raster scanning the beam across the interface plane (ten adjacent spectra have been averaged to produce each one of these curves). The three violet curves at the bottom correspond to the YAP substrate, while the spectra from blue to yellow correspond to the interface and first planes of YSZ. The spectra at the top, from orange to red, correspond to the bulk-like region of the YSZ film, away from the interface. (c) Standard deviation of the absolute value of the residual signal obtained after carrying out a MLLS fit of the EELS linescan using the bottom and top spectra in (b) as references. The inset shows the residual signal of the MLLS fit for the fit region.

Figure 8a displays a pair of HAADF images of the 50 nm YSZ thin film on YAP (101). Figure 8b shows a set of EELS O *K* edges measured while scanning the beam across the interface, extracted from a line scan (averaged, normalized and displaced vertically, for clarity). The line scan was acquired using an energy dispersion of 0.25 eV/channel and an exposure time of 0.5 s/pixel, with a beam current of tens of pA. Random noise was reduced using principal component analysis (PCA, see Chapter 2). The violet-purple colored spectra at the bottom correspond to the substrate, while the blue spectra come from the interface area. Data from the cyan to the yellow curves correspond to the first 5 nm of the YSZ thin film. In this region, a clearly different fine structure of the O *K* edge is observed. The red signals at the top end correspond to the top of the YSZ film, and their fine structure appears more bulk-like than the former spectra from the first 4 nm of the film. In order to deconvolve the different signals involved (substrate, film, interface), we have employed the multiple linear least square fit (MLLS) routine available in Digital Micrograph (see Chapter 2). First, we have extracted representative spectra from the substrate (purple curve at the bottom of Figure 8(b)) and the film (brown spectrum at the top). Then, the whole data set has been fitted to a combination of those two. The residual of the fit is plotted in the inset of Figure 8(c). If the interfacial O *K* edge spectra were a mere superposition of pure substrate-like and film contributions (e.g. due to beam broadening), the residual signal of the fit should be uniform across the whole area (mostly resulting from random noise). Quite on the contrary, we observe a significant signal in the residual around the interface area. In fact, a high contrast of white and black fringes is seen near the interface typical of statistically significant deviations (i.e., not random noise). In order to quantify this effect as a function of the distance to the interface, Figure 8(c) displays the standard deviation of the absolute value of the whole residual signal per spectrum as a function of the distance. The YSZ/YAP interface position has been highlighted with a dashed red line. It is quite obvious that there is an interfacial contribution (localized in a region within 4 nm of the interface) which cannot be fitted to a superposition of pure bulk and substrate spectra. Instead, this contribution is associated with purely interfacial features, which we discuss next.

Bulk YSZ O *K* edge spectra often show two peaks in the near edge structure, labeled p_1 and p_2 on Figure 8(b), which change relative intensities and position depending on the ZrO_2 crystal structures and the Y_2O_3

composition [18, 19]. Our data clearly show these fine structure features well within the film, in good agreement with the nominal composition of our samples. However, in the layer near the interface the p_1 and p_2 peaks get closer to each other in energy, almost merging right on the interface atomic plane (see Figure 9). These changes take place in a layer within 4 nm of the interface, which suggests the presence of changes in the coordination number or a change in the environment of the surrounding oxygen atoms. In fact, similar findings regarding the O *K* fine structure of ultrathin YSZ films have been reported by T. J. Pennycook et al. in the highly strained STO/YSZ/STO system [20]. They were ascribed to heavy disorder within the O sublattice ensuing from a high degree of epitaxial strain (around 7% in that case). In our study the degree of mismatch strain is much lower, in the 1% range. In order to analyze strain derived effects on the structure, we will analyze next the features present in atomic resolution images of the YSZ/YAP interface.

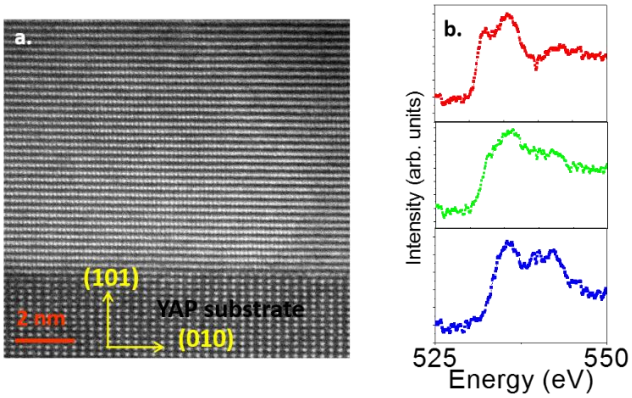

Figure 9. (a) HAADF image of a YSZ thin film. (b) O *K* edge signal of the YAP sustrates (blue), the YSZ interfacial signal (Green) and YSZ top signal (red).

Figure 9a displays a HAADF image of reference to study the strain of the sample using the "Peak Pais Analysis" (PPA) suite for Digital Micrograph (see Chapter 2). The directions (101) and (010) have been chosen as reference base vectors for our strain maps. In Figure 9b, the three main contributions to the O *K* edge that we have identified are presented. The signals correspond to the YAP substrate (blue), the YSZ interfacial signal (green) and the YSZ top signal (red).

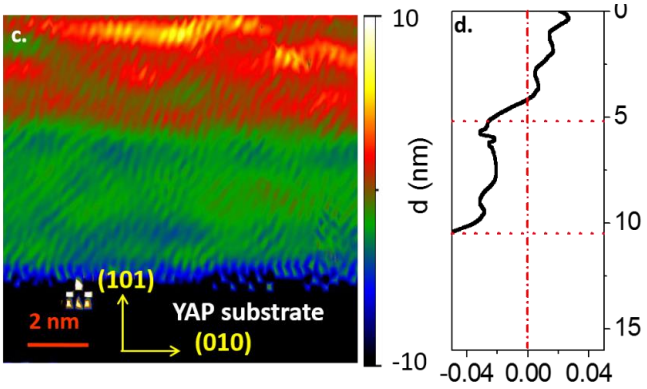

Figure 10. (a) Strain map of the thin film shown in the HAADF image in Figure 9, in the (001) direction (ε_{yy}). (b) Mean value (averaged laterally) of the map shown in (a) as a function of the distance to the interface. A region near the interface with a strain change close to 3% is seen within 4-5 nm of the interface.

The strain component map in the growth direction from the PPA strain analysis (ε_{yy}) is shown in Figure 10a. Colors from brown to white (positive values) indicate an expansion in the *c* (growth) direction respect to the reference, while colors ranging from brown to black (negative values) indicate a compression in the out-of-plane lattice parameter. The substrate area remains black, since the reference has been taken in the film. The change from green (near the interface) to red into the thin film shown in Figure 10a indicates an important relaxation in the out-of-plane lattice parameter taking place abruptly for thicknesses about 5 nm. This behavior is summarized in Figure 10b, where the laterally averaged value of the ε_{yy} parameter is plotted. Horizontal red dashed lines indicate the interface YAP/YSZ and the imaginary line where the lattice parameter changes abruptly. An expansion of 3% in the out of plane lattice parameter is observed within an averaged distance of 1.5 nm (5 atomic planes). This change is in good agreement with the results obtained from the O *K* edge analysis. It is worth noting that these structural changes are taking place in the same interfacial area where the EELS interfacial contribution is detected. The relevant changes in lattice constants observed are surely related to the O *K* ELNES variations measured here, since the EELS fine structure is strongly dependent on the nearest neighbor bonding and coordination. At this point, however, it remains unclear what the precise structural modifications are like. Comparisons to previous reports suggest a disorder in the O sublattice, which in strained YSZ results in a similar merging of the p_1 and p_2 peaks. Indeed, the perovskite and fluorite lattices exhibit a discontinuity at the interface plane that would promote such disorder. In such a case, these findings should be taken into account when pursuing future theoretical simulations of the interface O sublattice structure, and hence mobility, which would affect the interface ionic conductivity properties.

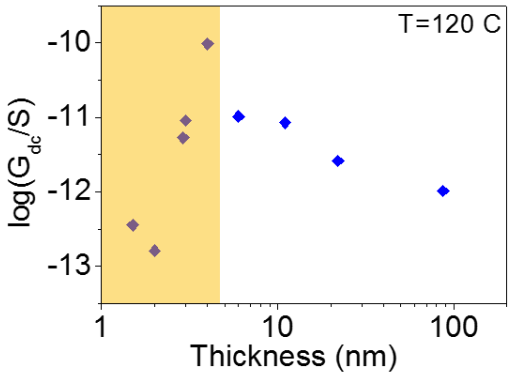

Figure 11. Conductance measured at 493 K f thin films with thickness increasing between 2 and 11 nm. The orange transparent rectangle marks the region where the anomalous out-of-plane lattice contraction is observed.

In fact, we can connect the structural features to changes in the conductivity. In Figure 11 the dc conductivity at 120ºC (traken from the Arrhenius plots of Figure) has been plotted versus the thickness of the samples. The interfacial conductance within very low thickness ranges is small but increases continuously until values of the order of 4 nm are reached (range highlighted with an orange rectangle). After this critical thickness value, reaches a saturation for larger thicknesses (>20 nm). Interestingly, this onset or critical thickness for the conductivity coincides with the values found by the STEM-EELS analyses (both strain and EELS fine structure). Hence, we can conclude that it is the first 4-5 nm of the sample that are responsible for the greatly enhanced conduction process.

4. Conclusions

In this experiment, a series of high quality YSZ(111) thin films have been grown on YAP(101) substrates by RF sputtering. The samples grow epitaxially with no signs of major defects or secondary phases. The dielectric spectroscopy measurements show that the conductance of the samples increases with the thickness, reaching a maximum value around 4 nm. Beyond this value, the conductance decreases slightly to saturate near bulk values for larger thicknesses. We find that both ionic and electronic contributions to the conductivity may exist. Transport measurements in the frequency domain performed under a N_2 atmosphere show a practical absence of blocking effects. Capacitance vs. frequency curves show two different plateaus, which suggests the presence of two types of carriers in the conduction process, both ionic and electronic. The comparison of the Arrhenius plots under different atmospheres reveals that the mobile carriers can be created or destroyed, which would also be incompatible with a purely ionic conduction mechanism. Our results indicate the electronic nature of one of the two kinds of carriers. However, the *n* or *p* type remains unclear and further experimental and theoretical work would be needed to analyze this issue. Nevertheless, in order to study the origin of these phenomena, we have studied the chemical and structural incompatibility of the system. Reciprocal space maps show that the samples accommodate epitaxial mismatch strain in a domain-like fashion, despite the dissimilar interfacial planes and the lattice mismatch. STEM-EELS experiments reveal a highly inhomogeneous strain release mechanism, through an interface-specific contribution to the O *K* edge signal clearly noticeable within the first 4-5 nm of YSZ. Some studies reported by McComb et al. [21] show similar changes in the O *K* edge by XANES and EXAFS, which they interpret in terms of changes in the coordination number of the oxygen atoms in the lattice or the Y_2O_3 concentration in ZrO_2. Other studies of the O *K* edge in YSZ explain the enhanced mobility in the STO/YSZ/STO system in terms of oxygen disorder, although these results are accompanied by a high amount of strain in the system [22]. Although the studied system presents a little amount of strain, the PPA studies presented show an abrupt change in the lattice which correlates with the continuous change of the O *K* edge signal suggesting a similar effect. We can conclude that it is the structural changes, and possibly the doping distribution, within the first 4-5 nm by the interface that are responsible for the greatly enhanced conduction process in our thin YSZ films.

5. References

[1] B. C. H. Steele and A. Heinzel, "Materials for fuel-cell technologies," *Nature* **414**, 6861, 2001.

[2] N. Sata, K. Eberman, K. Eberl, and J. Maier, "Mesoscopic fast ion conduction in nanometre-scale planar heterostructures", *Nature* **408**, 946–9, 2000.

[3] J. Maier, "Nanoionics: ion transport and electrochemical storage in confined systems" ,*Nat. Mater.* **4**, 805–815, 2005.

[4] I. Kosacki, C. M. Rouleau, P. F. Becher, J. Bentley, and D. H. Lowndes, "Nanoscale effects on the ionic conductivity in highly textured YSZ thin films", *Solid State Ionics*, 176, 1319–1326, 2005.

[5] A. Karthikeyan, C. L. Chang, and S. Ramanathan, "High temperature conductivity studies on nanoscale yttria-doped zirconia thin films and size effects" , *Appl. Phys. Lett.* **89**, 1–3, 2006.

[6] S. Azad, O. A. Marina, C. M. Wang, L. Saraf, V. Shutthanandan, D. E. McCready, A. El-Azab, J. E. Jaffe, M. H. Engelhard, C. H. F. Peden, and S. Thevuthasan, "Nanoscale effects on ion conductance of layer-by-layer structures of gadolinia-doped ceria and zirconia", *Appl. Phys. Lett.* **86**, 1–3, 2005.

[7] C. M. Wang, M. H. Engelhard, S. Azad, L. V. Saraf, D. E. McCready, V. Shutthanandan, Z. Q. Yu, S. Thevuthasan, M. Watanabe, and D. B. Williams, "Distribution of oxygen vacancies and gadolinium dopants in ZrO_2-CeO_2 multi-layer films grown on α-Al_2O_3", *Solid State Ionics* **177**,. 1299–1306, 2006.

[8] A. Peters, C. Korte, D. Hesse, N. Zakharov, and J. Janek, "Ionic conductivity and activation energy for oxygen ion transport in superlattices - The multilayer system CSZ (ZrO_2 + CaO) / Al_2O_3" *Solid State Ionics* **178**, 67–76, 2007.

[9] C. Korte, A. Peters, J. Janek, D. Hesse, and N. Zakharov, "Ionic conductivity and activation energy for oxygen ion transport in superlattices — the semicoherent multilayer system YSZ (ZrO_2 + 9.5 mol % Y_2O_3)/ Y_2O_3", *Phys. Chem. Chem. Phys.* **10**, 4623, 2008.

[10] J. Garcia-Barriocanal, a Rivera-Calzada, M. Varela, Z. Sefrioui, E. Iborra, C. Leon, S. J. Pennycook, and J. Santamaria, "Colossal ionic conductivity at interfaces of epitaxial ZrO_2:Y_2O_3/$SrTiO_3$ heterostructures", *Science* **321**, 676–80, 2008.

[11] J. Garcia-Barriocanal, A. Rivera-Calzada, M. Varela, Z. Sefrioui, M. R. Díaz-Guillén, K. J. Moreno, J. a Díaz-Guillén, E. Iborra, A. F. Fuentes, S. J. Pennycook, C. Leon, and J. Santamaria, "Tailoring disorder and dimensionality: strategies for improved solid oxide fuel cell electrolytes", *Chemphyschem*, **10**, 1003–11, 2009.

[12] M. Sillassen, P. Eklund, N. Pryds, E. Johnson, U. Helmersson, and J. Bøttiger, "Low-temperature superionic conductivity in strained yttria-stabilized zirconia," *Adv. Funct. Mater.* **20**, 2071–2076, 2010.

[13] B. Li, J. Zhang, T. Kaspar, V. Shutthanandan, R. C. Ewing, and J. Lian, "Multilayered YSZ/GZO films with greatly enhanced ionic conduction for low temperature solid oxide fuel cells", *Phys. Chem. Chem. Phys.* **15**, 1296–301, 2013.

[14] J. Hyodo, S. Ida, J. A. Kilner, and T. Ishihara, "Electronic and oxide ion conductivity in $Pr_2Ni_{0.71}Cu_{0.24}Ga_{0.05}O_4$/$Ce_{0.8}Sm_{0.2}O_2$ laminated film" *Solid State Ionics* **230**, 16–20, 2013.

[15] A. Rivera-Calzada, M. R. Diaz-Guillen, O. J. Dura, G. Sanchez-Santolino, T. J. Pennycook, R. Schmidt, F. Y. Bruno, J. Garcia-Barriocanal, Z. Sefrioui, N. M. Nemes, M. Garcia-Hernandez, M. Varela, C. Leon, S. T. Pantelides, S. J. Pennycook, and J. Santamaria, "Tailoring interface structure in highly strained YSZ/STO heterostructures", *Adv. Mater.* **23**, 5268–5274, 2011.

[16] M. Scigaj, N. Dix, M. Cabero, A. Rivera-Calzada, J. Santamaria, J. Fontcuberta, G. Herranz, and F. Sánchez, "Yttria-stabilized zirconia/$SrTiO_3$ oxide heteroepitaxial interface with symmetry discontinuity", *Appl. Phys. Lett.* **104**, 12–16, 2014.

[17] L. Vasylechko, A. Matkovskii, D. Savytskii, A. Suchocki, and F. Wallrafen, "Crystal structure of GdFeO3-type rare earth gallates and aluminates", *J. Alloys Compd.* **291**, 57–65, 1999.

[18] S. Ostanin, a J. Craven, D. W. Mccomb, D. Vlachos, a Alavi, M. W. Finnis, and a T. Paxton, "Effect of relaxation on the oxygen K-edge electron energy-loss near-edge structure in yttria-stabilized zirconia", *Phys. Rev. B.* **62**, 728–735, 2000.

[19] D. Vlachos, A. J. Craven, and D. W. McComb, "The influence of dopant concentration on the oxygen K-edge ELNES and XANES in yttria-stabilized zirconia" *J. Phys. Condens. Matter* **13**, 10799–10809, 2001.

[20] T. J. Pennycook, M. P. Oxley, J. Garcia-Barriocanal, F. Y. Bruno, C. Leon, J. Santamaria, S. T. Pantelides, M. Varela, and S. J. Pennycook, "Seeing oxygen disorder in YSZ/SrTiO 3 colossal ionic conductor heterostructures using EELS" *Eur. Phys. J. Appl. Phys.* **54**, 33507, 2011.

[21] D. McComb, "Bonding and electronic structure in zirconia pseudopolymorphs investigated by electron energy-loss spectroscopy" *Phys. Rev. B* **54**, 7094–7102, 1996.

[22] Y. Y. Zhang, R. Mishra, T. J. Pennycook, A. Y. Borisevich, S. J. Pennycook, and S. T. Pantelides, "Oxygen Disorder, a Way to Accommodate Large Epitaxial Strains in Oxides", *Adv. Mater. Interfaces* **2,** 18, 2015.

Summary

The quest for novel functionalities in strongly correlated oxide systems has often been determined by reducing dimensionality and designing nanostructured systems that exploit new physical effects. Any physical phenomena occurring within nanometric length scales are often ruled by the properties of small active regions, such as interfaces, point or extended defects, etc. In the growth process of oxide based heterostructures, the oxygen content constitutes a degree of freedom that can strongly affect the physical properties. Thus, the study of interfacial effects driven by oxygen vacancies is of great interest in order to pursue new functionalities aimed at designing future devices. Under these premises, in this thesis we have grown and characterized a number of systems comprised of complex oxide heterostructures where the O stoichiometry is tuned to produce physical behaviors not present in bulk. The local atomic structure and chemical properties of our samples have been probed with one of the most powerful techniques available currently to explore materials in real space with atomic resolution: aberration corrected scanning transmission electron microscopy (STEM) combined with electron energy-loss spectroscopy (EELS). By means of spatially resolved analyses of slight fluctuations of the local crystalline structure, composition or electronic environment imposed by the presence of O point defects defects, we have been able to explain a number of physical effects in oxide interfaces of interest in hot fields such as spintronics or energy materials, establishing the link between the atomic local structure and the macroscopic world.

Objectives and experimental results

- First, we have grown and characterized high quality ferromagnetic/insulating $La_{0.7}Sr_{0.3}MnO_3/LaCoO_3$ (LSMO/LCO) interfaces, with the general objective of fabricating novel multiferroic tunnel junctions with $LaCoO_3$ as insulating ferromagnetic barrier. For this purpose, the $La_{0.7}Sr_{0.3}CoO_3$ system with different Sr doping levels has been studied in depth in order to establish the sample quality and also obtain internal calibrations for our STEM-EELS studies (including characterization of the *3d* metal oxidation states near the interfaces). We have explored the system conductance and magnetic properties to find that tunneling magnetoresistance (TMR) values were unusually low due to changes in the magnetic anisotropy of LSMO ferromagnetic electrodes. To understand this behavior we have synthetized and analyzed LCO/LSMO (LSMO/LCO) bilayers where LSMO (LCO) is grown on top of LCO (LSMO), to find that structural distortions arising in $LaCoO_3$ buffer due to the presence of inhomogeneous densities of O vacancies layers supress of the strain-induced biaxial magnetic anisotropy of the top LSMO electrodes.

- We have also fabricated a number of asymmetric LSMO /$BaTiO_3$ /$La_{0.86}Sr_{0.14}CuO_3$ /LSMO multiferroic tunnel junctions with a main purpose: breaking the symmetry of the ferromagnetic/ ferroelectric/ ferromagnetic LSMO /$BaTiO_3$ / LSMO system by introducing an ultrathin film of an oxygen deficient $La_{0.86}Sr_{0.14}CuO_3$ cuprate between the $BaTiO_3$ barrier and the top LSMO electrode. We have found that the introduction of a high density of oxygen vacancies in the system contributes to the enhancement of the tunnel electroresistance by 10^4%. We have observed that the ferroelectric polarization state along with the location of oxygen vacancies control the size of the depletion region. We have also detected a significant electron doping at the other side of $BaTiO_3$ interface due to oxygen vacancy transfer. We observe a change

of the sign of the TMR, which we interpret that charge transfer as a spin filter effect. In summary, we show that the mechanisms of ferroelectric polarization and oxygen vacancy migration through the barrier are coupled and they should be taken into account when explaining the properties of these devices.

- Last, we turn to the study of low dimensional materials systems for energy. Electric conduction properties in ionic conductors are determined by presence of point defects, and also by lattice strains in thin films. This is especially the case in oxide films such as Y_2O_3:ZrO_2 (YSZ), where the carriers are oxygen vacancies themselves. We have grown a series of epitaxial Y_2O_3:ZrO_2(111) (8% mol) thin films on $YAlO_3$(101) substrates. Reciprocal space maps reveal that the samples present a domain matching epitaxy despite the lattice mismatch, promoting high quality growth. However, the dissimilar symmetries at the interface strongly affect the conduction properties of our YSZ films. Dielectric spectroscopy measurements have shown the presence of two kind of carriers, seemingly electronic and ionic in nature. STEM-EELS experiments reveal a highly strained interfacial layer (within the first 4-5 nm of YSZ) where an abrupt change in the lattice structure takes place, revealing an inhomogeneous strain relaxation process. Enhanced conductivity values are measured within these interfacial areas, localized within the first 4-5 nm of YSZ. Our findings suggest that interfacial effects due to new reconstructions can be responsible for the presence of two types of carriers involved in the conduction process.

Summary

Throughout this thesis, an extensive study of different oxide perovskite thin films and heterostructure devices of interest in spintronics and energy has been carried out. All the systems involved in our experiments present one or more interfaces where different oxides come face-to-face. The most usual point defect in these systems - oxygen vacancies- has been employed as a tuning parameter to promote novel behaviors. In all of these cases we have tried to make a connection between microscopic phenomena associated with O vacancies and macroscopic effects. While many questions remain unanswered, our results should be taken into account in order to harness the physical properties of future devices where O deficient complex oxides are combined.

Anex

List of publications

G. Santolino, M. Cabero, M. Varela, J.García-Barriocanal, C. León, S. J. Pennycook, J. Santamaría, "Oxygen octahedral distortions in $LaMnO_3/SrTiO_3$ Superlattices", *Microsc. Microanal.* **20**, 825-831 (2014).

M. Scigaj, N. Dix, M. Cabero, A. Rivera-Calzada, J. Santamaría, J. Fontcuberta, G. Herranz, F. Sánchez, "Yttria-stabilized zirconia/$SrTiO_3$ oxide heteroepitaxial interface with symmetry discontinuity", *Applied Phys. Lett.* **104**, 251602 (2014).

M. Rocci, J. Azpeitia, J. Trastoy, A. Pérez-Muñoz, M. Cabero, R. F. Luccas, C. Munuera, F. Monpean, M. García-Hernández, K. Bouzehouane, Z. Sefrioui, C. León, A. Rivera-Calzada, J. Villegas, J. Santamaría, "Proximity driven commensurate pining in $YBa_2Cu_3O_7$ through all-oxide magnetic nanostructures", *Nano Lett.* **15**, 7526–7531 (2015).

T.J. Pennycook, H. Yang, L. Jones, M. Cabero, A. Rivera-Calzada, C. León, M. Varela, J. Santamaría, P.D. Nellist, "3D elemental mapping with nanometer scale depth resolution via electron optical sectioning", *Ultramicroscopy* **174**, 27-34 (2017).

G. Sánchez-Santolino, J. Tornos, D. Hernández-Martín, J.I. Beltrán, C.Munuera, M. Cabero, A. Pérez-Muñoz, F. Monpean, M. García-Hernández, Z. Sefrioui, C. León, S.J. Pennycook, M.C. Muñoz, M. Varela and J. Santamaría, "Realization of a ferroelectric-domain-wall tunnel junction" (Nature Nanotechnology, accepted (2017))

A.J. Pérez-Rivero, M. Cabero, M. Varela, R. Ramírez-Jiménez, F. J. Mompean, J. Santamaría, J.L. Martínez, C. Prieto, "Thermoelectric Functionality of $Ca_3Co_4O_9$ Epitaxial Thin Films on Yttria-Stabilized Zirconia Crystalline Substrate". (*Journal of Alloys and Compounds*, submitted (2017))

M. Cabero, K. Nagy, F. Gallego, J. Tornos, D. Hernández-Martín, M. Nemes, F. Monpean, M. García-Hernández, Z- Sefrioui, T. Feher, M. Varela, C. León, J. Santamaría, "Oxygen defect controlled magnetic anisotropy at $LaCoO_3/La_{0.7}Sr_{0.3}MnO_3$ interfaces" (Under preparation for *Applied Phys.Lett.*)

M. Cabero, A. Rivera-Calzada, M. Frechero, O. J. Durá, F. Y. Bruno, M. Varela, J. Garcia-Barriocanal, C. León, J. Santamaria, "Large conductivity enhacement in unstrained YSZ epitaxial thin films" (Under preparation for *Advanced Functional Materials*)

Conference contributions

1. EELS Characterization of Interfaces Based on Ionic Conductors, M. Cabero, A. Rivera-Calzada, T.J. Pennycook, M. Varela, S.J. Pennycook, C. Leon, J. Santamaría (Poster contribution)
   Enhanced Data generated by Electrons, EDGE 2013, Saint-Maxime, France
   May 2013

2. Characterization by aberration corrected STEM-EELS of YSZ epitaxial thin films. M. Cabero, A. Rivera Calzada, T. J. Pennycook, M. Varela, S. J. Pennycook, C. León, J. Santamaría. (Poster)
   International Microscopy Conference, IMC 2014, Prague, Czech Replublic
   September 2014

3. Study of $La_{0.7}Sr_{0.3}MnO_3/BaTiO_3$ multiferroic tunnel junctions. M. Cabero, A.M. Pérez-Muñoz, D. Hernández, Z. Sefrioui, M. Varela, S.J. Pennycook, C. León, J. Santamaría. (Oral contribution)
   XXXV Bienal RSEF 2015: Strongly correlated electrons, Gijón, Spain
   July 2015

4. Study of $La_{0.7}Sr_{0.3}MnO_3/BaTiO_3$ multiferroic tunnel junctions. M. Cabero, A.M. Pérez-Muñoz, D. Hernández, Z. Sefrioui, M. Varela, S.J. Pennycook, C. León, J. Santamaría. (Poster contribution)
   International Workshop on Oxide Electronics, WOE 2015, Paris, France
   October 2015

5. Tailoring magneto-electric coupling in $La_{0.7}Sr_{0.3}MnO_3/BaTiO_3$ multiferroic tunnel junctions.
   M. Cabero, A.M. Pérez-Muñoz, D. Hernández, Z. Sefrioui, M. Varela, S.J. Pennycook, C. León, J. Santamaría. (Oral contribution)
   American Physical Society March Meeting, APS 2016, Baltimore, USA
   March 2016

6. Atomic resolution studies of $La_{0.7}Sr_{0.3}MnO_3/BaTiO_3$ multiferroic tunnel junctions.
   M. Cabero, A.M. Pérez-Muñoz, D. Hernández, Z. Sefrioui, R. Abrudan, S. Valencia, S.J. Pennycook, C. León, M. Varela, J. Santamaría (poster contribution)
   European Microscopy Conference, EMC 2016, Lyon, France
   August 2016

Short research stays

Center Oak Ridge National Laboratory, Materials Science and Technology Division
Location Oak Ridge, TN, 37830, USA
Dates: July 10th – September 12th, 2012.
November 26th – December 20th, 2012.
July 7th – August 4th, 2013.
July 8th- 28th 2014.
November 10th-26th, 2014.